

## Highlights

### **Future frame prediction in chest and liver cine MRI using the PCA respiratory motion model: comparing transformers and dynamically trained recurrent neural networks**

Michel Pohl, Mitsuru Uesaka, Hiroyuki Takahashi, Kazuyuki Demachi, Ritu Bhusal Chhatkuli

- RNNs trained online can forecast frames in chest and liver cine MRI accurately and fast.
- Online learning helps adapt to unsteady motion and reach high accuracy with few data.
- Breathing was represented mainly by the PCA motion model's first or second component.
- Data scarcity, narrow input window, and domain shift capped transformer accuracy.
- Linear filters and RNNs predicted motion well at low and high horizons, respectively.

# Future frame prediction in chest and liver cine MRI using the PCA respiratory motion model: comparing transformers and dynamically trained recurrent neural networks

Michel Pohl<sup>a,\*</sup>, Mitsuru Uesaka<sup>b</sup>, Hiroyuki Takahashi<sup>a</sup>, Kazuyuki Demachi<sup>a</sup> and Ritu Bhusal Chhatkuli<sup>c</sup>

<sup>a</sup>The University of Tokyo, 113-8654 Tokyo, Japan

<sup>b</sup>Japan Atomic Energy Commission, 100-8914 Tokyo, Japan

<sup>c</sup>National Institutes for Quantum and Radiological Science and Technology, 263-8555 Chiba, Japan

## ARTICLE INFO

### Keywords:

radiotherapy  
video prediction  
time series forecasting  
recurrent neural networks  
transformers  
online learning  
principal component analysis

## ABSTRACT

Respiratory-induced motion complicates accurate irradiation of thoraco-abdominal tumors in radiotherapy, as treatment-system latency entails target-location uncertainties. This work addresses frame forecasting in dynamic chest and liver MRI to compensate for such delays. We investigate RNNs trained with online learning algorithms, enabling adaptation to changing respiratory patterns via on-the-fly parameter updates, and transformers, increasingly common in time series forecasting for their ability to capture long-term dependencies.

Experiments were conducted using twelve sagittal thoracic and upper-abdominal cine-MRI sequences from ETH Zürich and Otto-von-Guericke University Magdeburg (OvGU). PCA decomposes the Lucas–Kanade optical-flow field into static deformations and low-dimensional time-dependent weights. We compare various methods forecasting the latter: linear filters, population and sequence-specific encoder-only transformers, and RNNs trained with real-time recurrent learning (RTRL), unbiased online recurrent optimization, decoupled neural interfaces, and sparse one-step approximation (SnAp-1). Predicted displacements were used to warp the reference frame and generate future images.

Prediction accuracy decreased with the horizon  $h$ . Linear regression performed best at short horizons (1.3mm geometrical error at  $h = 0.32s$ , ETH Zürich dataset), while RTRL and SnAp-1 outperformed the other algorithms at medium-to-long horizons, with geometrical errors below 1.4mm and 2.8mm on the sequences from ETH Zürich and OvGU (the latter featuring higher motion variability, noise, and lower contrast), respectively. The sequence-specific transformer was competitive for low-to-medium horizons, but transformers remained overall limited by data scarcity and domain shift between datasets. Predicted frames visually resembled the ground truth, with notable errors occurring near the diaphragm at end-inspiration and regions affected by out-of-plane motion.

## 1. Introduction

### 1.1. Respiratory motion management in MR-guided radiotherapy

Machine learning can benefit external beam radiotherapy at various steps within the clinical workflow, ranging from supporting the optimal treatment plan selection, improving dose planning and radiation delivery, to helping assess patient response to the therapy session [1]. Among those steps, respiratory motion forecasting during treatment is a critical application that can enhance therapeutic irradiation precision and patient outcome. Indeed, the beam may partially miss the moving target (e.g., the lung or pancreas tumor) and negatively affect surrounding healthy tissue instead, due to intrinsic treatment-system latency. Specifically, rotations, deformations, and translations of the tumor and surrounding organs at risk (OAR) induced by breathing can cause geometric and dosimetric errors. Thoracic and upper-abdominal tumor motion is primarily periodic, with a range in the cranio-caudal direction sometimes exceeding 5cm [2]. Nonetheless, it is influenced by phase shifts and local variations in frequency and amplitude. Amplitude shifts refer to

sudden and occasional variations in the average position of the organs, while the term "drift" describes more gradual changes occurring during a single treatment session. For example, baseline intrafractional drifts of  $1.65 \pm 5.95$  mm,  $1.50 \pm 2.54$  mm, and  $0.45 \pm 2.23$  mm (mean  $\pm$  standard deviation) have been observed in the superior-inferior (SI), anterior-posterior, and left-right directions, respectively [3]. Moreover, general posture changes due to patient relaxation as time elapses or minor positional adjustments on the treatment bed also add to the variability in motion records. Each radiotherapy treatment system has a specific characteristic time delay, but "for most radiation treatments, the latency will be more than 100ms, and can be up to two seconds" [4].

During external beam radiotherapy treatment of thoracic and abdominal tumors, the three-dimensional (3D) target cannot be imaged fully in real time. Conventional methods rely on tracking fiducial markers implanted near the target using kilovoltage (kV) fluoroscopic imaging (e.g., the CyberKnife Synchrony [CKS] system), which requires an invasive surgical procedure, or on recording the positions of external markers on the chest and abdomen (e.g., the Varian Real-Time Position Management [RPM] system), whose trajectories may correlate only weakly with tumor motion, partly due to phase shifts. Recent advancements in

\*Corresponding author

 michel.pohl@centrale-marseille.fr (M. Pohl)

magnetic resonance imaging (MRI) have enabled real-time observation of soft tissue and organs with high contrast in a fixed imaging plane. Moreover, magnetic resonance-guided (MR-guided) radiotherapy systems (e.g., MRIdian) do not involve additional imaging dose, unlike systems relying on kV fluoroscopy or four-dimensional cone beam computed tomography (4D-CBCT). Consequently, they can image free-breathing in the slice of interest over relatively long periods, enabling the observation of inter-cycle variations. By contrast, 4D-CBCT can only capture an average breathing cycle, due to dose and hardware constraints. This improved visualization, combined with online adaptive planning capabilities (i.e., on-table plan re-optimization based on real-time imaging) specific to MR-guided radiotherapy, can widen eligibility for high-dose focal liver irradiation and support improved local control in cases where motion and OAR dose constraints would otherwise limit treatment due to toxicity [5]. Fast four-dimensional (4D) MRI is an active area of research, motivated by the relatively low spatial resolution and image quality of current 4D acquisition techniques. In that context, artificial intelligence (AI) research for MR-guided radiotherapy has focused on 3D motion estimation from the observed two-dimensional (2D) slices and irradiation delay mitigation—our work addresses the latter challenge.

Previous works have explored mathematical correspondence models that derive 3D internal motion, which is not observable in real time, from surrogate signals (also referred to as partial observations). Fitting such models requires prior, simultaneous acquisition of image and surrogate signal data. Correspondence and forecasting models may be subject-specific, when fitted to data from a single patient, or population-based, also termed cross-subject, when trained on data from multiple individuals. Wang et al. inferred liver motion from ultrasound images using the positions of light-emitting diodes (LED) placed on the chest as surrogate signals (AccuTrack 250 system), and further forecast these positions to achieve spatio-temporal prediction [6]. They reported that long short-term memory (LSTM) networks outperformed support vector regression (SVR) on both tasks, and that continuously updating the correlation model improved accuracy.

Principal component analysis (PCA), an unsupervised dimensionality-reduction algorithm that can be interpreted as fitting an ellipsoid to the data, has been widely used in correspondence models. In radiotherapy, the key step in PCA—eigendecomposition of the data matrix—is commonly applied to motion information obtained via deformable image registration (DIR) between a reference phase and other phases in a four-dimensional dataset (Appendix C). That approach implicitly assumes that linear combinations of the leading eigenvectors can approximate relevant organ motion states. Two broad strategies utilizing PCA in correspondence modeling are highlighted in [7]: direct and indirect modeling. In direct models, PCA is applied to internal or surrogate data and a regression method is fitted using the PCA weights, or PCA itself is used to fit the correspondence model. The firstly introduced PCA respiratory motion

model belongs to the latter subcategory [8]. In that work, Zhang et al. inferred the displacement vector field (DVF) within the whole chest from the diaphragm position in four-dimensional computed tomography (4DCT) and argued that two principal components were sufficient to describe breathing motion accurately. Likewise, Chen et al. applied PCA to fit a correspondence model relating tumor and lung motion to that of the external chest surface in 4DCT, using particle-based surface meshing and topology-preserving non-rigid point matching registration [9]. Conversely, Li et al. performed regression-based direct modeling using PCA fitted with internal data, as they inferred the entire chest motion from a single artificial marker using Bayesian maximum-a-posteriori estimation [10]. They recommended to select the number of components on a per-patient basis and experimentally also found that two components were generally sufficient. This finding was supported by the fact that two eigenvectors can exactly represent a cosine breathing model.

By contrast, in indirect models, the weights associated with principal components derived from internal motion are estimated by maximizing the similarity between partial 2D observations and the corresponding cross-sections from inferred 3D data (the warped reference volume). Subject-specific indirect models were used to synthesize volumetric magnetic resonance (MR) images from 2D cine MRI in [11, 12]. The Bayesian information criterion was applied to select the PCA subspace dimension in [11]; one component was favored as the best bias–variance trade-off, but a second component was retained in practice to model respiratory motion hysteresis. Romaguera et al. mentioned that "results reported for these patient-specific models are often more accurate than for population-based methods. In a clinical scenario, their reliability depends, however, on the degree of patient-specific inter-fraction motion variations" [13].

## 1.2. Breathing motion prediction with recurrent and attention-based neural networks

Recurrent connections are widespread in recent artificial neural network architectures proposed for respiratory motion forecasting in radiotherapy [14, 15, 16, 17, 18]. At the core of all recurrent neural network (RNN) variants, these feedback loops act as a form of memory by enabling the storage and retrieval of information over time. This distinctive feature allows them to effectively learn patterns and relationships within sequential data and often surpass conventional multilayer perceptrons (MLP) and linear models in time-series or natural language processing (NLP). Studies have shown that recurrent models such as deep bi-directional gated recurrent units (bi-GRU) or LSTMs can outperform simpler algorithms, for instance, adaptive-boosted MLPs [14] and linear filters [17], in breathing motion prediction.

Respiratory motion forecasting has also been influenced by research on attention-based algorithms, most notably transformers. Originally introduced by Bahdanau to improve neural machine translation, attention mechanisms allow models to dynamically focus on relevant parts of an

input sequence [19]. This helps reduce the information bottleneck of encoding long history into a single recurrent state and mitigate long-range dependency issues often associated with vanishing gradients during RNN training. While early forms of attention operated sequentially alongside RNNs, transformer self-attention helps avoid the strictly sequential update of recurrent models by enabling parallel computation over sequence positions [20]. This can accelerate training, while allowing each token to attend to all others simultaneously.

Recent research on general time series forecasting with transformers has explored improvements regarding complexity and sequential data modeling. For instance, Li et al. proposed the LogSparse transformer, making each cell attend to previous ones following exponentially increasing intervals, and using causal convolutions in self-attention to better capture local context [21]. Also leveraging sparsity to reduce complexity, Zhou et al. focused on long sequence forecasting and introduced the Informer [22]. The latter relies on the ProbSparse self-attention, which operates using only a selected subset of dominant queries based on a sparsity measurement derived from the Kullback-Leibler divergence. This architecture is characterized by shrinking encoder representations at each layer via max-pooling and a generative-style decoder that can perform prediction in one forward operation. In the Autoformer model, proposed for long-term forecasting, self-attention is replaced with auto-correlation, helping discover similarities based on periodicity, and the input is decomposed into seasonality and trend, whose representations are progressively refined [23].

Regarding respiratory motion forecasting, Jeong et al. compared a full encoder–decoder transformer with an LSTM and a bi-directional long short-term memory (bi-LSTM) network to predict the distance from a laser source to the chest surface of cancer patients (Anzai respiration-gating system). The transformer outperformed the other two models at horizons  $h \geq 0.50s$  (the time interval in the future for which the prediction is made, also called response time or look-ahead time). Moreover, Shi et al. predicted respiratory signals using an architecture combining squeeze-and-excitation attention with a temporal convolutional network (TCN) component [25]. It consistently yielded lower mean average error and root-mean-square error (RMSE) than the bi-LSTM model examined in [14] and CNN–TCN and CNN–bi-LSTM baselines, for  $h \geq 0.30s$ .

Despite recent progress enabled by transformers in time series processing, models in that family remain constrained by computational and memory bottlenecks. In particular, the complexity of the canonical transformer architecture grows quadratically with the input length. Notably, Romaguera et al. reported that their transformer-based approach for predicting future volumes from 2D dynamic liver MRI was approximately three times slower than baselines relying on a convolutional long short-term memory (ConvLSTM) or convolutional gated recurrent unit (ConvGRU) module [26]. These costs practically limit usable context length, which in turn can hinder long-range dependency modeling. In

addition, standard transformers lack built-in notions of order or locality, in opposition to RNNs. The latter have stronger inductive biases, as their core definition, involving a hidden state evolving over time, implies assumptions regarding continuity and causality. Accordingly, recent evidence suggests that although transformers trained on large datasets tend to perform well, RNNs can be more sample-efficient and generalize better in low-data regimes, sometimes with equivalent parameter counts. Haller et al. provided such comparative analysis in the context of low-resource language modeling, using datasets of 10M–100M words, and showed that recurrent architectures, including hierarchically gated linear RNNs (HGRN), can surpass decoder-only transformers on multiple benchmarks with controlled parameter budget (approximately 300M–360M weights) [27]. In biomedical imaging and signal processing, datasets are often relatively small, partly due to privacy and data-governance constraints, and it has been stated that "this poses challenges for training and validating transformer models effectively" [28]. Importantly, there is an ongoing discussion regarding the practical applicability of transformers in radiotherapy. For example, Wimmert et al. reported that an LSTM outperformed a limited-history transformer for predicting Varian RPM signals despite a large cohort (2,502 traces, 416 patients, mean duration of 130s) [29]. However, their full-history encoder-only transformer (without window limitation) surpassed the LSTM in accuracy. Attention maps revealed that its third and fourth layers attended to similar patterns relatively far (up to approximately 80s) in the past. Nonetheless, its inference time was roughly 100 times higher than that of the LSTM, potentially constraining clinical feasibility.

In this context, research on RNNs has evolved alongside that on transformers, with recent works proposing hybrid models that integrate elements of both architectural families. For instance, Tan et al. proposed the LSTformer, which combines transformer-encoder and LSTM-based layers, to predict CyberKnife respiratory motion traces, using a dataset of 304 records (26Hz sampling, 71min average duration) [30]. This model consistently outperformed LSTM, bi-LSTM, and bi-GRU baselines [15, 14, 16] for various metrics over horizons between 0.20s and 0.60s, although inference time was nearly 1.5 times higher than for the LSTM. Moreover, Zhang et al. introduced LGEANet, a network designed for multivariate time series forecasting, combining LSTM layers, temporal convolutional and linear autoregressive (AR) modules, and external attention (small, trainable, and shared memory units accounting for relationships between all samples) [31]. When trained and evaluated on the same CyberKnife dataset, LGEANet consistently surpassed several attention-based and recurrent baselines over the four test sequences and horizons between 0.07s and 0.92s. These observations underscore the continued relevance of approaches involving recurrent architectures in breathing motion prediction.

### 1.3. Online learning algorithms for RNNs applied to respiratory motion forecasting in radiotherapy

A common strategy in sequence processing is to adjust model parameters as new samples arrive, improving robustness to patterns unseen during training. To achieve that, one can simply fine-tune the model using the information contained within a sliding time window, beyond which past data is discarded. For instance, such an approach was used to personalize and update over time a cross-subject MLP predicting lung-tumor SI positions recorded by the CKS system [32]. Similarly, Lombardo et al. adapted a population LSTM forecasting SI tumor motion in 2D cine MRI (acquired on MRIdian) to a specific patient via sliding-window updates [17]. They reported RMSE decreases from 2.02mm to 1.77mm and from 1.59mm to 1.34mm on both test sets at  $h = 0.75$ s compared to offline learning (the training procedure without continuous adaptation). This strategy can improve performance but induces forgetting, as earlier examples outside the current window no longer contribute to parameter updates. A related and widely used approach for dynamic training of RNNs is truncated backpropagation through time (TBPTT), which limits gradient propagation to a fixed history length [33]. In TBPTT, past data influence persists implicitly via forward recursion using non-detached states. By contrast, sliding-window retraining with backpropagation through time (BPTT), the standard offline training procedure for RNNs, is prone to representation drift due to repeated reinitialization. While TBPTT remains relatively resource-efficient, with a time complexity of  $\mathcal{O}(Td^2)$ , where  $d$  and  $T$  denote the number of hidden units and truncation length, respectively, it still biases learning towards more recent dependencies.

Unlike sliding-window retraining or TBPTT, truly online training methods retain knowledge over a longer effective time span. Indeed, parameter update equations do not directly reference a past time point beyond which information is lost. Real-time recurrent learning (RTRL), a fundamental online learning algorithm for RNNs, operates by recursively updating the sensitivity matrix (the derivative of the hidden state with respect to the parameters), also referred to as the influence matrix, at each time step [34]. This algorithm has been used to forecast the locations of fiducial markers implanted in the lungs (SyncTraX system) [35], abdominal and thoracic cancer lesions recorded by the CKS system [36], chest internal points tracked with DIR in 4D cone beam computed tomography (CBCT) images [37], and external markers on the chest and abdomen of volunteers (NDI Polaris system) [38, 39]. Nonetheless, RTRL is limited by its high computational complexity, which scales as  $\mathcal{O}(d^4)$ , rendering inference impractical even for moderately sized networks.

Several online-training algorithms for RNNs have been proposed to lower computational requirements compared to RTRL, while avoiding the truncation bias incurred by

Algorithm	Complexity	
	Memory	Time
Real-time recurrent learning [34]	$\mathcal{O}(d^3)$	$\mathcal{O}(d^4)$
Truncated BPTT [40]	$\mathcal{O}(Td)$	$\mathcal{O}(Td^2)$
Unbiased online recurrent optimization [41]	$\mathcal{O}(d^2)$	$\mathcal{O}(d^2)$
Kronecker-factored RTRL [42]	$\mathcal{O}(d^2)$	$\mathcal{O}(d^3)$
Kernel RNN learning [43]	$\mathcal{O}(d^2)$	$\mathcal{O}(d^2)$
r-optimal Kronecker-sum approximation [44]	$\mathcal{O}(rd^2)$	$\mathcal{O}(rd^3)$
Random-feedback online learning [45]	$\mathcal{O}(d^2)$	$\mathcal{O}(d^2)$
Sparse one-step approximation [46]	$\mathcal{O}(d^2)$	$\mathcal{O}(d^2)$
Reverse Kronecker-factored RTRL [47]	$\mathcal{O}(d^2)$	$\mathcal{O}(d^3)$
Efficient BPTT [47]	$\mathcal{O}(Td)$	$\mathcal{O}(d^2)$
Future-facing BPTT [47]	$\mathcal{O}(Td)$	$\mathcal{O}(Td^2)$
Decoupled neural interfaces [48]	$\mathcal{O}(d^2)$	$\mathcal{O}(d^2)$

**Table 1**

Memory and time complexity of several online learning algorithms for RNNs. In the last two columns,  $d$  and  $T$  designate the number of hidden units and the truncation length, respectively<sup>1</sup>.

TBPTT to better preserve learning signals from distant past time steps (Table 1) [47]. In unbiased online recurrent optimization (UORO), the sensitivity matrix is approximated by an unbiased, random rank-one estimator updated recursively [41]. This, in turn, produces unbiased loss gradient estimates, but introduces additional stochasticity. Other approaches leverage sparsity to reduce time complexity; for instance, sparse  $n$ -step approximation (SnAp- $n$ ) tracks only parameter-to-state dependencies that affect hidden units within  $n$  recurrent steps [46]. SnAp- $n$  introduces bias during loss gradient estimation but yields deterministic closed-form updates. The specific case  $n = 1$  (SnAp-1) corresponds to a diagonal-like approximation of the sensitivity matrix, similar in spirit to early forward-mode training formulations for LSTMs [49]. Unlike UORO and SnAp-1, which compress past information encoded in the sensitivity matrix, decoupled neural interfaces (DNI) is future-facing, as it seeks to predict the error signal, i.e., the derivative of the future accumulated loss with respect to the hidden states [47, 48]. Originally introduced as a framework relevant to both recurrent and non-recurrent networks, DNI aims to eliminate the dependency of modules on the completion of backward or forward computations by other modules before updating their own weights. This is achieved by learning a "synthetic gradient," an independent prediction of the error signal, at each layer. The updates in DNI are biased, deterministic, and numerical, as the synthetic gradient is obtained via auxiliary optimization rather than closed-form recursion. Notably, UORO, SnAp-1, and DNI benefit from a relatively low computational complexity of  $\mathcal{O}(d^2)$ ; efficient implementations for vanilla RNNs were presented in [38, 39]. Specifically, closed-form simplifications for quantities involved in the loss gradient calculation in UORO were derived in [38]. Regarding SnAp-1, compression of sparse matrices (including the influence matrix) into a compact, dense form was introduced to reduce practical memory and

<sup>1</sup>Adapted from [47] (open-access article), first published in modified form in [39], Copyright JMLR 2020.

computational requirements in [39]. The same work also improved the linear-operator update used to fit the synthetic gradient, compared with the standard RNN formulation in [47], yielding higher empirical accuracy. These three algorithms were first applied to radiotherapy (in external marker position forecasting) in [38, 39] and generally outperformed RTRL under roughly comparable computational budgets (e.g., smaller value of  $d$  for RTRL).

## 1.4. Future frame prediction in natural videos and medical imaging

### 1.4.1. Video prediction in general computer vision

Closely related to time series forecasting, video prediction, the self-supervised task of estimating future frames given a sequence of past successive frames, has seen much interest in the computer vision community, with some applications in robotic control [50, 51], autonomous driving [52, 53, 54], or precipitation nowcasting [55]. Natural videos exhibit complex dynamics across scales and may involve occlusions, camera motion, and illumination changes, which makes forecasting challenging. Furthermore, the future is multimodal, as multiple outcomes may be consistent with the past frames, which can produce blurred predictions, especially at long horizons  $h$ . Overall, prediction accuracy typically degrades as  $h$  increases. Recurrent models have long been a common backbone for temporal modeling in video prediction. Early RNN-based video predictors include ConvLSTM, which replaces fully connected transitions with convolutions to better capture spatial structure [55], and extensions of the LSTM encoder–decoder model originally developed for machine translation [56, 57]. Notably, Jin et al. reported that sliding-window fine-tuning at test time with BPTT improved multi-step predictions relative to purely autoregressive rollouts [52]. More recently, transformer-based approaches have been proposed for video prediction, framing it as generation of a fixed block of future frames conditioned on a short context. For example, MaskViT uses a masked visual modeling objective (it masks a subset of tokens and predicts the remaining ones) together with iterative decoding that progressively fills in masked tokens from the most confident predictions [51].

Oprea et al. comprehensively surveyed deep learning methods for video prediction and proposed a taxonomy of approaches [58]. Early works attempted to forecast raw pixel values directly by implicitly capturing fine details and scene dynamics [55, 57, 53]. Nevertheless, learning a stable and meaningful representation from raw frames proved difficult due to the high dimensionality and variability of the pixel space, motivating developments aimed at structuring and simplifying internal representations. One line of work has focused on separating variability elements from the visual content, which Oprea et al. refer to as "factorizing the prediction space." One such strategy consists of disentangling motion and appearance using a two-stream processing approach [59]. Another subcategory of methods represent change as explicit transformations between subsequent frames to

leverage the latter's high level of similarity, using kernel-based or vector-based resampling [60, 61]. Architectures relying on vector-based resampling predict a dense motion field between an observed frame and a future frame, then warp the former to synthesize the latter. This resampling approach often relies on a spatial transformer-style differentiable warping module [62]. The original spatial transformer network comprises a localization network that predicts the parameters of geometrical transformations and a sampling layer that applies them to the input image or feature map. It has been argued that such approaches "can avoid [the] blurring problem by copying coherent regions of pixels from existing frames" and "lead to more realistic and sharper results than techniques that hallucinate pixels from scratch" [61]. By contrast, Oprea et al. group methods that "narrow the prediction space" either by "conditioning the predictions on extra variables" (e.g., the state or actions of a robot [60, 63, 51]) or by reframing the forecasting task in a higher-level space (e.g., segmentation maps [52, 54] or keypoint coordinates [50]). In parallel, the challenge of future multimodality has spurred probabilistic approaches based on latent-variable models, including variational auto-encoders (VAE) and variational recurrent neural networks (VRNN) [63, 64, 50]. A VAE learns a distribution over a low-dimensional representation  $z$  from which inputs can be reconstructed; VRNNs extend this framework to recurrent architectures. In computer vision, such models can generate images by sampling from a prior over the encoding  $z$ , thus introducing a probabilistic element to the otherwise deterministic latent space of traditional auto-encoders (AE).

### 1.4.2. Future frame estimation in thoraco-abdominal and cardiac image sequences

Video prediction in dynamic chest and liver imaging is valuable for radiotherapy, as it helps characterize the future motion of anatomical structures of interest. By contrast, many works on tumor position estimation have attempted to predict only its centroid trajectory, which does not capture spatially varying deformations. Several studies on motion compensation in radiotherapy have also addressed organ and tumor contour estimation or interpolation between subsequent frames in 4DCT imaging to better estimate target volume during treatment planning. For instance, dynamic mode decomposition—an eigenvalue decomposition method that identifies a linear evolution operator capturing temporal dynamics—was applied to tumor contour samples for motion modeling, in [65]. However, our contribution focuses on video forecasting in cine MRI from past frames alone, without requiring or inferring contours. This task is particularly challenging due to the limited temporal resolution, potentially low contrast and signal-to-noise ratio (SNR), and specific degradations (e.g., susceptibility, flow, chemical shift, or magnetic field inhomogeneity artifacts) associated with that imaging modality. Future multimodality, arising from respiratory irregularities, cardiac beating, or out-of-plane motion (Section 1.1), and limited cohort sizes and sequence lengths can add to the difficulty. Nonetheless,

cine MRI forecasting is one critical step towards enabling real-time motion tracking in MR-guided radiotherapy and connects to broader video prediction research.

Chhatkuli et al. applied PCA to raw pixel intensities and predicted the associated time-dependent weights with multi-channel singular spectral analysis (MSSA) to forecast chest image sequences [66]. They evaluated this method using kV fluoroscopic phantom images and coronal 4DCT cross-sections. Likewise, Pham et al. employed PCA to model the DVF between the reference and incoming frames and forecast the corresponding coefficients using adaptive-boosted MLPs to predict 3D chest cine-MRI sequences from extended cardiac-torso phantom (XCAT) data and a liver cancer patient [67]. A similar approach was used in [68] to predict chest surfaces reconstructed from point clouds captured by a 3D photogrammetry system. In that work, kernel principal component analysis (kPCA) was applied to the time-varying surface height map, and a linear AR model was used to forecast the low-dimensional motion representation in the kernel feature space. The PCA models in [66, 67, 68] were subject-specific; it was observed that an oscillatory pattern following the breathing motion characterized the first-order weights.

Regarding video prediction with deep learning, Nabavi et al. applied the predictive coding network (PredNet)—a direct-pixel-synthesis ConvLSTM-based architecture inspired by the neuroscience concept of predictive coding—to forecast chest 4DCT cross-sections [69, 53]. By contrast, Romaguera et al. adopted a warping (vector-based resampling) strategy and designed a neural network inspired from VoxelMorph, an encoder–decoder model for self-supervised DIR, to forecast 2D liver images from multiple modalities (MRI, computed tomography [CT], and ultrasound) [70, 71]. Their architecture included multi-scale residual blocks and a ConvLSTM module to model temporal dynamics. More recent works have focused on future volumetric MR image generation from 2D cine MRI to simultaneously address the intrinsic delays and real-time 3D imaging limitations of MR-guided linear accelerator (MR-LINAC) systems (Section 1.1). Notably, Romaguera et al. proposed an encoder–decoder network (similar to that in [70]) that estimates the latent encodings of future 3D deformations from the incoming 2D frames [13]. They later reformulated that architecture using a conditional VAE backbone and achieved a lower vessel tracking error (TE) [72]. Further accuracy improvements were reported after replacing the ConvLSTM component in the latter work with a transformer using prior-based conditioning and learnable queries for temporal prediction [26]. In these studies, predictions were generally less accurate near end-inspiration (EI), especially around the diaphragm edge, as that phase exhibits high inter-cycle variability. It has also been reported that blood vessels entering or leaving the imaged slice due to out-of-plane motion were challenging to predict. Also using a latent-variable probabilistic AE to learn low-dimensional motion representations of intra-interventional image sequences, Gunnarsson et al. modeled temporal dynamics in cardiac imaging with

a linear Gaussian state-space model (LG-SSM) [73]. They introduced patient-specific online adaptation of the LG-SSM by maximizing, via Kalman filtering, the marginal log-likelihood of recently inferred latent states, which improved ultrasound forecasting performance compared with a fixed pretrained model. They also reported competitive offline cine-MRI interpolation results relative to conventional registration baselines.

## 1.5. Contributions and scope of this study

Most works addressing breathing motion forecasting for radiotherapy have focused on low-dimensional respiratory surrogate signals, such as external motion traces acquired by optical tracking systems [15, 17, 39], while studies on future frame prediction in thoraco-abdominal imaging have been scarce [70]. In this study, we apply for the first time online learning algorithms for RNNs to chest and liver cine-MR image prediction, to our knowledge, and compare them with transformers, the backbone of many developments in time series forecasting. Regarding RNN algorithms, RTRL and more efficient, recent approaches (UORO, SnAp-1, and DNI) were selected as a standard, computationally exact baseline and due to their more favorable time and memory complexity (Table 1), respectively. We first chose a simple, standard RNN structure given the small size of our datasets and the scope of this study—a proof of concept focused on comparing broad architectural and training paradigms. Such vanilla RNNs can suffice in low data regimes, whereas architectures based on LSTM or gated recurrent unit (GRU) cells, whose greater gating capacity can help better capture longer-range dependencies, might benefit from more training data. Although transformers typically require large amounts of data, we selected a lightweight encoder-only model, as a modern, representative attention-based forecasting method. In particular, Romaguera et al. proposed an end-to-end transformer-based algorithm to forecast frames in respiratory cine-MRI [26]; we explore transformers with a different experimental angle. Indeed, our modular approach can work with smaller datasets and we discuss paradigms such as population-based versus subject-specific training and online versus offline learning, and highlight domain adaptation challenges when scanning protocol and image characteristics differ, assessing robustness to varying levels of noise and contrast. Such insights are particularly needed as "the application of attention mechanisms for deformation prediction is still underexplored in the literature" [26].

Prior PCA-based approaches to respiratory motion prediction relied on simple surrogates, forecasting algorithms, or pixel-space representations. For instance, the baseline forecasting pipeline in Romaguera et al. combined a PCA motion model driven by a one-dimensional surrogate signal with temporal prediction using an adaptive linear filter. By contrast, we derive a sequence-specific internal motion model by applying PCA to dense deformation fields and predict temporal dynamics with modern algorithms. Specifically, we use the Lucas–Kanade optical-flow algorithm to estimate deformations between the incoming and reference

frames; this DIR technique has been commonly used in chest imaging [74, 75, 76], and here we analyze the optimization of its parameters in chest cine MRI. Li et al. selected the PCA subspace dimension by minimizing the validation error between the ground-truth and reference DVFs in 4DCT imaging [10]; we extend this general validation-based model selection approach to cine MRI forecasting. We forecast the time-dependent PCA weights to obtain the future DVFs, which are then used to warp the reference frame and estimate the next frames. As such, our approach belongs to the vector-based resampling category in the classification of video forecasting models of Oprea et al. [58]. We comprehensively evaluate performance across multiple accuracy metrics and a wide range of horizons (up to 2.2s). Finally, we highlight the interpretability of our approach by analyzing deformation modes and linking PCA-weight prediction errors to mismatches between the predicted and ground-truth frames.

## 2. Materials and methods

### 2.1. Chest and liver cine-MRI data

This study uses two publicly available datasets; the first one comprises two volumetric chest MR image sequences; we refer to it as the ETH Zürich dataset [77]. The original 4D-MRI data was acquired using a technique based on “stacking of dynamic 2D images using internal image-based sorting” [78, 79]. Using bicubic spline interpolation, we resampled the original volumes to a  $1\text{mm}^3$  isotropic resolution. We then selected two sagittal planes for each subject, totaling four sequences of 2D images. The latter thus have an isotropic in-plane resolution of  $1\text{mm}^2$  per pixel; they are encoded in 8 bits. Lastly, we shifted the frames in each sequence so that the first one corresponds to the middle phase within the expiration; the resulting sagittal MRI sequences each comprise 200 frames, as the initial 4D data. Sequences 1 and 4 comprise cross-sections from the left part of the chest and include cardiac motion, whereas sequences 2 and 3 correspond to the right hemithorax.

In this study, we also used eight 2D sagittal cine-MRI sequences, each from one individual, covering mainly the liver and surrounding organs such as the kidneys, from another dataset publicly available online [80, 81]. The latter is referred to as the Otto-von-Guericke University Magdeburg (OvGU) dataset throughout this paper. Those images were acquired on a MAGNETOM Skyra MRI scanner (Siemens Medical Solutions, Erlangen, Germany) using a TRUFI sequence and just enough contrast to detect respiratory motion. No body array coil was utilized; acquisition used the fixed receiver coil of the bore. Two reference 2D MRI sequences were available for each subject in that dataset. They are also referred to as “navigator” sequences in the context of 4D-MR reconstruction, as they cover a static plane representative of breathing motion. We arbitrarily selected one per patient based on visual assessment of image quality and characteristics. Specifically, we chose the acquisition whose frames had lower levels of noise and vessel flickering due to blood circulation, as that could render prediction harder. Those

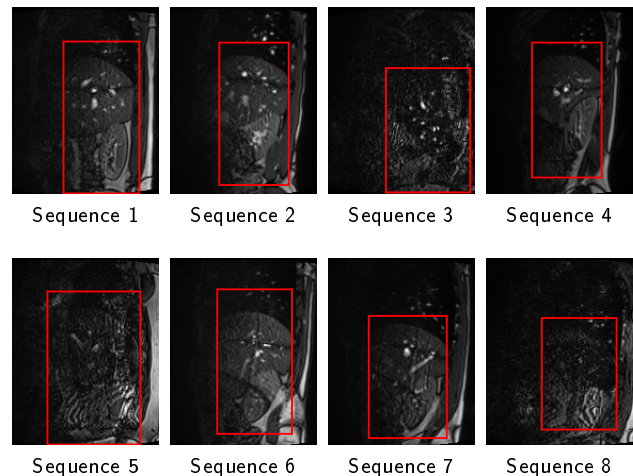


**Figure 1:** MR images from the Magdeburg dataset at the initial time step  $t = t_1$ , with the high-contrast ROI selected for algorithm evaluation displayed as a red rectangle.

navigator slices are characterized by lower contrast, higher noise, and more respiratory motion variability than the frames in the ETH Zürich dataset. In particular, sequences 3, 5, and 8 featured high noise, contrast variations with time were more pronounced in sequence 6, and sequence 4 exhibited particularly irregular breathing combining deep and shallow inspirations. The pixel resolution in the eight image sequences was  $1.818 \times 1.818$  (the through-plane resolution was  $4\text{mm}^3$ ); we did not perform resampling and kept that original pixel resolution in our study. However, we discarded the first 15 images of each original acquisition, as those were subject to higher contrast variability overall; the resulting sequences comprised 498 frames. Finally, for each subject, we selected a region of interest (ROI) where contrast was higher, for algorithm evaluation (Fig. 1). We intentionally avoided including the spine in the ROIs, as it is largely immobile during respiration and may introduce spurious errors in DIR due to out-of-plane motion or imaging artifacts.

Table 8 in Appendix A summarizes the characteristics of both datasets. One notable difference between them is their sampling frequency, as the ETH Zürich MRI sequences have a lower rate (approximately 3.18Hz) than those in the OvGU dataset (6.0Hz). Sequences in the former dataset also have a shorter duration (63s) than those in the latter (83s).

### 2.2. Breathing motion modeling with PCA

For each MR image sequence, DIR between the initial 2D frame (at time  $t_1$ ) and that at time  $t$  is performed using the pyramidal iterative Lucas–Kanade optical-flow algorithm [82, 83, 84], following the implementation in [38] (with a straightforward adaptation from 3D to 2D). In the following, we denote by  $\vec{u}(\vec{x}, t)$  the push-forward 2D local deformation vector at pixel  $\vec{x}$  and time  $t$ , which satisfies the local brightness constancy assumption, by definition:

$$I(\vec{x}, t_1) \approx I(\vec{x} + \vec{u}(\vec{x}, t_k), t_k) \quad (1)$$

We optimize optical-flow parameters for each sequence with grid search, minimizing the registration error averaged over the first 28.3s of each acquisition (Appendix B).

The vector resulting from concatenating and centering the deformations  $\vec{u}(\vec{x}, t)$  at time  $t$ ,  $X_c(t)$ , lies in a high-dimensional space of dimension  $2|I|$ , where  $|I|$  designates the number of pixels (Eq. 27 in Appendix C). Yet, the complex overall spatiotemporal variations are driven by relatively simple phenomena that can be described with few degrees of freedom. We use PCA to project the centered motion vector  $X_c(t)$  onto a linear subspace of dimension  $n_{cp}$ , with  $n_{cp} \ll 2|I|$ . Mathematically, for a sequence of  $M_{\max}$  frames, we compute, for each  $j \in \{1, \dots, n_{cp}\}$ , the  $j^{\text{th}}$  principal component  $(\vec{u}_j(\vec{x}))_{\vec{x} \in I}$  and its associated coefficients  $(w_j(t_k))_{k \in \{1, \dots, M_{\max}\}}$ , satisfying the following approximate relationship for all pixels  $\vec{x}$  at any time  $t$ :

$$\vec{u}(\vec{x}, t) \approx \vec{\mu}(\vec{x}) + \sum_{j=1}^{n_{cp}} w_j(t) \vec{u}_j(\vec{x}) \quad (2)$$

The formula above expresses the high-dimensional time-dependent DVF,  $\vec{u}(\vec{x}, t)$ , as a linear combination of a few static vector fields,  $\vec{u}_j(\vec{x})$ , weighted by the time-dependent PCA coefficients,  $w_j(t)$ . The latter are also referred to as the PCA weights or PCA scores in this work.  $\vec{\mu}(\vec{x})$  represents the temporal mean of  $\vec{u}(\vec{x}, t_k)$  over  $k \in \{1, \dots, M_{\text{train}}\}$ , and the principal components  $\vec{u}_j(\vec{x})$ , also called the principal DVFs in this article, are computed using the first  $M_{\text{train}}$  frames of each sequence as well; the selection of  $M_{\text{train}}$  is detailed in Section 2.3.3. To estimate the weights at time  $t_k$  when  $k \geq M_{\text{train}}$ , we project  $X_c(t_k)$  onto the principal components:

$$w_j(t) = \sum_{\vec{x} \in I} \langle \vec{u}(\vec{x}, t) - \vec{\mu}(\vec{x}), \vec{u}_j(\vec{x}) \rangle \quad (3)$$

In that equation,  $\langle \cdot, \cdot \rangle$  designates the Euclidean inner product, and the sum is over all pixels  $\vec{x}$  of the incoming image at time  $t$ . The principal components stay constant throughout each sequence, as the motion model is not updated as time elapses. Indeed, we assume that the breathing dynamics remain relatively stable within all sequences, since the latter are relatively short (approximately one minute) and show no extreme out-of-plane motion or changes in motion patterns. Eq. 3 follows directly from Eq. 2 by using the orthonormality of the  $2|I|$ -dimensional principal components:

$$\sum_{\vec{x} \in I} \langle \vec{u}_i(\vec{x}) | \vec{u}_j(\vec{x}) \rangle = \begin{cases} 1 & \text{if } i = j \\ 0 & \text{otherwise} \end{cases} \quad (4)$$

Appendix C provides the full mathematical derivation of Eqs. 2 and 3.

### 2.3. Prediction of the time-dependent PCA weights

In order to predict future frames in a given MRI sequence, we first forecast the PCA weights,  $w_j(t_k)$ . To this end, we compare various adaptive methods, namely standard

(i.e., vanilla) RNNs using online learning and least mean squares (LMS), and algorithms trained offline, namely transformers trained with backpropagation and an ordinary least squares (OLS) linear AR model. For brevity, we refer to the latter as linear regression in this article.

#### 2.3.1. Input and target definition

The input of all forecasting algorithms consists of the concatenation of the PCA coefficients  $w_j(t_n), \dots, w_j(t_{n+L-1})$  for each component index  $j \in \{1, \dots, n_{cp}\}$ , where  $L$  designates the signal history length (SHL)—the input window width—expressed in number of time steps. The scores  $w_1(t), \dots, w_{n_{cp}}(t)$  are predicted simultaneously to utilize temporal correlation information, thereby potentially increasing accuracy. A unit bias term is added to the input vector, providing more flexibility to the forecasting model; the input with bias is denoted as  $x_n$ . The output vector,  $y_{n+1}$ , consists of the coefficients at time  $t_{n+L+h-1}$ , where  $h$  refers to the horizon value expressed in number of time steps:

$$x_n = \begin{pmatrix} 1 \\ w_1(t_n) \\ w_2(t_n) \\ \dots \\ w_{n_{cp}}(t_n) \\ w_1(t_{n+1}) \\ \dots \\ w_{n_{cp}}(t_{n+L-1}) \end{pmatrix}, \quad y_{n+1} = \begin{pmatrix} w_1(t_{n+L+h-1}) \\ \dots \\ w_{n_{cp}}(t_{n+L+h-1}) \end{pmatrix} \quad (5)$$

#### 2.3.2. Model architectures and learning algorithms Standard RNNs trained dynamically

We first provide a brief description of the RNN models used in this study. To prevent overfitting in our low-data context, we adopt a minimal RNN architecture: a standard RNN with a single hidden layer of limited size,  $d \leq 110$ . Its hidden state vector  $s_n \in \mathbb{R}^d$  encodes past information and serves as the network's internal memory. At each time step, the state is updated by applying a non-linear activation function,  $\Phi$ , to a linear combination of the previous state,  $s_n$ , and current input,  $x_n$ . The output,  $y_{n+1}$ , is obtained through a linear transformation of the updated hidden state:

$$s_{n+1} = \Phi(A_n s_n + B_n x_n), \quad y_{n+1} = C_n s_{n+1} \quad (6)$$

In the equations above,  $A_n$ ,  $B_n$ , and  $C_n$  denote the hidden-to-hidden, input-to-hidden, and hidden-to-output learnable weight matrices, respectively. Their shape is  $d \times d$ ,  $d \times (n_{cp}L + 1)$ , and  $n_{cp} \times d$ . These matrices depend on the time step index  $n$ , as online learning algorithms update them continually.  $\Phi$  is set as the coordinate-wise hyperbolic tangent function. The RNN training algorithms compared in this study are RTRL, UORO, SnAp-1, and DNI; they minimize the instantaneous squared error between the latest prediction and incoming sample at each time step. We use the efficient vanilla-RNN implementations of UORO, SnAp-1, and DNI described in [38, 39] (see also Section 1.3). Gradient norm clipping is applied to LMS and RNNs to ensure numerical stability [85]. To provide a baseline scenario for comparison,

Prediction method	Mathematical model	Training/validation split	Range of hyperparameters in the tuning grid
RTRL, UORO SnAp-1, DNI	$s_{n+1} = \Phi(A_n s_n + B_n x_n)$ $y_{n+1} = C_n s_{n+1}$	28.3s/28.3s	$\eta \in \{0.005, 0.01, 0.015, 0.02\}$ $L \in \{1.9s, 3.8s, 5.7s, 7.6s, 9.5s\}$ $d \in \{10, 30, 50, 70, 90, 110\}$
LMS	$y_{n+1} = A_n x_n$	28.3s/28.3s	$\eta \in \{0.02, 0.05, 0.1, 0.2\}$ $L \in \{1.9s, 3.8s, 5.7s, 7.6s, 9.5s\}$
Linear regression	$y_{n+1} = A x_n$	50.4s/6.2s	$L \in \{1.9s, 3.8s, 5.7s, 7.6s, 9.5s\}$
Transformer encoder	$y_{n+1} = \text{FFN}_{\text{out}}\left(\text{vec}\left(E^{(n_{\text{layer}})} \circ \dots \circ E^{(1)}(A_{\text{in}} x_n + \text{PE})\right)\right)$ with $E^{(l)} = \text{FFN}^{(l)} \circ \text{MHA}^{(l)}$	Subject-specific: 50.4s/6.2s Population: first 80%/last 20% of each sequence (samples from all sequences are concatenated)	$\eta \in \{0.0001, 0.0005\}$ $L \in \{1.9s, 3.8s, 5.7s, 7.6s, 9.5s\}$ $d_{\text{model}} \in \{8, 16\}$
RNN with a frozen hidden layer	$s_{n+1} = \Phi(A s_n + B x_n)$ $y_{n+1} = C_n s_{n+1}$	Training 28.3s Validation 28.3s	$\eta \in \{0.02, 0.05, 0.1, 0.2\}$ $L \in \{1.9s, 3.8s, 5.7s, 7.6s, 9.5s\}$ $d \in \{10, 30, 50, 70, 90, 110\}$

**Table 2**

Overview of the forecasting techniques and validation schemes considered. The second column specifies the relationship between the input  $x_n$  containing the past PCA weights and the output  $y_{n+1}$  corresponding to the predicted weights (both defined in Eq. 5)<sup>2</sup>. The fourth column outlines the hyperparameter configuration evaluated using grid search.  $\eta$ ,  $L$ ,  $d$ ,  $n_{\text{layer}}$ , and  $d_{\text{model}}$  designate the learning rate of neural networks and LMS, the SHL<sup>3</sup>, the number of hidden units of the standard RNN architecture, and the number of layers and embedding dimension of the encoder-only transformer, respectively.

we also consider an RNN whose hidden parameter matrices,  $A$  and  $B$ , are randomly initialized and then frozen during inference (they do not depend on the time index  $n$ ), but whose output layer weights,  $C_n$ , are updated online. RNNs are fully implemented in MATLAB [86].

### Transformers

In this work, RNNs are compared with transformers, which benefit from long-range dependency modeling capabilities via self-attention. Specifically, we adopt an encoder-only architecture, appearing as a natural and data-efficient choice for deterministic time series forecasting. Indeed, we do not seek to generate sequences autoregressively using a decoder layer, unlike in many NLP applications, but rather focus on architectural simplicity for fixed-horizon regression. In our study, transformers are trained with backpropagation, contrasting with the RNNs which rely on online learning algorithms.

By abuse of notation, the transformer input,  $x_n$ , is reshaped as a matrix of size  $(n_{\text{cp}} + 1) \times L$ , where a bias term is added to each column. It is first linearly projected into

<sup>2</sup>The matrices  $A$  and  $A_n$ , both of size  $n_{\text{cp}} \times (n_{\text{cp}}L + 1)$ , correspond to the coefficients for linear regression and LMS, respectively. The latter coefficients depend on the time step index  $n$ , since they are updated each time a new incoming sample arrives, in opposition to the former.

<sup>3</sup>Due to the difference in sampling rates,  $L$ , expressed in number of time steps, is selected within  $\{6, 12, 18, 24, 30\}$  or  $\{11, 23, 34, 45, 57\}$  when testing is conducted on the ETH Zürich dataset or the OvGU dataset, respectively. For instance, for a population transformer using training examples constituted from the former dataset and resampled to 6Hz to match the OvGU test sequences, the possible range of values for  $L$  in the search grid will correspond to that frequency ( $\{11, 23, 34, 45, 57\}$ ). For sequence-specific models, the validation and test sets are extracted from the same sequence, so there is no resampling and the rule is straightforward.

a latent space of dimension  $d_{\text{model}}$ , via multiplication with the matrix  $A_{\text{in}}$ . Sinusoidal positional encodings, denoted by "PE", are then added to preserve temporal order. Subsequently, the sequence is processed by a succession of  $n_{\text{layer}}$  transformer-encoder layers. The resulting representation is flattened across both temporal and embedding dimensions ("vec" operator below) and passed through the output-head feed-forward network (FFN), denoted as  $\text{FFN}_{\text{out}}$ . The latter stacks two linear layers separated by a rectified linear unit (ReLU) activation:

$$y_{n+1} = \text{FFN}_{\text{out}}\left(\text{vec}\left(E^{(n_{\text{layer}})} \circ \dots \circ E^{(1)}(A_{\text{in}} x_n + \text{PE})\right)\right) \quad (7)$$

Each encoder layer,  $E^{(l)}$ , consists of multi-head self-attention (with two heads),  $\text{MHA}^{(l)}$ , followed by a position-wise FFN, denoted as  $\text{FFN}^{(l)}$ :

$$E^{(l)} = \text{FFN}^{(l)} \circ \text{MHA}^{(l)} \quad (8)$$

In contrast with the online RNN algorithms investigated, which only "see" each training example once, as they perform one-shot sequence forecasting and learn parameters during that process, transformers are shown the same examples multiple time during training, as we minimize the mean squared error (MSE) loss of the training set across multiple epochs. The optimization algorithm selected for transformers is adaptive momentum (ADAM). Shuffling is applied during training, at each epoch, to prevent bias from data ordering and improve convergence stability. Similar to RNNs, transformer capacity is kept relatively low ( $d_{\text{model}} \leq 16$ ,  $n_{\text{layer}} \leq 2$ , and position-wise FFN dimension below 32) to speed up computations and avoid overfitting, given the

small dataset size, while preserving sufficient expressivity. In addition, dropout is applied to the encoder layers with a high probability ( $p = 0.5$ ) for further regularization. Nonetheless, weight decay is not applied. Transformers are implemented using the Pytorch library in Python [86]. The parameters relative to RNNs and transformers are summarized in Table 2 and Table 10 (in Appendix D).

### 2.3.3. Training and validation schemes

#### Overview

We compare two types of models, namely sequence-specific models and population models. For sequence-specific models, the train/validation/test splits are within the same sequence, with offline methods using a relatively longer training window. By contrast, the population transformer is trained and validated on one dataset, and testing is conducted using the end of the sequences from the other dataset, so that evaluation remains consistent for both model categories. We recall that registration and motion modeling with PCA are sequence-specific, regardless of the forecasting method employed (Section 2.2). When using the OvGU dataset, we use the terms "sequence-specific" and "subject-specific" interchangeably, as each subject corresponds only to one 2D MR image sequence (this is not true for the ETH Zürich dataset). During hyperparameter tuning, we optimize  $L$  for all algorithms, the learning rate of LMS and neural networks (RNNs and transformers), denoted by  $\eta$ , the number of RNN hidden units, and the number of layers and embedding dimension of the transformer (Table 2).

In our experiments, we study the influence of the horizon  $h \in \{1, \dots, h_{\max}\}$ , with  $h_{\max}$  corresponding to 2.2s, on prediction accuracy. In other words, we set  $h_{\max} = 7$  for the ETH Zürich dataset and  $h_{\max} = 13$  for the OvGU dataset, due to the difference in sampling rates. All models are specific to a given horizon  $h$ , that is, we perform training and validation separately for each value of  $h$  considered. This choice—avoiding recursive forecasting—prevents error accumulation and should lead to higher performance.

#### Sequence-specific models

For sequence-specific models, each time series is split into training and validation sets totaling together 56.6s, corresponding to its beginning, and a test set of duration 6.3s and 26.3s for the ETH Zürich and OvGU datasets, respectively, corresponding to its end. The training set comprises the data between 0s and  $t_{M_{\text{train}}} = 28.3\text{s}$ , except for offline methods (linear regression and transformers), whose training period is set to end at  $t_{M_{\text{train}}} = 50.4\text{s}$ , as using more training data may benefit them.  $M_{\text{train}}$  denotes the last time index of the training set; its value depends also on the dataset, due to the difference in sampling rates (Table 11 in Appendix D). Prior to forming the input vectors  $x_n$  via Eq. 5, each incoming PCA score  $w(t) = [w_1(t), \dots, w_{n_{cp}}(t)]$  is standardized using the mean and standard deviation over the training set (i.e., over  $t \leq t_{M_{\text{train}}}$ ), accelerating the convergence of stochastic gradient descent. Predictions on the validation and test sets are mapped back to the original scale.

The validation segment corresponds to the time indices  $k \in \{M_{\text{train}} + 1, \dots, M_{cv}\}$ , where  $t_{M_{cv}} = 56.6\text{s}$  for all forecasting methods considered (Table 11). We select the hyperparameters in the grid that minimize the validation normalized root-mean-square error (nRMSE) of the validation set, defined in the following equation (with  $k_{\min} = M_{\text{train}} + 1$  and  $k_{\max} = M_{cv}$ ):

$$nRMSE = \sqrt{\frac{\sum_{k=k_{\min}}^{k_{\max}} \sum_{j=1}^{n_{cp}} (\widehat{w}_j(t_k) - w_j^{true}(t_k))^2}{\sum_{k=k_{\min}}^{k_{\max}} \sum_{j=1}^{n_{cp}} (\overline{w}_j^{true} - w_j^{true}(t_k))^2}} \quad (9)$$

In that equation, for each component order  $j \in \{1, \dots, n_{cp}\}$ ,  $w_j^{true}(t_k)$ ,  $\widehat{w}_j(t_k)$ , and  $\overline{w}_j^{true}$  designate the reference (i.e., ground-truth) PCA score at time  $t_k$ , computed by projecting the deformations associated with the incoming image onto the linear subspace spanned by the principal DVFs (Eq. 3), the predicted score at time  $t_k$ , and the mean of  $w_j^{true}(t_k)$  for  $k \in \{k_{\min}, \dots, k_{\max}\}$ , respectively. For sequence-specific models, the hyperparameters selected for testing depend both on the horizon  $h$  and the sequence being processed.

Because neural networks are stochastic algorithms (e.g., due to random parameter initialization),  $\widehat{w}_j(t)$ , and by extension the validation nRMSE (Eq. 9), depend on the run index. Consequently, given each possible combination of hyperparameters in the tuning grid (Table 2), we average that error over  $n_{cv}$  successive runs (each with a different random seed). This averaged error is minimized to determine hyperparameters during validation with neural networks. We set  $n_{cv} = 250$  for RNN algorithms, except RTRL, for which we select  $n_{cv} = 10$ , as the latter was more computationally intensive but experimentally yields error measurements with lower uncertainty. This is possibly due to exactness in the gradient computation in RTRL; the other RNN algorithms involved are indeed approximations of RTRL. By contrast, UORO and DNI were associated with larger confidence intervals (CI) when computing average accuracy metrics for each sequence<sup>4</sup>, which can be linked with stochasticity in the loss gradient update in UORO and random initialization of the linear coefficients involved in error-signal estimation in DNI. We also set  $n_{cv} = 10$  for the sequence-specific transformer, reflecting the higher computational resources that it needs for training.

#### The population transformer

Besides training sequence-specific models, we also consider a population transformer that was trained on multiple sequences outside the test set. Specifically, when performing evaluation with the ETH Zürich dataset, that model is trained on the OvGU dataset, and vice versa, ensuring subject-wise and scanner-wise splitting. The training set is formed using batches from the first 80% of each training sequence; the last 20% is used for validation. We do not use the whole separate dataset for testing, but only the end of

<sup>4</sup>This is not reflected in Tables 3 and 4, where the performance on one sequence averaged over  $n_{\text{test}}^{\text{PCA}}$  runs and  $n_{\text{test}}$  runs, respectively, is treated as one sample.

each sequence (starting from 56.6s), ensuring that evaluation remains consistent across both the population transformer and sequence-specific models. Because the sampling frequency of each dataset is different, we resample the PCA weights  $w(t)$  of the training/validation set to match that of the test set, using bandlimited finite impulse response (FIR) interpolation via polyphase filtering (SciPy library). The training and validation data is standardized using the mean and standard deviation of all concatenated samples in the training set. When evaluating performance on the test sequences, the PCA weights are first standardized using the portion corresponding to the first 50.4s, before feeding the inputs  $x_n$  to the population model, similar to inference with sequence-specific offline models. The transformer output is then scaled back to calculate accuracy metrics. Specifically, when conducting inference with the population transformer, standardization does not involve data from the training set but only from the sequence we are evaluating on. To handle stochasticity, we train  $n_{cv} = 5$  different models per horizon. During grid search, we select the hyperparameters minimizing the RMSE of the validation set—the numerator in the right-hand side of Eq. 9—averaged over the  $n_{cv}$  models. The hyperparameter grid for the population transformer is the same as that for sequence-specific transformers (Table 2). The Optuna Python library was used to tune the population transformers specifically [87]. In contrast with the sequence-specific models, the hyperparameters relative to population transformers depend only on the specified horizon  $h$ , not on the test sequences.

The number of epochs associated with cross-subject transformers (300 epochs) is set higher than for sequence-specific ones (50 epochs), as a lower value for the latter acts as lightweight regularization, helping counteract more prominent data scarcity, and training time is less critical for the former. After hyperparameter selection, the final population model is trained with early stopping, terminating training if the validation loss did not improve for 30 consecutive epochs, potentially improving generalization. To further prevent overfitting with cross-subject models, especially as PCA semantics between the ETH Zürich and OvGU acquisitions may misalign and breathing patterns in both datasets may not exactly match, we apply stochastic data augmentation to each batch in the training set, operating per feature and mirroring all relevant transformations on the targets to preserve input–output consistency. Specifically, we (i) scale amplitudes by a factor drawn from a configured range (with a probability  $p = 0.8$  and a range between 0.8 and 1.2), (ii) permute feature channels ( $p = 0.5$ ), (iii) add a constant baseline bias (offset) proportional to the amplitude of the input window signal ( $p = 0.3$ , multiplicative factor  $\leq 0.2$ ) (iv) inject a linear drift (time-dependent slope) with a magnitude scaled to the amplitude of the features ( $p = 0.3$ , slope  $\leq 0.05$ ). The amplitude of the past PCA coefficients within a given window are estimated robustly as the 5th–95th percentile range to normalize the strength of bias and drift. Random noise was not injected during data augmentation as the PCA signals were already noisy.

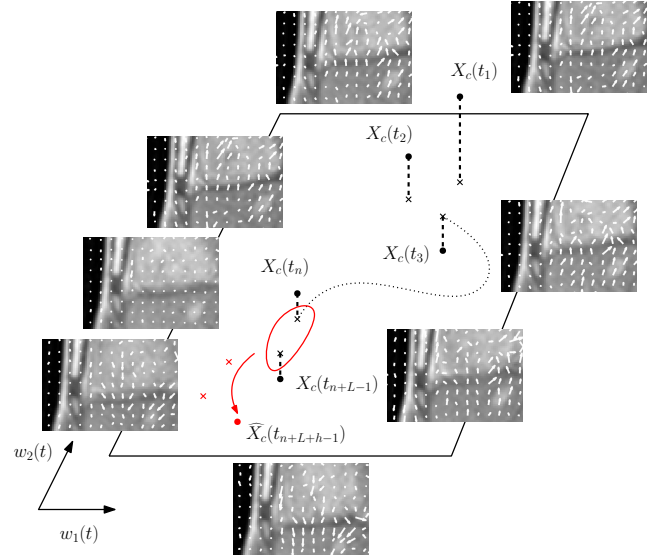


**Figure 2:** Geometrical interpretation of the motion prediction process. The flattened, centered DVF at time  $t$ ,  $X_c(t)$ , lies in a  $2|I|$ -dimensional space, with  $|I|$  denoting the number of pixels. It is projected onto the  $n_{cp}$ -dimensional linear subspace spanned by the principal components. The coordinates of this projection are the PCA weights,  $w_j(t)$  (Eq. 3). The DVF predicted at horizon  $h$  from the past time steps  $n, \dots, n+L-1$ ,  $\widehat{X}_c(t_{n+L+h-1})$ , also lies in that subspace. The case illustrated corresponds to  $h = 3$ ,  $L = 2$ , and  $n_{cp} = 2$ . The diaphragm region from sequence 1 of the ETH Zürich dataset (frames  $t_{36}$ – $t_{43}$ ) and the corresponding Lucas–Kanade optical-flow are shown for illustration. The origins of each of the displayed 2D displacement vectors are separated from each other by 6 pixels.

## 2.4. Image prediction

We estimate the future DVFs by plugging the predicted PCA weights,  $\widehat{w}_j(t_{k+h})$ , where  $h$  designates the prediction horizon, in Eq. 2:

$$\vec{u}(\vec{x}, t_{k+h}) \approx \vec{\mu}(\vec{x}) + \sum_{j=1}^{n_{cp}} \widehat{w}_j(t_{k+h}) \vec{u}_j(\vec{x}) \quad (10)$$

By doing so, we assume that the predicted motion lies in the  $n_{cp}$ -dimensional linear subspace spanned by the principal DVFs computed using the first  $M_{\text{train}}$  images (cf. Fig. 2 for a geometrical illustration). The future frames are synthesized by warping the initial image according to the predicted DVFs (Fig. 3). This operation maps each pixel in the source frame to a new, generally non-integer location in the target frame—the tip of its associated displacement vector. Since intensity values are then required at integer pixel coordinates on the regular grid, they must be interpolated. To achieve this, we perform Nadaraya-Watson regression, whose implementation in this work follows that in [37] (Fig. 4). Our strategy implicitly relies on the assumptions that the motion field

<sup>5</sup>Includes content from [37], Copyright 2024, with permission from Elsevier.

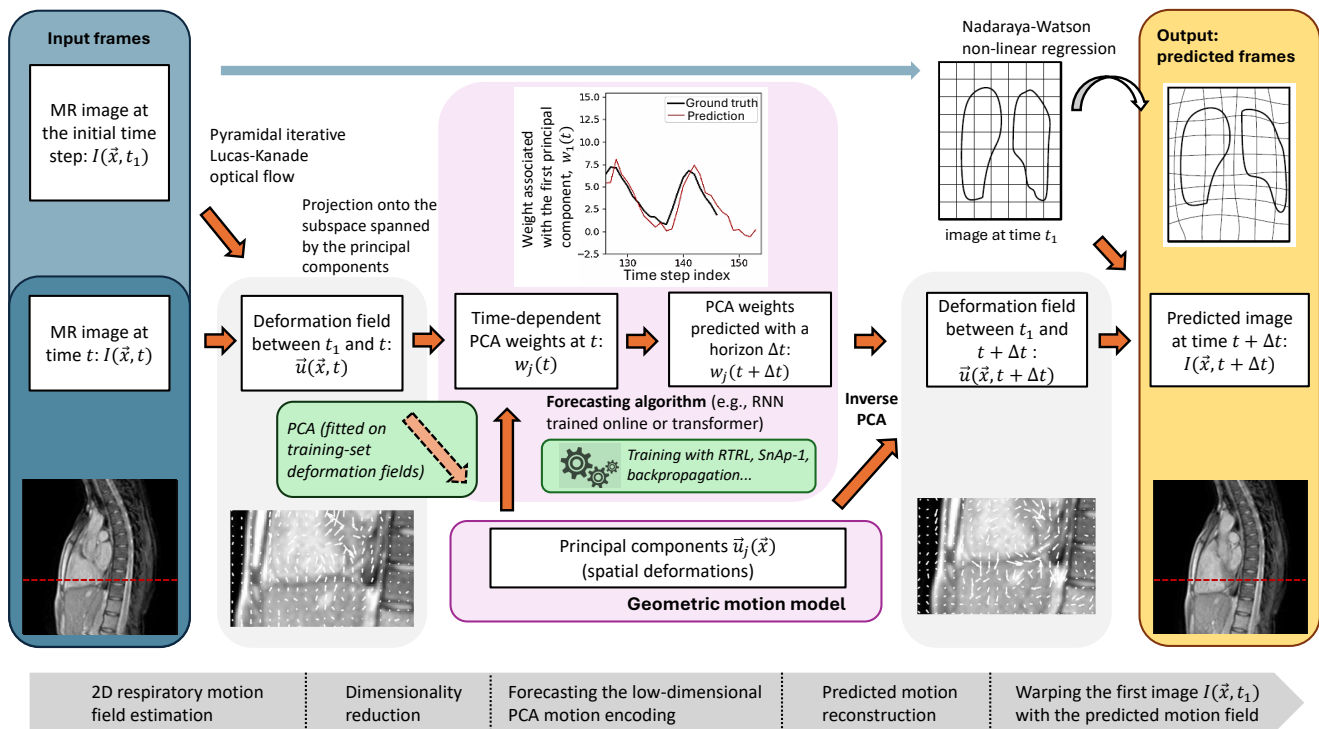


**Figure 3:** Pipeline of the proposed modular algorithm, combining motion estimation, PCA, and time-series forecasting. The algorithm input consists of the MR frames at times  $t_1$  and  $t$  (blue boxes). First, the optical-flow algorithm computes the deformations between them. During training, PCA is fitted using these deformations, producing a small set of spatial principal components and corresponding time-dependent weights, which a forecasting method learns to predict (green boxes). During inference, current weights are estimated by projecting the optical-flow field at time  $t$  onto the PCA components and are forecast by the trained model. The reference image is warped by the resulting reconstructed DVF, yielding the predicted frame at  $t + \Delta t$  (yellow box)<sup>5</sup>.

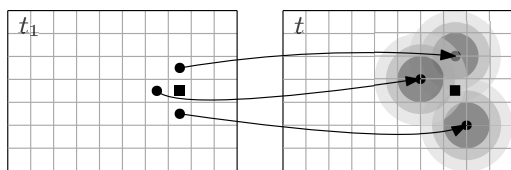


**Figure 4:** Warping the first image (at time  $t_1$ ) using Nadaraya-Watson regression with a Gaussian kernel. The closer a point in the source image lands to the square point in the target image (at time  $t$ ), the more it influences the intensity of that target pixel at  $t$ <sup>6</sup>

is reasonably smooth (i.e., mostly invertible) and that out-of-plane motion, artifacts, and brightness variations corresponding to the same tissue patch throughout the video are minimal.

To evaluate the performance of neural networks while accounting for randomness in the initialization and updates of their parameters, we run the image forecasting pipeline  $n_{\text{test}}$  times, each corresponding to a different seed and thereby, different predicted PCA coefficients,  $\hat{w}_j(t_{k+h})$ . The latter yield  $n_{\text{test}}$  versions of the predicted DVF, each used to warp the initial image. Subsequently, the accuracy metrics of the test set are averaged over the  $n_{\text{test}}$  runs.  $n_{\text{test}}$  was chosen

<sup>6</sup>Reprinted from [37], Copyright 2024, with permission from Elsevier.

such that  $n_{\text{test}} \leq n_{\text{cv}}$ , reflecting the computational cost of the warping process (Table 11). In the following, by abuse of notation, when it is clear from the context that  $w_j(t)$  refers to the predicted coefficient, we do not explicitly write  $\hat{w}_j(t)$ , for simplicity.

## 2.5. Optimization of the PCA subspace dimension

For the population transformer, we arbitrarily set the number of principal components to  $n_{cp} = 3$ , following common practices in respiratory motion modeling [66, 12]. For sequence-specific methods, the PCA subspace dimension,  $n_{cp}$ , is selected as explained below. First, for each value of  $n_{cp} \in \{1, 2, 3, 4\}$ , the hyperparameters minimizing the nRMSE of the validation set (Eq. 9) are determined following the procedure described in Section 2.3.3. To choose the optimal value of  $n_{cp}$ , we minimize the registration error,  $E_{\text{pred}}(n_{cp})$ , defined below in Eq. 13, characterizing the predicted DVFs computed using those hyperparameters and the first  $n_{cp}$  components,  $\vec{u}^{(i)}(n_{cp})$ , where  $i$  designates the run index.

We first define  $\delta(\vec{u}, \vec{x}, t)$ , the local instantaneous absolute registration error at pixel  $\vec{x}$  and time  $t$ , for a 3D (2D + time) vector field  $\vec{u}$ :

$$\delta(\vec{u}, \vec{x}, t_k) = |I(\vec{x} + \vec{u}(\vec{x}, t_k), t_k) - I(\vec{x}, t_1)| \quad (11)$$

Using the latter quantity, one can calculate  $\epsilon(\vec{u}, t_k)$ , the instantaneous normalized root-mean-square (RMS) registration error at time  $t_k$  using the vector field  $\vec{u}$ :

$$\epsilon(\vec{u}, t_k) = \sqrt{\frac{\sum_{\vec{x}} \delta(\vec{u}, \vec{x}, t_k)^2}{\sum_{\vec{x}} (\bar{I}(t_1) - I(\vec{x}, t_1))^2}} \quad (12)$$

In that expression,  $\bar{I}(t_1)$  designates the mean intensity of the initial image. This error, evaluated using  $\vec{u}^{(i)}(n_{cp})$ , is averaged over the validation time steps and  $n_{cv}^{\text{dim}}$  evaluation runs to account for neural network stochasticity:

$$E_{\text{pred}}(n_{cp}) = \frac{1}{n_{cv}^{\text{dim}} (M_{cv} - M_{\text{train}})} \sum_{i=1}^{n_{cv}^{\text{dim}}} \sum_{k=M_{\text{train}}+1}^{M_{cv}} \epsilon(\vec{u}^{(i)}(n_{cp}), t_k) \quad (13)$$

$E_{\text{pred}}(n_{cp})$  is referred to as the (mean) normalized RMS registration error; we choose the value of  $n_{cp}$  minimizing that error. Computing this metric is relatively inexpensive, as it does not require warping the initial image at  $t_1$ . The number of averaging runs,  $n_{cv}^{\text{dim}}$ , is set equal to that used for test-set image prediction accuracy,  $n_{\text{test}}$ , with  $n_{cv}^{\text{dim}} = 1$  for deterministic algorithms. The overall experimental setting and related parameters are outlined in Figs. 3 and Table 11.

## 3. Results

### 3.1. Breathing motion modeling with PCA

The optical flow near the diaphragm mainly followed the SI tissue motion associated with breathing. In sequence 1 of the ETH Zürich dataset, the deformation vectors mostly pointed downwards during inspiration and upwards during expiration (Figs. 2, 6a, and 6b), as the initial frame corresponds to a middle phase in the cycle (background in Fig. 6c). Their average over  $t \leq t_{90}$ ,  $\mu(\vec{x})$ , did not capture a major vertical displacement trend around the liver or diaphragm, reflecting the absence of respiratory drift (Fig. 6c). Artifacts and transverse motion causing sudden brightness variations led to relatively high fluctuations of the norms of the deformation vectors, for example, near the sternum and lower back. In general, the optical flow did not homogeneously lie vertically, as each organ moves and deforms in a specific way. Results regarding DIR parameter optimization can be found in Appendix B.

The first-order principal DVF in sequence 1 of the ETH Zürich dataset was associated with expansion and contraction of the right cardiac ventricle and internal liver deformation (Fig. 6d). By contrast, the second PCA component mainly reflected respiratory motion, with most deformation vectors within the thoracic cavity leaning downwards uniformly (Fig. 6e). The third component combined vertical respiratory elements, with motion vectors pointing superiorly or towards the posterior side of the body, and heart deformation (Fig. 6f). Periodic intensity variations around the sternum and lumbar regions, largely due to transversal displacement, were also captured by these three components.

Likewise, in the fourth ETH Zürich sequence, the first-order principal DVF corresponded to liver deformations and out-of-plane motion artifacts localized at the back area (Fig. 7a). The vectors forming the second component aligned upwards relatively homogeneously, reflecting breathing (Fig. 7d). By contrast, regarding the OvGU dataset, the first principal component in each sequence primarily represented the prevailing SI constituent of respiratory motion (Fig. 9). The antero-posterior displacements of the upper abdominal organs, particularly those located below the liver and near the anterior abdominal wall, were also reflected in that first component, notably in sequence 6. In all sequences, the norm of the components  $\vec{u}_j(\vec{x})$  in air/background regions tended to increase with  $j$ , consistent with PCA progressively capturing variance attributable to noise (not displayed for brevity).

Correspondingly, the time-varying PCA weights became noisier and their amplitude decreased as the component order increased (Fig. 7). Temporal noise and instability were more pronounced in the ETH Zürich sequences, owing to their lower acquisition rate and the presence of cardiac motion (with higher characteristic frequency). Respiratory motion was associated with the most regular and cyclical PCA coefficients. Noticeably, in the ETH Zürich dataset, both the higher frequency and stronger amplitude variations associated with breathing in sequence 4, compared to sequence 1, were reflected in the oscillations of the second-order weight, primarily capturing breathing (Figs. 7e and 8c). Nonetheless, the peaks of most coefficients exhibited some degree of synchronization, suggesting that PCA may not have fully isolated respiratory motion into a single mode of deformation. Incidentally, the first-order coefficient in sequence 1 was very similar to the second-order one in sequence 2 (not shown here for brevity), also linked to liver deformations, even though the cross-sections differed visually. This happened as both were extracted from the same 4D-MRI acquisition, reflecting the motion modeling capabilities of PCA. In the OvGU dataset, the first-order weight trajectories followed the respiratory motion apparent in the cine-MR images, despite the latter's high noise and low contrast, and captured irregularities in amplitude and frequency. Across both datasets, the coefficients (and components) corresponding to online and offline learning remained similar, even though  $M_{\text{train}}$  was set to a value approximately twice lower for the former (Figs. 8 and 9). This mainly stems from information redundancy inherent to the quasi-periodic nature of respiratory motion.

### 3.2. Prediction of the time-dependent PCA weights

#### 3.2.1. Quantitative evaluation on the ETH Zürich dataset

In this section, we discuss PCA weight-forecasting performance on the ETH Zürich acquisitions, setting  $n_{cp} = 3$  and performing PCA separately for each sequence using the first 28.3s to compare all algorithms using identical time

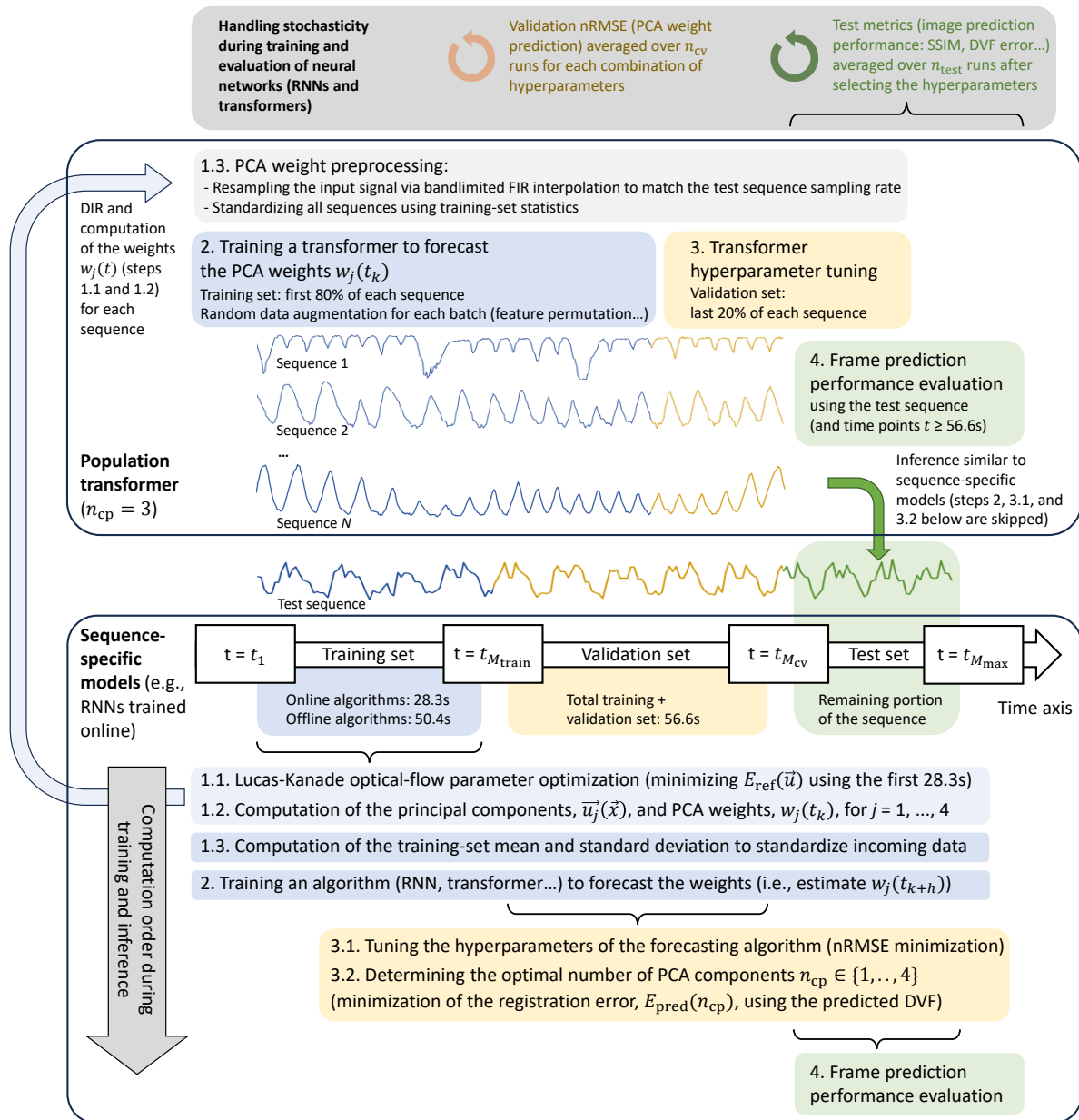


**Figure 5:** Overall experimental setting, summarizing the sequence-specific and population specific workflows, including DIR, PCA weight computation, model training and evaluation, and stochasticity mitigation. Only the first-order weight is represented for each sequence for clarity. The end of the population-model training sequences is visually aligned with the start of the test-set period, emphasizing that all algorithms are evaluated on the same test segment for consistency; in practice, sequence durations vary and this alignment is schematic.

series<sup>7</sup>; sequence-specific offline algorithms are still trained over the first 56.6s.

Performance is quantified as the nRMSE of the test set between the predicted and ground-truth time-dependent PCA weights (Eq. 9 with  $k_{min} = M_{cv} + 1 = 181$  and  $k_{max} = 200$ ). For neural networks, results are averaged over  $n_{test}^{PCA}$  evaluation runs; we set  $n_{test}^{PCA}$  to the same value

<sup>7</sup>This differs from the end-to-end frame-prediction pipeline (Sections 2.3.3 and 2.5), where offline models use PCA fitted on the first 50.4s and  $n_{cp}$  is selected via a validation-based procedure.

as  $n_{cv}$ , for simplicity. SnAp-1 and RTRL achieved the lowest prediction nRMSEs (averaged over the four sequences and horizon values examined,  $h \leq 2.20s$ ), followed by the sequence-specific transformer, DNI and then UORO (Table 3). The naive predictor using the latest weight as the prediction (i.e., a PCA-score persistence model) yielded the worst accuracy, followed by the population transformer. Although the population transformer significantly underperformed relative to the sequence-specific models, with non-overlapping 70% CIs, those associated with the latter models intersected—likely due to the limited number of sequences

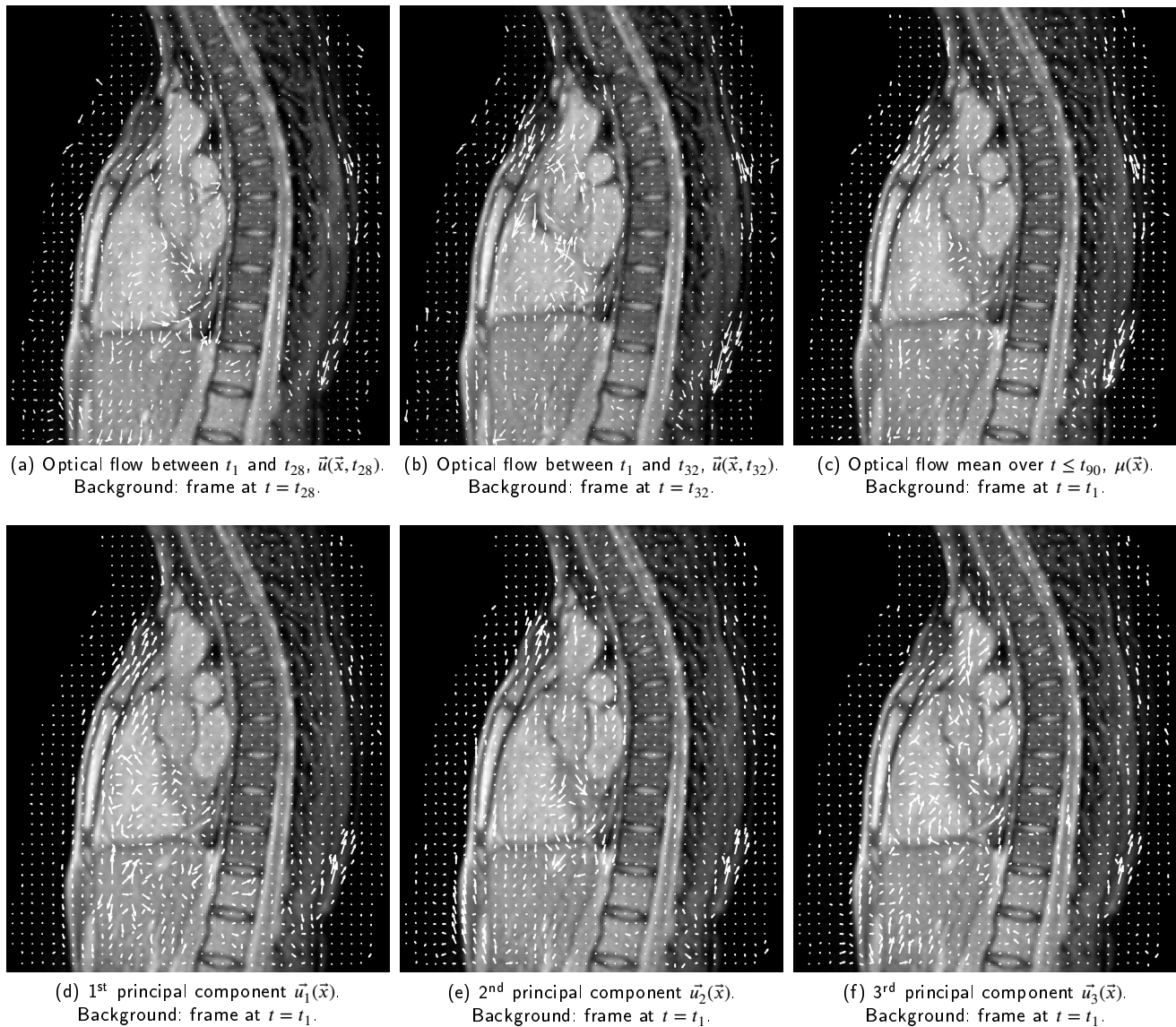


**Figure 6:** Top row: Lucas–Kanade optical flow in sequence 1 of the ETH Zürich dataset during inspiration (left,  $t = t_{28}$ ) and expiration (middle,  $t = t_{32}$ ), and its temporal average between  $t_1$  and  $t_{90}$ . Bottom row: first three principal components, computed using the first 90 frames of the MRI sequence (online learning setting). Deformable registration parameters were optimized by grid search using the same first 90 images (Appendix B). The origins of each of the displayed 2D displacement vectors are separated from each other by 6 pixels. The principal components were multiplied by a scalar coefficient equal to 500, and in each subfigure, the black borders with null vectors on the left and right sides were removed, to enhance visualization. Best viewed with zoom-in on a digital display.

( $N = 4$ ). Errors generally increased with  $h$  (Fig. 10). The sequence-specific transformer led to the lowest sequence-mean nRMSEs at  $h = 0.31$ s and  $h = 0.62$ s (0.781 and 0.815, respectively); that of the linear AR model at  $h = 0.31$ s (0.787) was comparable. SnAp-1 outperformed all other algorithms when  $h \geq 0.94$ s, with associated nRMSEs below 0.879, and was nearly matched by RTRL, suggesting that the diagonal influence-matrix approximation was accurate. Linear regression resulted in lower accuracy than all RNN methods when  $h \geq 0.94$ s, except the baseline with a frozen hidden layer.

The validation nRMSEs for UORO, SnAp-1, and DNI (Eq. 9 with  $k_{min} = M_{train} + 1 = 161$  and  $k_{max} = M_{cv} = 180$ ) generally increased with  $h$ , corroborating our previous observations regarding the test-set errors (Fig. 11). These three algorithms attained the minimum of the sequence-mean validation nRMSE (averaged over  $h \leq 2.20$ s) at  $L = 12$  time steps, corresponding to a history window of 3.77s. Furthermore, the value of  $\eta$  minimizing that error was 0.01 for both UORO and DNI and 0.02 for SnAp-1. Concerning the latter algorithm, the validation error decreased both with  $\eta$  and  $d$ , irrespective of  $h$ .

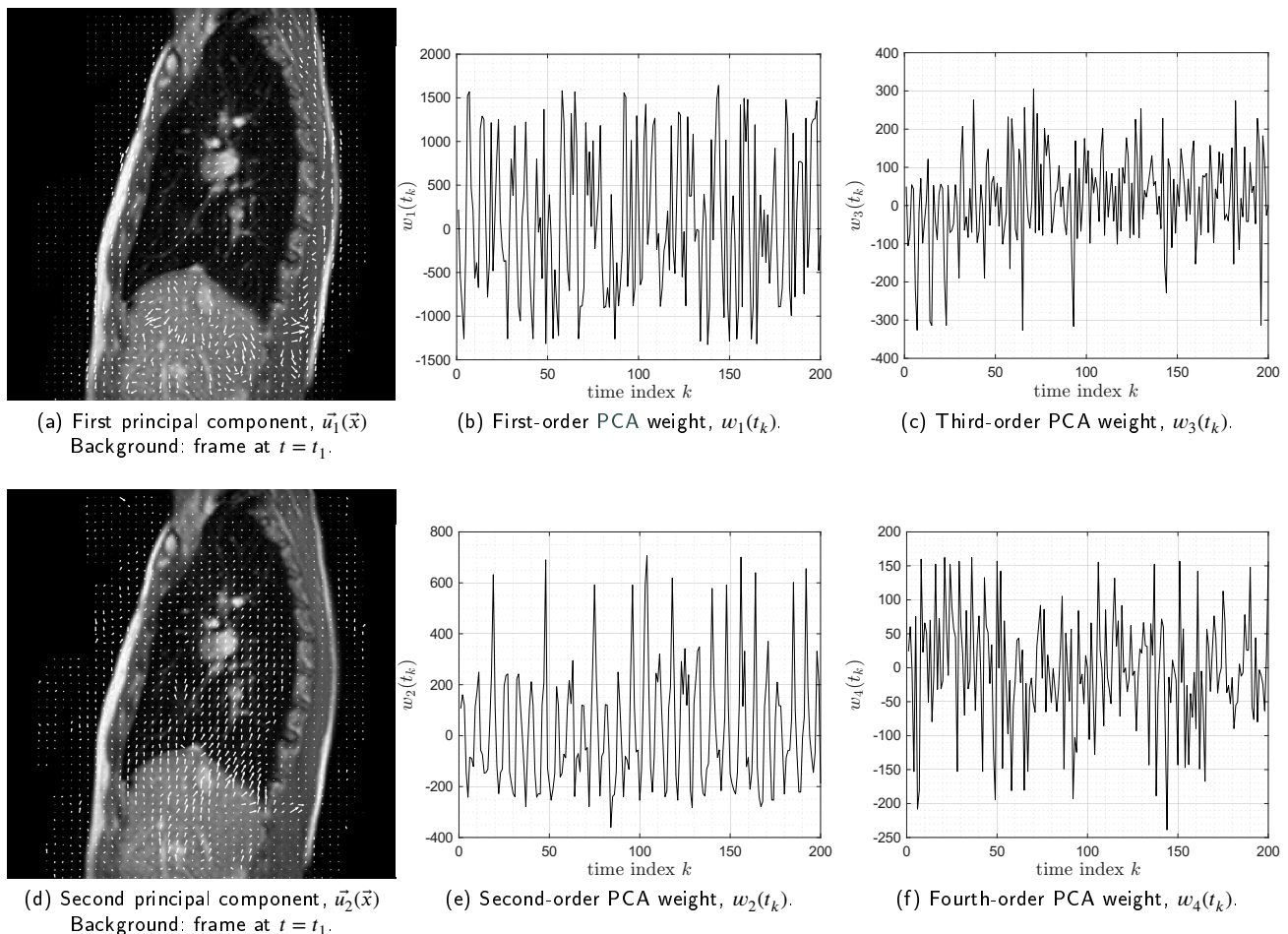


**Figure 7:** First two principal components associated with sequence 4 of the ETH Zürich dataset, computed using the first 90 frames (online learning setting), and corresponding first four time-dependent PCA coefficients. Same remarks as in Fig. 6 regarding principal displacement vector spacing, scaling, and visualization.

### 3.2.2. Qualitative evaluation

In what follows,  $n_{cp}$  is selected using the validation set, and the number of frames used to fit PCA depends on the algorithm type (online or offline), as detailed in Sections 2.3.3 and 2.5. Regarding sequence 1 of the ETH Zürich dataset, the RTRL predictions seemed generally visually correct in general, although their extrema did not perfectly match those of the ground truth, especially for the third-order weight, possibly due to the short acquisition time of 62.8s combined with the low sampling rate (Fig. 8). The predictions of the population transformer seemed relatively less accurate. At short horizons ( $h = 0.31s$ ), they captured the general trends but were overly oscillatory and tended to overshoot near the extrema. At medium-to-long horizons, forecasts for the second-order weight remained moderately faithful overall—yet with suboptimal extrema—whereas those corresponding to the other weights were low-amplitude and inaccurate.

On the OvGU dataset, the subject-specific transformer was qualitatively less accurate than UORO, SnAp-1, and DNI regarding prediction of the PCA weights at  $h = 1.66s$  (Fig. 9). The stronger respiratory motion irregularities in this dataset, both in amplitude and frequency, combined with that

relatively long horizon, likely amplified the negative impact of training-data scarcity on offline algorithms compared with online ones. Motion variability was generally higher near the EI phase, making it harder to predict. Forecasting appeared particularly challenging in sequence 4, which featured more pronounced amplitude fluctuations, including deep inspirations around  $t = 28s$  and  $t = 52s$ . Although the three RNN algorithms above performed reasonably well across all breathing traces, they also exhibited substantial high-frequency oscillations at  $h = 1.66s$  occurring, for instance, around the large-amplitude irregularities in sequence 4. The occasionally lower amplitude of early RNN forecasts reflects the adaptation period (warm-up) typical of online training from scratch before convergence stabilizes (see the RTRL and UORO predictions in Figs. 8 and 9d, respectively).

### 3.3. Optimization of the PCA subspace dimension

In this section, we examine the optimization of  $n_{cp}$  for sequence-specific methods on the ETH Zürich dataset, following the procedure described in Section 2.5 (step 3.2 in Fig. 5). The same selection strategy was applied to the OvGU acquisitions when performing video prediction, to ensure

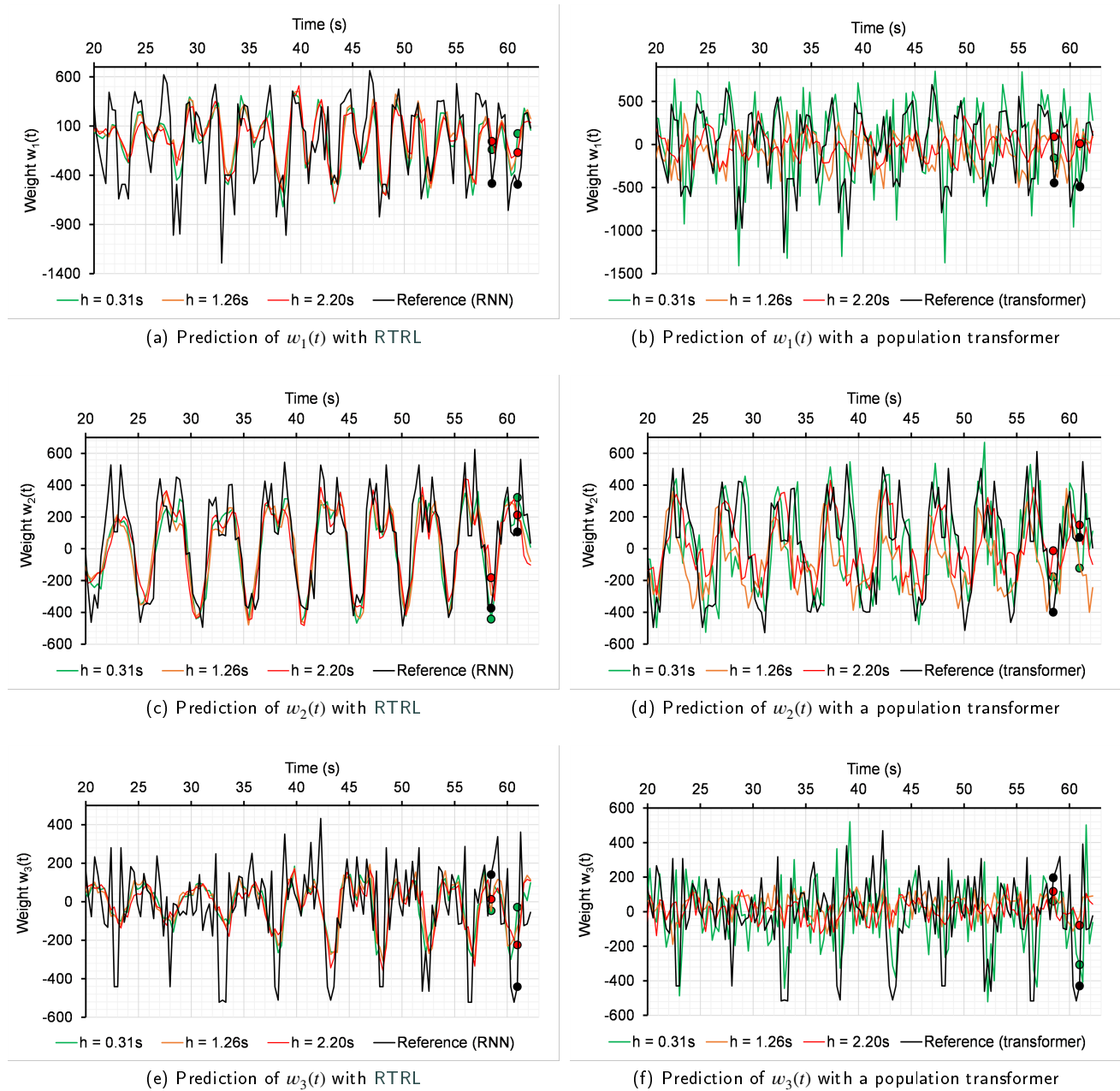


**Figure 8:** Prediction of the time-dependent PCA weights associated with sequence 1 of the ETH Zürich dataset for different horizon values  $h$  using an RNN trained with RTRL and a population transformer trained with the OvGU data. Hyperparameters, including  $n_{cp}$  for RTRL, were selected by grid search on the validation set for each value of  $h$  (Sections 2.3.3 and 2.5). Accordingly, the algorithms were trained to predict the first three PCA coefficients, except RTRL at  $h = 2.20s$ , for which  $n_{cp} = 4$  resulted in higher validation accuracy ( $w_4(t)$  is not represented due to space constraints). The reference weights were computed using the first 28.3s and 50.4s of the sequence for RTRL and the population transformer, respectively. Test-set evaluation only involves data beyond 56.6s, but earlier predictions are displayed to better assess prediction quality visually. Round markers at  $t = 58.4s$  and  $t = 60.9s$  correspond to the predicted images shown in Fig. 15, as both figures depict the same forecasting runs.

comparability across experiments. The registration error of the validation set using the predicted DVF,  $E_{pred}(n_{cp})$ , defined in Eq. 13, generally increased with  $h$  (Fig. 12), with more pronounced variations for offline algorithms, aligning with our previous observations in Figs. 8, 10, and 11. For all algorithms and horizons, the mean of  $E_{pred}(n_{cp})$  over the four sequences attained its maximum at  $n_{cp} = 1$ ,

reflecting that the primary respiratory mode was captured by the second-order principal component in three of the four ETH Zürich acquisitions (Section 3.1). The variations of  $E_{pred}(n_{cp})$  between  $n_{cp} = 2$  and  $n_{cp} = 4$  were moderate compared to the sharp error drop when increasing  $n_{cp}$  from 1 to 2. Choosing  $n_{cp} = 2$  was generally optimal for LMS, with a clear increase of  $E_{pred}(n_{cp})$  across most horizons as

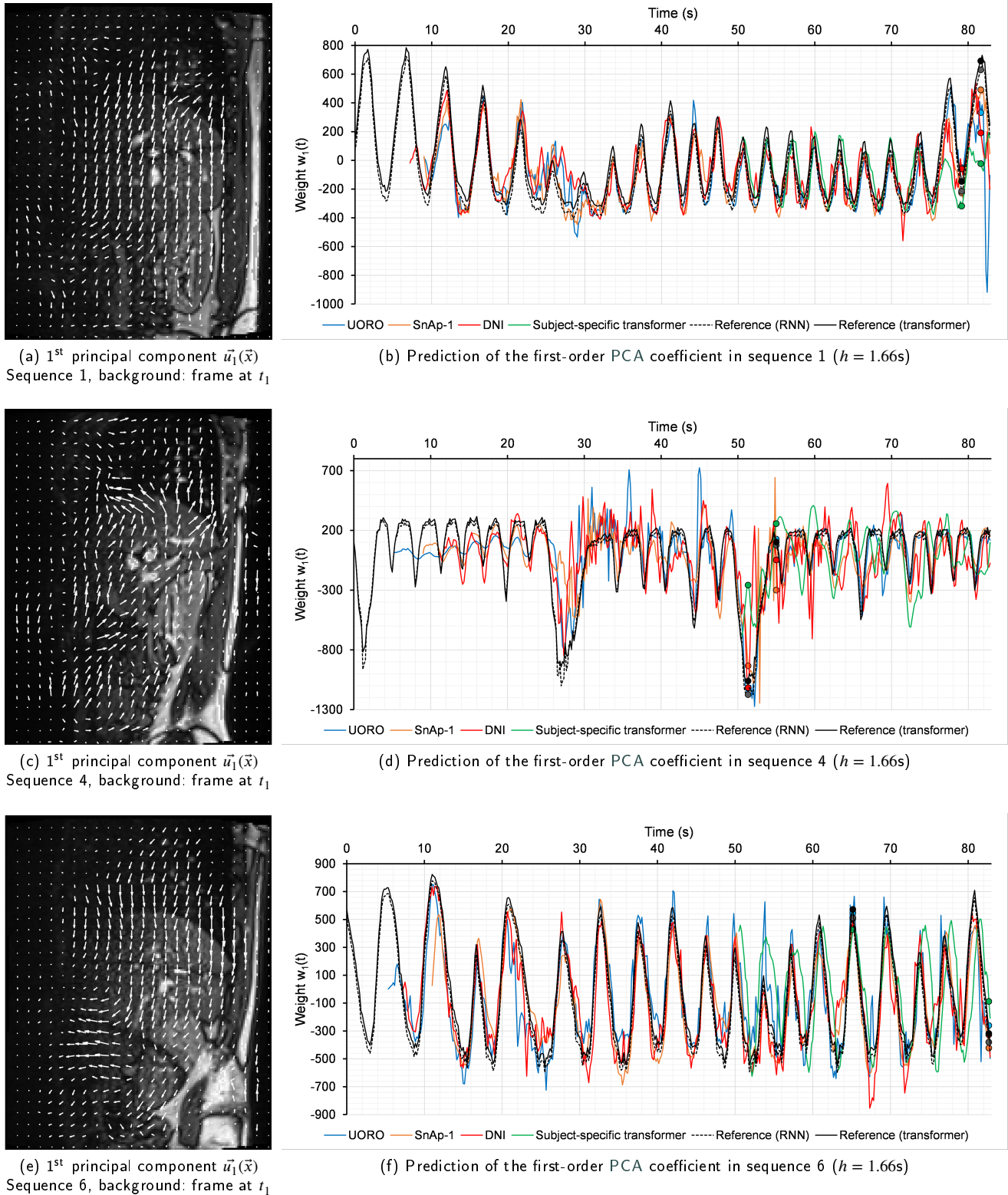


**Figure 9:** First-order principal component and corresponding time-dependent PCA weights, along with their prediction with an RNN trained with UORO, SnAp-1, and DNI and a subject-specific transformer at  $h = 1.66s$ , for sequences 1, 4, and 6 of the OvGU dataset. The principal DVFs plotted here were estimated from the first  $t_{M_{train}} = 50.4s$  of the sequence; this is the transformer setting, corresponding to the black solid lines on the plots on the right side, as opposed to the RNN setting ( $t_{M_{train}} = 28.3s$ , black dotted lines). Hyperparameters, including  $n_{cp}$ , were optimized using the validation segment for each sequence individually. The round markers on the forecasting graphs correspond to the predicted images shown in Fig. 17 (both represent the same prediction runs). Same remarks as in Fig. 6 regarding principal deformation vector spacing, scaling, and visualization.

Prediction method	Test nRMSE
UORO	$0.895 \pm 0.081$
SnAp-1	<b><math>0.857 \pm 0.100</math></b>
DNI	$0.887 \pm 0.079$
RTRL	<b><math>0.859 \pm 0.098</math></b>
LMS	$0.898 \pm 0.134$
Linear regression	$0.928 \pm 0.063$
Sequence-specific transformer	$0.879 \pm 0.048$
Population transformer (training: OvGU data)	$1.171 \pm 0.084$
RNN with a frozen hidden layer	$0.977 \pm 0.019$
Latest PCA weight as prediction (persistence)	$1.458 \pm 0.010$

**Table 3**

nRMSE of the test set associated with the prediction of the first three time-dependent PCA weights (Eq. 9 with  $k_{min} = M_{cv} + 1 = 181$  and  $k_{max} = 200$ ) for each algorithm, averaged over horizons between 0.32s and 2.20s, the four ETH Zürich sequences, and  $n_{test}^{PCA}$  runs (cf. Table 11) to account for neural network stochasticity. Each table entry corresponds to the mean of the horizon-wise errors shown in Fig. 10. Hyperparameters were selected by grid search on the validation set for each sequence and horizon individually (except the population transformer for which selection was horizon-wise only), as described in Section 2.3.3. The 70% CIs using the Student t-distribution with 3 degrees of freedom are also reported. The two lowest nRMSEs are bolded for readability.

$n_{cp}$  increased from 2 to 4, and for the sequence-specific transformer when considering that error averaged over  $h$  (black dotted curves in Fig. 12). By contrast,  $n_{cp} = 3$  minimized the sequence- and horizon-averaged error for UORO, SnAp-1, RTRL, and linear regression, whereas  $n_{cp} = 4$  seemed preferable for DNI. Higher-order PCA coefficients tended to be noisier and more challenging to forecast. However, they also carried additional information regarding minor deformation modes and exhibited mild synchronization with lower-order weights, potentially helping predict the latter. Algorithms with stronger predictive capabilities, such as SnAp-1 and RTRL, were better able to exploit these higher-order modes, which partly explains why higher values of  $n_{cp}$  benefited them.

Predictions at low response times were generally more accurate as  $n_{cp}$  increased. Indeed, regarding UORO, the sequence-mean  $E_{pred}(n_{cp})$  attained its minimum at  $n_{cp} = 2$  for  $h \geq 1.88s$  and  $n_{cp} = 3$  for  $h \leq 1.57s$ . Similarly, for LMS,  $n_{cp} = 3$  and  $n_{cp} = 4$  minimized that error for  $h \geq 0.94s$  and  $h \leq 0.63s$ , respectively. At low look-ahead times, the higher-order, noisier PCA weights could still be predicted reasonably well, improving DVF estimation as they captured finer chest and liver deformation patterns. At longer horizons, however, their prediction became unreliable; hence, discarding them (i.e., using a lower value of  $n_{cp}$ ) was often preferable. In other words, the information added by increasingly noisier PCA weights was only worth considering if they could be predicted with a relatively high degree of confidence, which was more often the case when  $h$  was small.

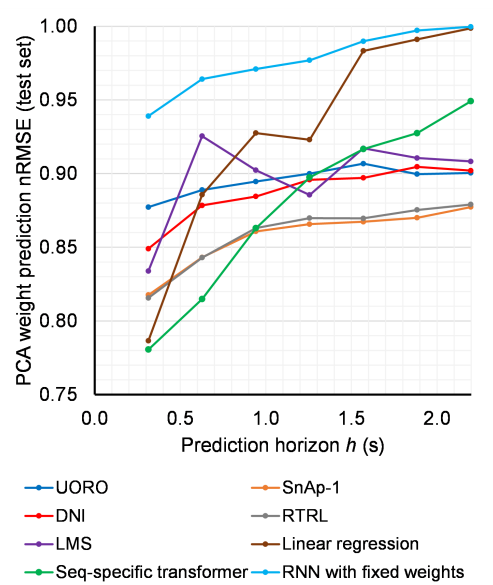


**Figure 10:** Test-set nRMSE between the reference first three time-dependent PCA weights relative to the ETH Zürich dataset and their prediction with several algorithms as a function of the horizon  $h$  (Eq. 9). Each point represents the error averaged over the four sequences and  $n_{test}^{PCA}$  runs (cf. Table 11) to account for neural network stochasticity, for a given value of  $h$ . The population transformer and the baseline using the latest incoming weight as the prediction were not represented, as their errors were relatively high. Hyperparameter tuning was performed on the validation set by grid search for each value of  $h$ .

### 3.4. Image prediction

#### 3.4.1. Quantitative evaluation

In this section, we numerically evaluate test-set image-prediction performance using pixel-intensity-based metrics, namely the Pearson correlation coefficient  $r$ , the structural similarity index measure (SSIM) [88], and the nRMSE between the ground-truth and predicted frames. Formally, the image-domain nRMSE is obtained by replacing  $\hat{w}_j$  and  $w_j^{true}$  in Eq. 9 with the predicted and ground-truth intensities, indexed by  $j \in \{1, \dots, |I|\}$ , respectively. In our implementation, the SSIM is computed over local windows and then averaged across the image. Alongside evaluation in the image space, we quantify motion-forecasting performance via the mean and maximum Euclidean endpoint errors, also referred to as geometrical errors, between the predicted and reference DVF. The latter, denoting the Lucas-Kanade optical-flow field, represents a reasonable benchmark for respiratory motion estimation [74, 75, 76], although the true underlying local tissue displacements are not directly observable. Even though mean deformation errors are reported to two decimals for consistency and comparability, differences below approximately 0.1mm should not be over-interpreted given the underlying image resolution and deformable registration uncertainty. Besides evaluating RNNs, transformers, and linear filters, we assess the performance of

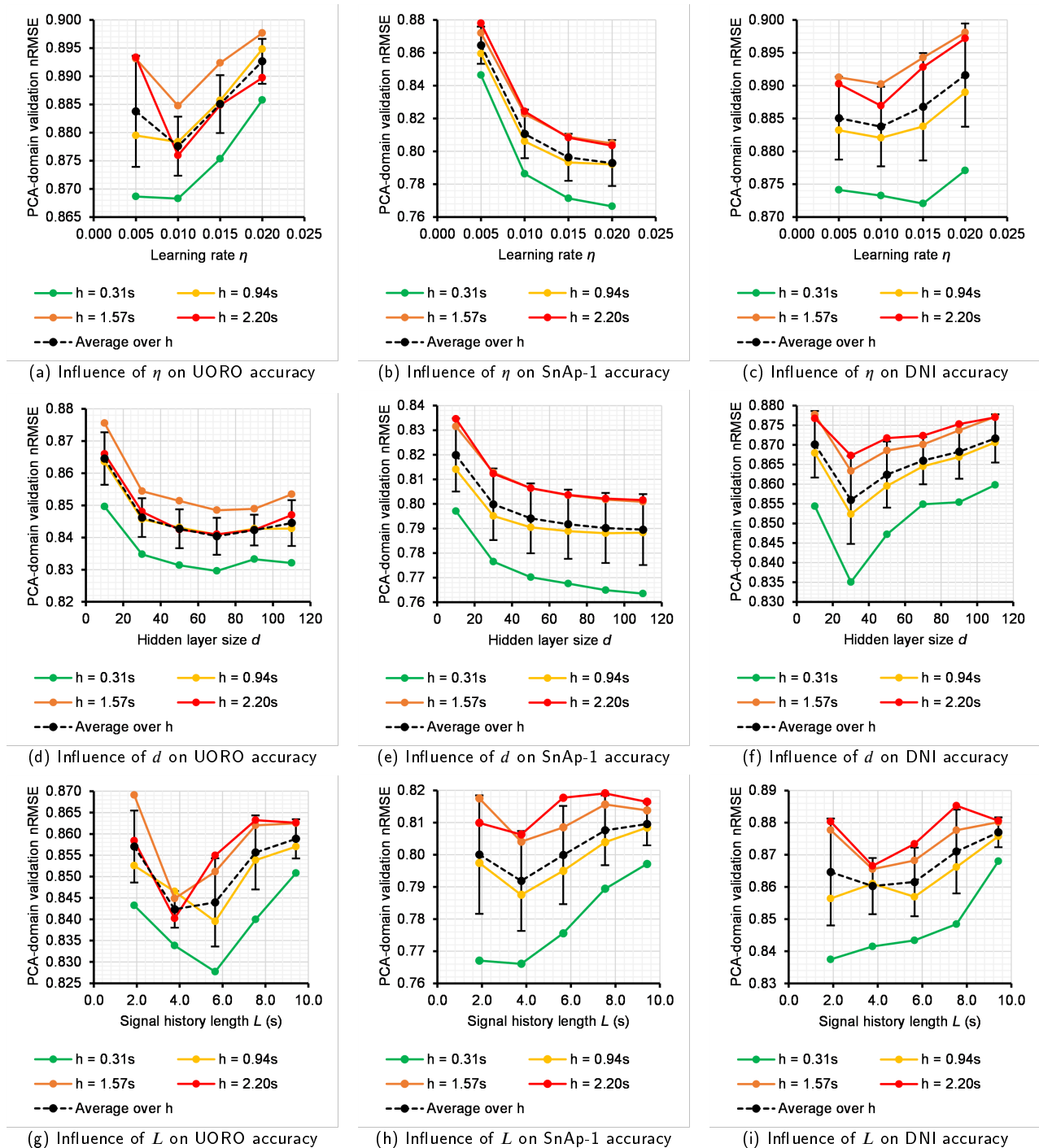


**Figure 11:** Validation nRMSE between the ground-truth first three time-dependent PCA weights relative to the ETH Zürich dataset and their prediction with an RNN trained with UORO, SnAp-1, and DNI, for various horizons  $h$  (Eq. 9). For a given hyperparameter, each colored point in the corresponding graph represents the minimum, over all combinations of the other hyperparameters in the search grid, of the nRMSE first averaged across the four sequences and  $n_{cv} = 250$  runs, at a specific value of  $h$ . The black dotted curves and associated error bars represent these error minima averaged over  $h$  between 0.31s and 2.20s and their standard deviation over this range, respectively.

two baseline naive predictors: a PCA-score-domain persistence model and an image-domain persistence model, using the latest frame and PCA weight at time  $t_k$  as the predicted frame and weight at  $t_{k+h}$ , respectively. Finally, we provide

the accuracy of an "oracle" that knows the reference optical-flow field and estimates the frame at  $t_{k+h}$  as the initial frame at  $t_1$  warped by that field. For the OvGU sequences, evaluation was performed both on the entire image and within the manually defined higher-contrast ROI.

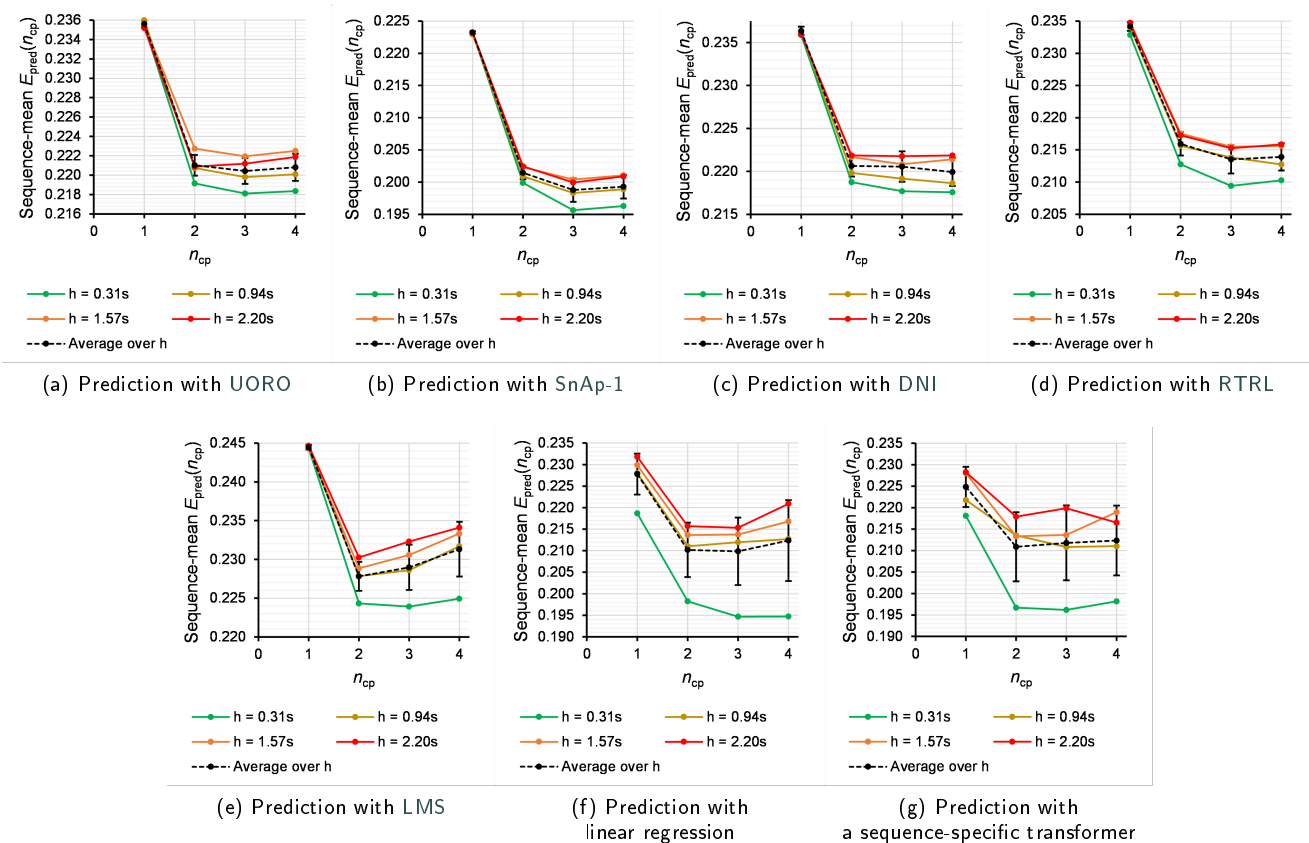


**Figure 12:** Registration error on the validation set,  $E_{pred}(n_{cp})$ , computed using the DVF predicted with  $n_{cp}$  principal components, averaged over the four sequences of the ETH Zürich dataset, as a function of  $n_{cp}$  for all sequence-specific algorithms and several horizon values  $h$  (Eq. 13). Hyperparameters were optimized by grid search for each sequence and value of  $n_{cp}$  and  $h$  (Section 2.3.3). The black dashed curves and associated error bars correspond respectively to the average and standard deviation of the sequence-mean  $E_{pred}(n_{cp})$  over all the values of  $h$  between 0.31s and 2.20s.

### Overall accuracy and stability

RTRL and SnAp-1 consistently achieved either the best or second-best test-set performance, averaged over the sequences and horizons  $h \leq 2.2$ s considered, across all metrics and both datasets (including both evaluation regions for the OvGU sequences), with mean geometrical errors of  $1.4 \pm 0.1$ mm and  $2.7 \pm 0.3$ mm on the ETH Zürich (full-frame) and OvGU (ROI) data, respectively (Table 4). LMS generally ranked second or third in terms of pixel-intensity-based metrics, and, on the ETH Zürich dataset, achieved the highest  $r$  and SSIM jointly with RTRL and SnAp-1. UORO and DNI invariably ranked either just below or on par with LMS regarding the three intensity-based measures. However, the DVF errors associated with LMS were greater than or equal to those of the four online RNN algorithms. One exception was the ROI-based maximum error on the OvGU sequences, marginally lower for LMS than for UORO. Linear regression always matched or surpassed the performance of the sequence-specific transformer. Both models ranked immediately below the adaptive algorithms regarding pixel-intensity-based metrics and mean geometrical error, except on the ETH Zürich acquisitions, where they attained a slightly lower mean endpoint error than LMS.

The population transformer was invariably outperformed by all non-baseline methods (corresponding to the first seven rows after the header in Table 4), but consistently surpassed both last-value naive models, regarding all metrics and both datasets. Noticeably, the PCA-score persistence model generally achieved higher accuracy than the image-domain one. This suggests that discarding the higher-order PCA components may have a significant regularizing effect on the initial DVF and thereby reduce noise in the predicted motion. The RNN with frozen hidden-layer parameters reached a lower accuracy than RNNs trained dynamically, confirming the benefit of online training in this setting. Finally, the oracle attained the highest performance across all metrics and both datasets (e.g., full-frame SSIMs of  $0.92 \pm 0.01$  and  $0.75 \pm 0.03$  on the ETH Zürich and OvGU data, respectively). The relatively high oracle scores, which represent an upper bound on prediction accuracy intrinsic to the DIR method employed, provide evidence of the effectiveness of the proposed warping-based approach.

For all methods, the mean geometrical error was substantially higher for the ETH Zürich acquisitions than for the OvGU ones (by about 92% on average; Table 5), mainly because the latter exhibit higher noise, lower contrast, and

Dataset	Correlation coefficient $r$			nRMSE			SSIM			Mean DVF error (mm)			Max DVF error (mm)		
	ETH Zürich	OvGU	OvGU	ETH Zürich	OvGU	OvGU	ETH Zürich	OvGU	OvGU	ETH Zürich	OvGU	OvGU	ETH Zürich	OvGU	OvGU
Evaluation region	Whole image	Whole image	ROI	Whole image	Whole image	ROI	Whole image	Whole image	ROI	Whole image	Whole image	ROI	Whole image	Whole image	ROI
UORO	0.986	0.939	0.832	0.214	0.340	0.548	0.897	0.655	0.468	1.45	2.82	2.83	21.8	23.7	15.6
	$\pm 0.005$	$\pm 0.004$	$\pm 0.023$	$\pm 0.016$	$\pm 0.012$	$\pm 0.034$	$\pm 0.022$	$\pm 0.025$	$\pm 0.033$	$\pm 0.14$	$\pm 0.21$	$\pm 0.24$	$\pm 3.2$	$\pm 3.6$	$\pm 0.9$
SnAp-1	<b>0.987</b>	<b>0.942</b>	<b>0.839</b>	0.212	<b>0.333</b>	<b>0.536</b>	<b>0.899</b>	<b>0.660</b>	0.476	<b>1.41</b>	<b>2.73</b>	2.68	<b>21.3</b>	<b>22.2</b>	<b>14.8</b>
	$\pm 0.005$	$\pm 0.004$	$\pm 0.024$	$\pm 0.016$	$\pm 0.013$	$\pm 0.036$	$\pm 0.022$	$\pm 0.026$	$\pm 0.036$	$\pm 0.14$	$\pm 0.22$	$\pm 0.25$	$\pm 3.3$	$\pm 3.1$	$\pm 0.9$
DNI	0.986	0.940	0.831	0.215	0.339	0.548	0.898	0.654	0.465	1.46	2.83	2.84	21.7	23.0	15.6
	$\pm 0.006$	$\pm 0.004$	$\pm 0.023$	$\pm 0.018$	$\pm 0.012$	$\pm 0.035$	$\pm 0.023$	$\pm 0.025$	$\pm 0.034$	$\pm 0.16$	$\pm 0.21$	$\pm 0.25$	$\pm 3.2$	$\pm 3.1$	$\pm 0.9$
RTRL	<b>0.987</b>	<b>0.942</b>	0.838	<b>0.211</b>	<b>0.333</b>	<b>0.536</b>	<b>0.899</b>	<b>0.660</b>	<b>0.477</b>	<b>1.41</b>	<b>2.73</b>	<b>2.66</b>	<b>21.3</b>	<b>22.5</b>	<b>14.8</b>
	$\pm 0.005$	$\pm 0.005$	$\pm 0.024$	$\pm 0.016$	$\pm 0.013$	$\pm 0.037$	$\pm 0.022$	$\pm 0.027$	$\pm 0.037$	$\pm 0.14$	$\pm 0.22$	$\pm 0.24$	$\pm 3.3$	$\pm 3.2$	$\pm 0.9$
LMS	<b>0.987</b>	0.940	0.833	0.214	0.337	0.544	<b>0.899</b>	0.656	0.470	1.48	2.83	2.85	22.0	24.0	15.4
	$\pm 0.005$	$\pm 0.006$	$\pm 0.026$	$\pm 0.018$	$\pm 0.015$	$\pm 0.039$	$\pm 0.021$	$\pm 0.027$	$\pm 0.037$	$\pm 0.19$	$\pm 0.23$	$\pm 0.29$	$\pm 3.4$	$\pm 4.0$	$\pm 0.9$
Linear regression	0.985	0.938	0.822	0.218	0.342	0.560	0.894	0.651	0.453	1.47	2.86	3.05	21.7	23.2	15.3
	$\pm 0.006$	$\pm 0.004$	$\pm 0.023$	$\pm 0.017$	$\pm 0.010$	$\pm 0.034$	$\pm 0.025$	$\pm 0.026$	$\pm 0.034$	$\pm 0.13$	$\pm 0.20$	$\pm 0.29$	$\pm 2.8$	$\pm 3.7$	$\pm 0.9$
Seq-specific transformer	0.985	0.936	0.815	0.218	0.346	0.567	0.894	0.649	0.448	1.46	2.94	3.17	22.9	23.1	15.7
	$\pm 0.007$	$\pm 0.004$	$\pm 0.025$	$\pm 0.018$	$\pm 0.012$	$\pm 0.035$	$\pm 0.026$	$\pm 0.025$	$\pm 0.032$	$\pm 0.14$	$\pm 0.23$	$\pm 0.32$	$\pm 2.7$	$\pm 3.2$	$\pm 0.9$
Population transformer	0.978	0.922	0.769	0.255	0.382	0.635	0.874	0.620	0.386	1.95	3.37	3.98	27.2	26.8	18.1
	$\pm 0.008$	$\pm 0.006$	$\pm 0.026$	$\pm 0.026$	$\pm 0.013$	$\pm 0.034$	$\pm 0.023$	$\pm 0.022$	$\pm 0.027$	$\pm 0.25$	$\pm 0.22$	$\pm 0.39$	$\pm 3.2$	$\pm 3.8$	$\pm 0.7$
RNN with fixed weights	0.981	0.935	0.806	0.234	0.350	0.585	0.887	0.646	0.423	1.61	2.92	3.09	23.3	24.4	15.5
	$\pm 0.010$	$\pm 0.004$	$\pm 0.026$	$\pm 0.024$	$\pm 0.011$	$\pm 0.037$	$\pm 0.030$	$\pm 0.024$	$\pm 0.039$	$\pm 0.16$	$\pm 0.22$	$\pm 0.28$	$\pm 3.0$	$\pm 4.1$	$\pm 0.8$
Latest PCA score	0.972	0.914	0.748	0.276	0.399	0.662	0.860	0.611	0.369	2.13	3.63	4.41	27.9	29.2	18.9
	$\pm 0.014$	$\pm 0.005$	$\pm 0.030$	$\pm 0.034$	$\pm 0.011$	$\pm 0.036$	$\pm 0.028$	$\pm 0.023$	$\pm 0.029$	$\pm 0.26$	$\pm 0.28$	$\pm 0.49$	$\pm 3.2$	$\pm 5.2$	$\pm 0.9$
Latest image	0.965	0.910	0.733	0.318	0.408	0.698	0.848	0.609	0.385	n/a	n/a	n/a	n/a	n/a	n/a
	$\pm 0.015$	$\pm 0.006$	$\pm 0.031$	$\pm 0.031$	$\pm 0.016$	$\pm 0.043$	$\pm 0.028$	$\pm 0.029$	$\pm 0.034$						
Reference DVF (oracle)	0.991	0.966	0.911	0.159	0.253	0.397	0.918	0.753	0.632	n/a	n/a	n/a	n/a	n/a	n/a
	$\pm 0.002$	$\pm 0.004$	$\pm 0.018$	$\pm 0.013$	$\pm 0.014$	$\pm 0.040$	$\pm 0.012$	$\pm 0.025$	$\pm 0.035$						

**Table 4**

Test-set video-prediction performance for each algorithm. Each value represents the average of a measure over all MRI sequences in either the ETH Zürich or OvGU dataset, the horizons considered ( $h \leq 2.2s$ ), and  $n_{\text{test}}$  evaluation runs to account for neural network stochasticity (Section 2.4). Hyperparameters, including  $n_{cp}$ , were optimized for each sequence and horizon individually (except the population transformer for which selection was horizon-wise only), as described in Sections 2.3.3 and 2.5. We report the 70% CIs associated with each metric, using the Student's t-distribution with  $N - 1$  degrees of freedom, where  $N$  is the number of sequences in each dataset. The rows "latest PCA score" and "latest image" correspond to using the PCA score  $w_j(t_k)$  and frame at time  $t_k$  as direct estimates of their future values at time  $t_{k+h}$ . The last row ("reference DVF - oracle") corresponds to estimating the frame at time  $t_{k+h}$  as the initial frame at  $t = t_1$  warped by the Lucas-Kanade optical flow between  $t_1$  and  $t_{k+h}$ . For each metric, all best-performing non-oracle methods are bolded (ties included).

stronger motion variability. For the OvGU dataset, the same mean endpoint error was slightly higher when computed in the ROIs than over the entire frames (by 3.8% on average). SnAp-1 and RTRL were the only exceptions: their mean DVF errors on the ROI were slightly lower than their full-frame ones, although the corresponding CIs overlapped (e.g.,  $2.73 \pm 0.22\text{mm}$  vs.  $2.68 \pm 0.25\text{mm}$  for SnAp-1). This suggests that both methods could robustly forecast the more structured but higher-amplitude ROI motion, consistent with their overall top performance among the algorithms considered (Table 4). The maximum DVF error dropped when restricting evaluation from the whole image to the ROI on the OvGU data, by about 34% on average for non-baseline methods (e.g., from  $22.2 \pm 3.1\text{mm}$  to  $14.8 \pm 0.9\text{mm}$  for SnAp-1). This reflects that motion prediction was more challenging in the lower-contrast, noisier peripheral areas, where DIR was relatively unreliable. Full-frame intensity-based accuracy was also higher on the ETH Zürich sequences than on the OvGU ones, with an average 27.2% SSIM decrease across RNNs trained online, transformers, and linear filters.

For instance, the full-frame SSIM of SnAp-1 decreased from  $0.90 \pm 0.02$  to  $0.66 \pm 0.03$  when swapping datasets. Likewise, intensity-based performance on the OvGU acquisitions was consistently lower when measured in the ROI rather than the whole image, with a mean 30.1% SSIM decrease for these non-baseline methods (e.g., the ROI-based SSIM was  $0.48 \pm 0.04$  for SnAp-1). This contrasts with the high intra-dataset stability observed for the mean geometrical error: even when deformations were predicted reasonably well in the ROI, image warping could still produce blur or misalignment in this high-contrast area, which degraded the SSIM. Notably, SnAp-1 and RTRL exhibited the greatest stability for the latter metric across datasets and image regions, and the highest intra-dataset stability regarding the mean DVF error.

Due to the relatively small number of sequences, the 70% CIs often overlapped between methods evaluated on the same dataset and in the same image region (Table 5). However, uncertainties for ROI-based metrics were consistently larger, reflecting higher motion variability and structural changes in that region, except for the maximum geometrical

		Cross-dataset stability ETH Zürich → OvGU (entire image)		Intra-dataset stability entire image → ROI (OvGU data)	
		Test SSIM decrease (%)	Mean test DVF error increase (%)	Test SSIM decrease (%)	Mean test DVF error increase (%)
<b>Prediction methods</b>	UORO	26.9	94.7	28.6	0.2
	SnAp-1	<b>26.6</b>	94.2	<b>27.8</b>	<b>-1.8</b>
	DNI	27.1	93.4	28.9	0.6
	RTRL	<b>26.5</b>	94.1	<b>27.7</b>	<b>-2.3</b>
	LMS	27.0	<b>91.2</b>	28.4	0.8
	Linear regression	27.2	94.6	30.4	6.5
	Sequence-specific transformer	27.5	101.2	30.9	8.1
	Population transformer	29.1	72.8	37.8	18.1
<b>Baselines</b>	RNN with a frozen hidden layer	27.2	81.4	34.5	6.0
	Latest PCA weight used as prediction	29.0	70.3	39.7	21.5
	Latest image used as prediction	28.2	n/a	36.7	n/a
<b>Oracle</b>	Warping with Lucas–Kanade optical flow	18.0	n/a	16.1	n/a
<b>Average for non-baseline and non-oracle methods</b>		27.2	92.0	30.1	3.8

**Table 5**

Cross-dataset and intra-dataset stability for each prediction method, measured as the test-set performance drop when moving from entire-image evaluations on the ETH Zürich sequences to those on the OvGU data, and from entire-image to ROI-based predictions on the OvGU data, respectively. The metric values for calculating those relative differences, provided in Table 4, are the SSIM and mean DVF error averaged over the sequences in each dataset, the horizons  $h \leq 2.2s$ , and  $n_{\text{test}}$  runs. A minus sign in the last column indicates an error decrease. In each column, the two most stable prediction methods are bolded for readability, except for cross-dataset stability evaluation with the DVF error. In the latter case, only the second most robust method is highlighted, since the population transformer—though most stable—produced much higher errors than the other algorithms.

error, due to higher noise in peripheral areas. When comparing the same algorithm across datasets or image regions, CIs generally did not overlap, except for the mean DVF error across datasets and the maximum DVF error across evaluation regions, respectively. These patterns support the robustness analysis outlined above.

### Statistical analysis of accuracy

To complement the discussion above, we conducted two-sided Wilcoxon signed rank tests and computed Cohen’s  $d$  values using the OvGU acquisitions<sup>8</sup>(here,  $d$  does not refer to the RNN hidden-layer dimension). We considered two complementary perspectives, using horizon-averaged full-frame SSIMs and mean ROI deformation errors for global intensity-based and local geometry-based evaluation, respectively. Statistical evaluation of RNNs trained online and linear filters may lack sensitivity due to the small number of sequences ( $N = 8$ ). This is reflected, for instance, by the low-to-medium  $p$ -values but high  $d$ -values (indicating practical, meaningful differences) when comparing UORO with SnAp-1 ( $p = 0.109$ ,  $d = 0.85$ ) and RTRL with DNI ( $p = 0.109$ ,  $d = 0.80$ ) using the mean DVF error in the ROI (Table 6). Noticeably, only the local deformation-based analysis produced marginally significant comparisons ( $p \leq 0.08$ ) and large effect sizes ( $|d| \geq 0.8$ ) for adaptive filters and linear regression. The high values of  $d$  for RTRL and SnAp-1 compared with UORO and DNI (four pairwise comparisons in total) indicate a practically robust performance gain that is consistent across sequences. This was observed even though error differences between algorithms across those two groups were generally modest; the highest average

gap (0.18mm) was between DNI and RTRL (Table 4). By contrast, mean ROI deformation-error comparisons between online-trained RNNs, on the one hand, and linear regression, on the other hand, were characterized by medium-to-large effect sizes (with  $|d|$  between 0.45 and 0.85) and low-to-moderate  $p$ -values (below 0.195), pointing to slightly less robust trends despite larger raw error differences (up to 0.39mm between linear regression and RTRL). The lower mean DVF errors in the ROI for RTRL and SnAp-1 compared with LMS were marginally statistically significant ( $p = 0.055$ ), with moderate effect sizes ( $d \approx 0.75$ ).

Statistical analysis confirmed the generally lower performance of transformers relative to the non-baseline algorithms (e.g.  $p = 0.008$  and  $d \geq 1.23$  for all pairwise comparisons with the cross-subject model). Nonetheless, there were exceptions for the subject-specific transformer: its comparisons with linear regression were not statistically significant for either metric ( $p \geq 0.461$ ), and those with both DNI and LMS yielded only moderate  $p$ -values and effect sizes for the SSIM ( $p \geq 0.195$ ,  $d = 0.49$ ). Finally, the relatively lower performance of the RNN with a frozen hidden layer relative to RNNs trained online, and that of the persistence models relative to the other algorithms, was statistically significant in all cases, except for the comparisons with the population transformer, which produced low-to-moderate  $p$ -values ( $p \leq 0.250$ ).

<sup>8</sup>Such statistical analysis was not performed with the ETH Zürich data, as  $N = 4$  sequences would yield under-powered tests (the smallest Wilcoxon signed-rank  $p$ -value attainable would be 0.0625)

Prediction method	Evaluation metric and region	SnAp-1		DNI		RTRL		LMS		Linear regression		Subj-specific transformer		Population transformer		RNN with fixed weights		Latest PCA score		Latest image	
		<i>p</i> -val.	<i>d</i>	<i>p</i> -val.	<i>d</i>	<i>p</i> -val.	<i>d</i>	<i>p</i> -val.	<i>d</i>	<i>p</i> -val.	<i>d</i>	<i>p</i> -val.	<i>d</i>	<i>p</i> -val.	<i>d</i>	<i>p</i> -val.	<i>d</i>	<i>p</i> -val.	<i>d</i>	<i>p</i> -val.	<i>d</i>
UORO	SSIM, full frame	0.148	-0.52	0.945	0.16 <sup>†</sup>	0.109	-0.65	0.844	-0.08 <sup>†</sup>	0.312	0.30	<b>0.078</b>	<b>1.03</b>	<b>0.008</b>	<b>1.74</b>	0.008	1.68	0.008	3.00	0.016	1.75
	DVF error, ROI	0.109	<b>0.85</b>	0.945	-0.07 <sup>†</sup>	<b>0.023</b>	<b>1.10</b>	0.641	-0.08 <sup>†</sup>	0.148	-0.60	<b>0.016</b>	<b>-1.29</b>	<b>0.008</b>	<b>-1.75</b>	0.008	-1.58	0.008	-1.85	-	-
SnAp-1	SSIM, full frame			0.109	0.63	0.547	-0.35	0.383	0.38	0.109	0.47	<b>0.039</b>	<b>0.95</b>	<b>0.008</b>	<b>1.43</b>	0.008	2.25	0.008	2.41	0.016	1.67
	DVF error, ROI	-	-	<b>0.039</b>	<b>-0.83</b>	0.742	0.20	<b>0.055</b>	-0.74	<b>0.078</b>	-0.76	<b>0.008</b>	<b>-1.29</b>	<b>0.008</b>	<b>-1.60</b>	0.008	-1.76	0.008	-1.78	-	-
DNI	SSIM, full frame					0.312	-0.72	0.461	-0.30	0.312	0.18	0.250	0.49	<b>0.008</b>	<b>1.43</b>	0.008	1.11	0.008	2.34	0.016	1.49
	DVF error, ROI	-	-	-	-	0.109	<b>0.80</b>	0.844	-0.04 <sup>†</sup>	0.195	-0.45	<b>0.016</b>	<b>-0.98</b>	<b>0.008</b>	<b>-1.58</b>	0.016	-1.30	0.008	-1.62	-	-
RTRL	SSIM, full frame							0.250	0.47	0.109	0.53	<b>0.008</b>	<b>1.05</b>	<b>0.008</b>	<b>1.47</b>	0.008	2.15	0.008	2.45	0.016	1.73
	DVF error, ROI	-	-	-	-	-	-	<b>0.055</b>	-0.75	<b>0.055</b>	<b>-0.85</b>	<b>0.008</b>	<b>-1.38</b>	<b>0.008</b>	<b>-1.65</b>	0.008	-1.84	0.008	-1.86	-	-
LMS	SSIM, full frame									0.250	0.23	0.195	0.49	<b>0.008</b>	<b>1.23</b>	0.055	0.94	0.008	1.85	0.016	1.35
	DVF error, ROI	-	-	-	-	-	-	-	-	0.383	-0.36	<b>0.055</b>	-0.78	<b>0.008</b>	<b>-1.35</b>	0.078	-0.84	0.008	-1.51	-	-
Linear regression	SSIM, full frame										0.742	0.20	<b>0.008</b>	<b>1.62</b>	0.461	0.32	0.008	2.86	0.008	2.07	
	DVF error, ROI	-	-	-	-	-	-	-	-	-	0.461	-0.38	<b>0.008</b>	<b>-1.76</b>	0.945	-0.14	0.008	-2.10	-	-	
Subj-specific transformer	SSIM, full frame												<b>0.008</b>	<b>1.59</b>	0.547	0.36	0.008	2.81	0.016	1.54	
	DVF error, ROI	-	-	-	-	-	-	-	-	-	-	-	<b>0.008</b>	<b>-1.59</b>	0.461	0.37	0.008	-1.84	-	-	
Population transformer	SSIM, full frame														0.008	-1.13	0.078	0.76	0.250	0.47	
	DVF error, ROI	-	-	-	-	-	-	-	-	-	-	-	-	-	0.008	1.39	0.109	-0.74	-	-	
RNN with fixed weights	SSIM, full frame																0.008	2.24	0.016	1.27	
	DVF error, ROI	-	-	-	-	-	-	-	-	-	-	-	-	-	-	-	0.008	-1.64	-	-	
Latest PCA score	SSIM, full frame																			0.742	0.12
	DVF error, ROI	-	-	-	-	-	-	-	-	-	-	-	-	-	-	-	-	-	-	-	-

**Table 6**

Statistical tests associated with image prediction on the OvGU dataset. Each value corresponds to the (two-tailed)  $p$ -value from the Wilcoxon signed-rank test or Cohen's  $d$  for each pair of methods, computed from the differences between sequence-level full-frame SSIM or mean DVF error in the ROI (averaged over the test set, all horizons  $h \leq 2.2s$ , and  $n_{\text{test}}$  runs) between methods A and B. A positive Cohen's  $d$  for a given metric indicates that method A (rows) tends to yield a higher metric value than method B (columns). A dagger symbol was added near the  $d$ -value when the median of the corresponding sequence-level metric difference over all videos had a different sign than the mean difference, indicating that the direction of  $d$  may not be meaningful in such instances.  $p$ -values lower than 0.08 and values of  $d$  greater than 0.8, reflecting (at least marginal) statistical significance and large effect sizes, respectively, were bolded for non-baseline methods for readability. This  $p$ -value threshold, set higher than 0.05, helps highlight trends that may be under-powered rather than absent, given the small dataset size ( $N = 8$  sequences).

### Performance evolution with the horizon

Across all algorithms, accuracy metrics ( $r$  and SSIM) tended to decrease with the horizon  $h$ , while error metrics (image-domain nRMSE and DVF errors) generally increased with  $h$  (Figs. 13–14 and Fig. 19 in Appendix E). Nonetheless, performance evolution with  $h$  exhibited instabilities, due to small dataset sizes ( $N = 8$  sequences maximum) and per-horizon hyperparameter tuning. That phenomenon was most pronounced for the full-frame maximum DVF error on the OvGU acquisitions, possibly due to less accurate deformable registration near the low-contrast noise-dominated image borders (Fig. 19).

SnAp-1 and RTRL, the strongest predictors for intermediate-to-high values of  $h$ , exhibited nearly identical performance regardless of  $h$ . UORO, DNI, and LMS formed a second group with relatively close performance on the OvGU data and similar DVF errors and nRMSEs on the ETH Zürich data; the gap between both groups remained small and largely stable as  $h$  increased. This pattern mirrors the behavior observed for PCA-weight forecasting (Fig. 10) and aligns with the medium-to-large effect sizes reported in Table 6. The sequence-specific transformer achieved competitive accuracy at low horizons, performing similarly to RTRL and SnAp-1 for  $h \leq 0.63s$  on the ETH Zürich data (e.g., mean DVF error below 1.37mm) and  $h \leq 0.50s$  on the OvGU sequences (e.g., mean ROI deformation error below 2.65mm). However, its accuracy degraded rapidly as  $h$  increased, in contrast

with online-trained RNNs. The population transformer stayed the least accurate non-baseline method across all horizons, except at  $h = 0.17s$  on the OvGU data (e.g., ROI-based mean DVF error of  $2.53 \pm 0.17\text{mm}^9$ ), where it outperformed UORO and DNI regarding both evaluation regions and most metrics.

Regarding low horizons, the image-domain persistence model produced the best intensity-based metrics (excluding the oracle) on the OvGU data in the ROI at  $h = 0.17s$  and in the full image at  $h \leq 0.33s$ , respectively; its ROI-based SSIM was also the highest at  $h = 0.33s$ . By contrast, it consistently underperformed the non-baseline algorithms on the ETH Zürich data, except for the cross-subject transformer, whose  $r$  and SSIM were lower at  $h = 0.31s$ . This discrepancy likely reflects differences in acquisition properties: the ETH Zürich sequences feature lower noise, higher contrast, and less motion variability, which makes prediction easier and reduces the benefit of simply copying the last frame at short response times. Conversely, matching local noise patterns in the OvGU frames can inflate performance metrics at low look-ahead times. For both datasets, linear regression performed strongly at small horizons, reaching the lowest mean and maximum DVF errors at  $h = 0.31s$  on the ETH Zürich sequences ( $1.30 \pm 0.18\text{mm}$  mean DVF error) and for all  $h \leq 0.50s$  on the OvGU data in both evaluation

<sup>9</sup>We report here the 70% CIs computed from the Student's  $t$ -distribution with  $N - 1$  degrees of freedom, where  $N$  is the number of sequences in each dataset. Horizon-wise CIs were not plotted in Figs. 13, 14, and 19 to avoid visual clutter and better emphasize trends with  $h$ .

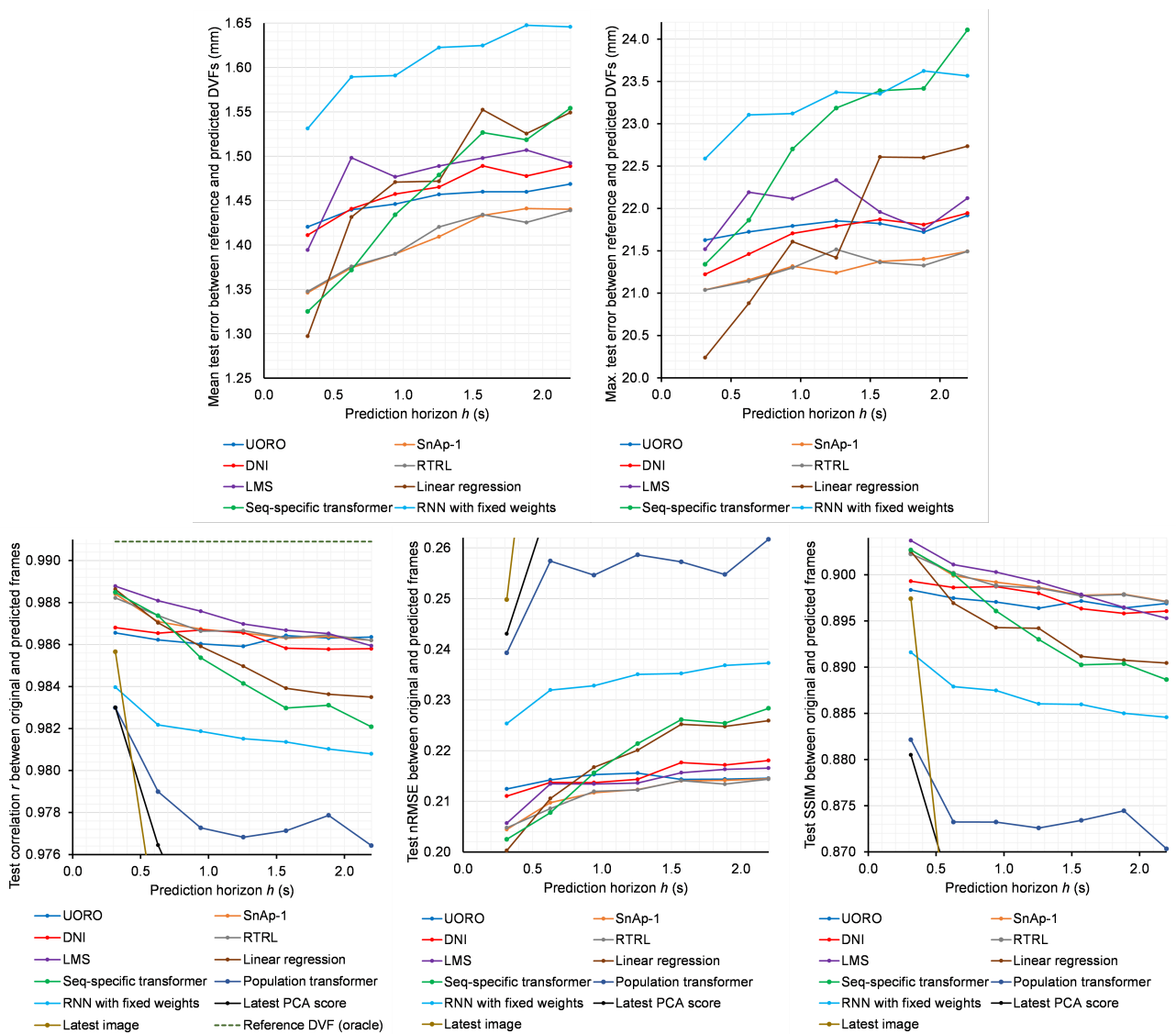


**Figure 13:** Test-set frame-forecasting performance for each algorithm as a function of the horizon  $h$ , for the ETH Zürich dataset. Each point represents the average of a given metric over the four image sequences and  $n_{\text{test}}$  runs (Section 2.4). Hyperparameters, including  $n_{cp}$ , were optimized for each value of  $h$  (and for each sequence, except the population transformer), as described in Sections 2.3.3 and 2.5. Baseline and oracle definitions are identical to those in Table 4. The mean of each curve (i.e., the performance averaged over  $h$  for each method) is reported in the “ETH Zürich” columns of that table. To improve readability, curves for algorithms with relatively poor accuracy (DVF errors for the population transformer and the naive PCA-weight predictor) and for oracle metrics far below or above the others (nRMSE and SSIM, respectively) were omitted.

regions (e.g.,  $2.43 \pm 0.23\text{mm}$  mean ROI-based DVF error at  $h = 0.33\text{s}$ ). The lower crossover point where it began to outperform image copying regarding the ROI-based  $r$  and nRMSE on the OvGU data ( $h = 0.33\text{s}$  instead of  $h = 0.50\text{s}$  for full-frame evaluation) possibly reflects lower noise and more structured motion in that area, which facilitate DIR and short-term motion forecasting. However, even for the smallest horizons, the oracle method almost systematically outperformed the strongest predictors, including linear regression and the last-image model.

Regarding medium-to-long horizons, SnAp-1 and RTRL were more accurate than linear regression on the OvGU dataset when  $h \geq 0.66\text{s}$ , except for the maximum DVF error.

Both RNN algorithms attained the lowest value among all algorithms for the latter error only when  $h \geq 1.0\text{s}$  in the ROI and for most horizons  $h \geq 0.50\text{s}$  in the full frame, with a few exceptions due to whole-image evaluation instability. On the ETH Zürich data, they also generally outperformed the other algorithms, including linear regression, regarding geometrical errors and nRMSEs for  $h \geq 0.94\text{s}$ . Notably, LMS reached the highest  $r$  and SSIM (among non-oracle methods) for  $h \leq 1.88\text{s}$  and  $h \leq 1.57\text{s}$ , respectively. Performance degradation for SnAp-1 and RTRL beyond  $h = 0.66\text{s}$  was less pronounced on the OvGU dataset. For instance, the ROI-based DVF error of SnAp-1 rose from 2.42

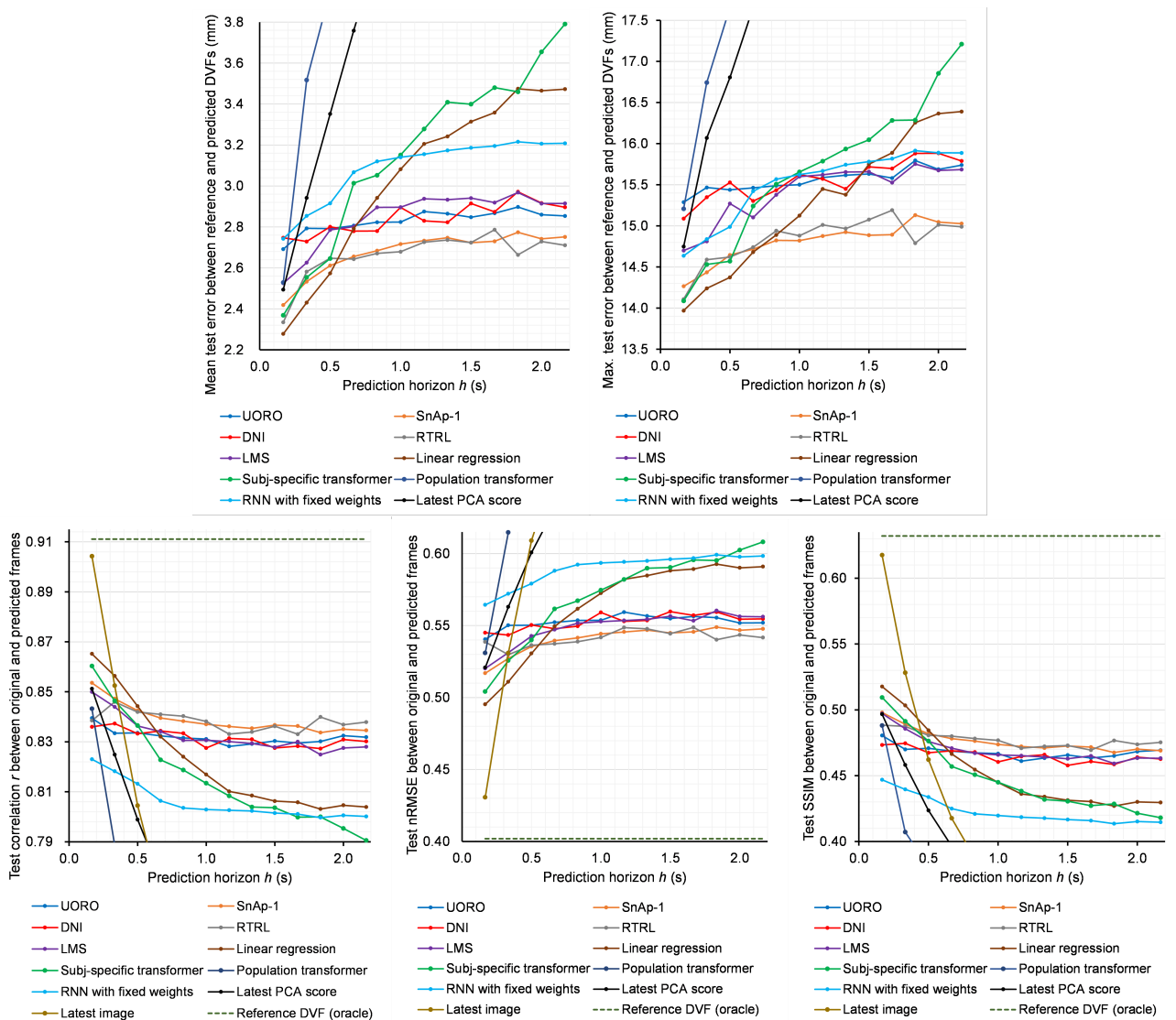


**Figure 14:** Test-set frame-forecasting performance for each algorithm as a function of the horizon  $h$ , for the OvGU dataset, computed in the ROI. Each point represents the average of a given metric over the eight image sequences and  $n_{\text{test}}$  runs. Hyperparameters, including  $n_{cp}$ , were optimized for each value of  $h$  using grid search on the validation set. The mean of each curve (i.e., the performance averaged over  $h$  for each method) is reported in the “OvGU (ROI)” columns of Table 4.

$\pm 0.19\text{mm}$  at  $h = 0.17\text{s}$  to  $2.66 \pm 0.25\text{mm}$  at  $h = 0.66\text{s}$  and reached only  $2.75 \pm 0.26\text{mm}$  at  $h = 2.17\text{s}$ .

The relative SSIM decrease and relative increase in mean DVF error between  $h = 0.3\text{s}$  and  $h = 2.2\text{s}$  were lower for online-trained RNNs than for all other non-baseline predictors (Table 12 in Appendix E). LMS consistently ranked immediately below RNNs among non-baseline methods regarding stability across horizons. On the OvGU dataset, stability decreased from whole-image to ROI evaluation, as the relative metric variations between the smallest and largest horizons generally increased by a factor of approximately 2–3. This reflects the presence of static peripheral background regions in the full frames and the more complex, high-amplitude deformations of the diaphragm, liver, and surrounding structures characterizing the ROI. By contrast, full-frame stability with  $h$  compared across datasets showed no

consistent trend: on average over non-baseline algorithms, the relative SSIM decrease between  $h = 0.3\text{s}$  and  $h = 2.2\text{s}$  was roughly three times larger for the ETH Zürich acquisitions than for the OvGU ones, while the relative DVF-error increase remained similar.

### 3.4.2. Qualitative evaluation

#### Visual assessment on the ETH Zürich dataset

In the predicted ETH Zürich frames, the breathing-induced organ deformations and the SI motion of the diaphragm and vessels were visually reproduced reasonably well, though not always with perfect accuracy. In sequence 1, the diaphragm appeared more elevated in the predictions from RTRL and the population transformer at  $t = 60.9\text{s}$ , corresponding to the EI phase, than in the original image, for both  $h = 0.31\text{s}$  and  $h = 2.20\text{s}$  (Fig. 15). Conversely,

its predicted boundary at  $t = 58.4\text{s}$ —the immediately preceding end-expiration (EE) phase—was slightly inferior to the ground-truth position for both models at  $h = 2.20\text{s}$ , and also for the transformer at  $h = 0.31\text{s}$ . This was likely due to predictions of  $w_2(t)$  exceeding the reference value at  $t = 58.4\text{s}$  (Figs. 8c-8d). Indeed, given the general downwards direction of the second-order component (Fig. 6e), a higher negative estimated value for  $w_2(t)$  produces less upwards displacement (Eq. 10). Likewise, we conjecture that the larger discrepancy at the EI phase primarily reflected over-predicted values of  $w_3(t)$  (Figs. 8e-8f), whose associated principal-component vectors locally pointed in the superior direction (Fig. 6f), although interactions with the second-order component also influenced the final displacement.

In sequence 1, at  $t = 58.4\text{s}$  (EE), high instantaneous intensity errors were concentrated near the superior right-ventricle wall, whereas the corresponding deformation errors were more homogeneous across that ventricle and the pancreas. At  $t = 60.9\text{s}$  (EI), both error types were more pronounced, with higher frame-wise maxima, particularly in the small lung region posterior to the heart, due to out-of-plane motion. Across the test set, mean intensity errors in sequence 1 were most prominent around that posterior air pocket and were moderate along sharp anatomical boundaries, including the diaphragm and right-ventricle top (cf. Fig. 16b for errors obtained with SnAp-1). Although instantaneous DVF errors broadly matched the intensity-error patterns in some regions for RTRL and the population transformer (e.g., higher values in lumbar and sternal areas), they were more spatially diffuse, reflecting the locally uniform nature of the displacement fields (Figs. 2, 6a-6b). Noticeably, deformation-forecasting inaccuracies in low-contrast areas did not necessarily yield large intensity errors. Conversely, local intensity mismatches may be attributed to sharp contrast between adjacent organs—such as at the diaphragm boundary—rather than acute and localized motion error.

These observations—namely the spatial diffuseness of DVF errors and their only moderate correspondence with intensity errors—were also evident in mean test-set error maps for SnAp-1 across all four sequences (Fig. 16). In sequences 2 and 4, moderate-to-high intensity errors near the central pulmonary vessels did not correlate with substantial geometrical errors. Noticeably, mean intensity errors were relatively strong near the diaphragm region and the intrahepatic vessels in sequence 2 (Fig. 16e). This reflects the fast SI motion of the liver relative to the sampling frequency, as evidenced by blurring near the diaphragm in the mean image. Specifically, in this acquisition, deformation errors were concentrated near the posterior part of the liver (Fig. 16f), where mean intensities appeared most blurred and motion amplitude was high. Across sequences, noise and temporal variations in local tissue texture additionally produced moderate and spatially diffuse intensity errors within tissue and moving organs, particularly visible in sequences 3 and 4. Lastly, all sequences exhibited moderate-to-large errors near the skin surface, subcutaneous fat, and osseous

structures (the rib cage and spine), due to strong tissue–bone–air contrast and out-of-plane motion.

### Visual assessment on the OvGU dataset

In the predicted OvGU frames, the overall positions and texture of anatomical structures, including the vessels, appeared generally correct despite the substantial noise in the original acquisitions and the relatively long horizon used for qualitative assessment ( $h = 1.66\text{s}$ ; Fig. 17). In sequence 1, the liver location in the predicted image at  $t = 81.7\text{s}$  (EI) seemed relatively accurate for SnAp-1 but appeared gradually more elevated in the predictions from UORO, DNI, and the population transformer, for which the mismatch with the ground truth was the strongest. This trend is consistent with the decreasing positive value of the predicted first-order PCA weight for these algorithms, in the same order (corresponding to an increasing error; Fig. 9b), at a time point where breathing irregularities in amplitude and phase were relatively strong, combined with the predominantly inferior direction of the first principal component (Fig. 9a). At the immediately preceding EE phase ( $t = 79.2\text{s}$ ), the transformer prediction placed the liver slightly higher than in the original frames, again in line with an underestimation of the negative first-order PCA-weight value. Likewise, in sequence 6, inaccurate PCA-coefficient prediction produced a slightly inferior liver position in the transformer estimation compared with the ground truth at  $t = 82.7\text{s}$  (EE; Fig. 9f). In sequence 4, the liver position was also challenging to forecast, especially near the deep inspiration at  $t = 51.3\text{s}$ . At that phase, the three RNN-based predictors estimated the first-order PCA weight reasonably well (Fig. 9d), and the general shape and relatively inferior location of the organs were broadly faithful to the ground-truth. However, organ contours and texture were noticeably blurred; we hypothesize that spatial modeling with PCA may lack robustness when estimating the state of anatomical structures that are unusually far from their average position within the training data. Conversely, the image predicted via the transformer at that time point appeared sharper, with better-preserved texture, but the corresponding liver position was too elevated, reflecting inaccurate PCA-weight forecasting. Notably, in this sequence, the underestimated first-order coefficient for SnAp-1 at the immediately succeeding EI phase ( $t = 55.0\text{s}$ ), together with the moderate horizontal component of the first principal DVF around the top of the liver (Fig. 9c), yielded a more curved diaphragm shape than in the ground truth frame.

Out-of-plane motion (noticeable in sequence 6) and vessel flickering due to blood flow were not always predicted accurately, as our method implicitly assumes that all relevant content is present in the first reference image and remains unchanged over time. Specifically, in sequences 1 and 2, tissue surrounding large vessels in the generated images seemed to contract and expand, intermittently masking bright vascular structures visible in the reference frame at  $t_1$  and mimicking flickering. This effect arises because motion is modeled as belonging strictly to the sagittal plane, which can occasionally make deformations look relatively unnatural.

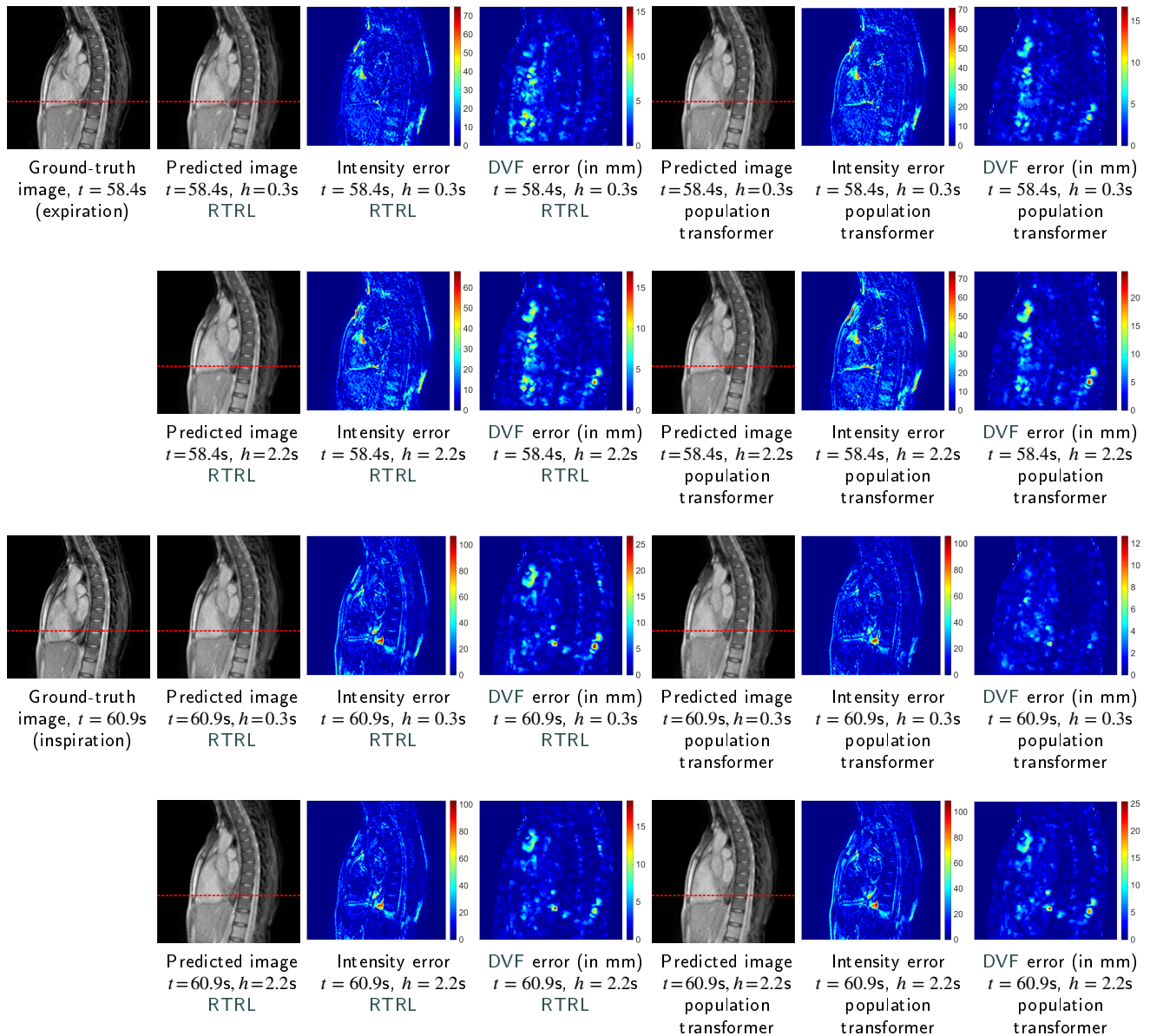


**Figure 15:** Original frames in sequence 1 of the ETH Zürich dataset and corresponding predictions using an RNN trained with RTRL (columns 2-4) and a population transformer trained with the OvGU data (columns 5-7) for  $h = 0.31s$  and  $h = 2.20s$  at two specific time steps in the test set—an EE phase (first two rows, frame 188) and EI phase (last two rows, frame 196)—along with the corresponding pixel-wise intensity and Euclidean deformation-error maps. The hyperparameters optimal for each horizon, including the value of  $n_{cp}$  for RTRL, were selected by grid search on the validation set. A dashed horizontal red line was superimposed on the ground-truth and predicted frames at the same height to help assess the quality of the predicted diaphragm position. The corresponding PCA weights are represented by round markers on Fig. 8 (both figures represent the same prediction runs).

By contrast, motion generally appeared more natural in the predicted ETH Zürich sequences due to more favorable acquisition characteristics (lower noise and higher, more stable contrast).

## 4. Discussion

### 4.1. Comparison with prior results on spatiotemporal respiratory motion forecasting

Comparison with prior works is challenging, as each study relies on a distinct dataset (Table 7). Specifically, the imaging modality, the anatomical regions imaged, the spatial resolution, brightness, contrast, sampling frequency, and noise characteristics, as well as the respiratory-motion amplitude, frequency, and regularity, differ across studies.

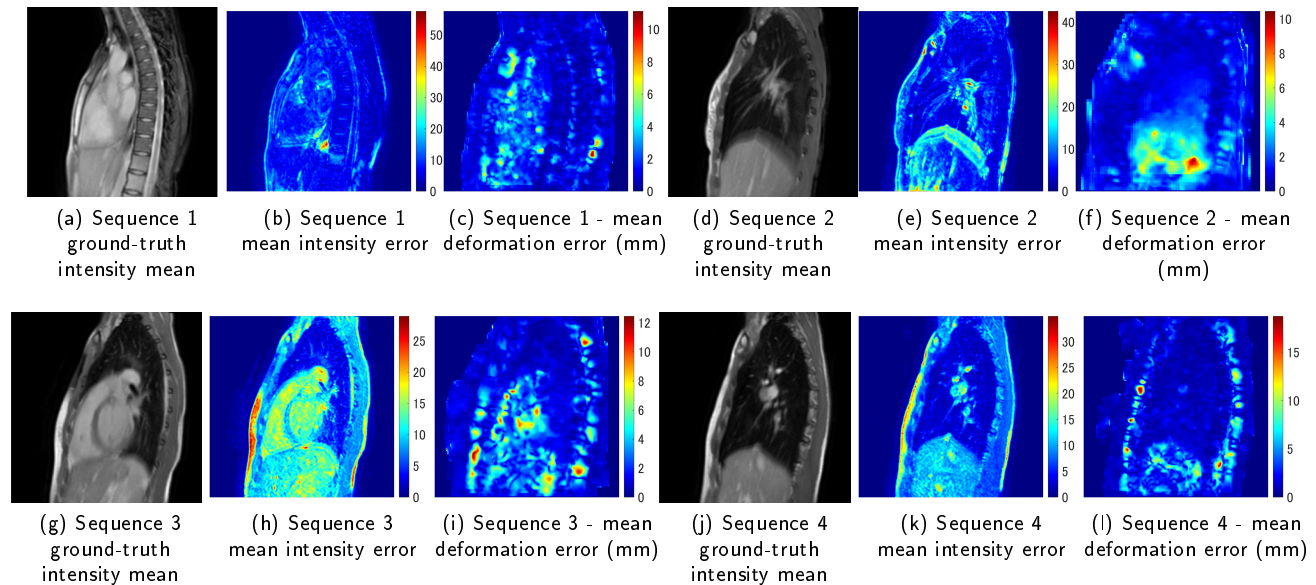


**Figure 16:** Spatial prediction errors for an RNN trained with SnAp-1 at  $h = 1.88s$ , averaged over the test set and 5 evaluation runs, along with the ground-truth intensity mean over the test set, for the four MRI sequences in the ETH Zürich dataset. Hyperparameters, including  $n_{cp}$ , were optimized for each sequence individually using grid search on the validation set.

Work	Prediction method	Video prediction model type [58]	Training scheme	Imaging data	Sampling rate	Amount of data	Response time $h$	Prediction performance
[66, 89]	PCA applied to pixel intensities; prediction with MSSA	Direct pixel synthesis	Subject-specific	1) kV fluoroscopy (phantom); 2) coronal 4DCT cross-sections from lung cancer patient	1) 10Hz 2) 2Hz	1) 1 seq. (repeated 24-frame cycle) 2) 1 seq. (repeated 28-frame cycle)	1) 0.10s 2) 0.50s	1) correlation: $r = 0.998$ SSIM: 0.971 2) $r = 0.999$ SSIM: 0.995
[67]	PCA applied to DVFs; prediction with adaptive-boosted MLPs	Prediction space factorization with explicit transformations	Subject-specific	1) 4D XCAT phantom 2) 4D cine MRI of liver cancer patient (plus on-board sagittal 2D MRI)	1) 8Hz 2) 3Hz	1) 5 sequences (2 min each) 2) 1 sequence of 1 min	1) 0.13s, 0.63s 2) 0.33s	1) 3D (simulated) tumor TE: 1.55mm, 2.60mm 2) SI/AP tumor TE: 1.58mm/1.90mm
[69]	PredNet [53]	Direct pixel synthesis	Population	x/y/z cross-sections from 4DCT of lung cancer patients [90]	not reported	One 10-phase 4DCT sequence for each of the 6 patients	not reported	SSIM: 0.935–0.951
[70]	Voxelmorph-like recurrent AE and spatial transformer	Prediction space factorization with explicit transformations	Population	1) liver sagittal cine MRI from healthy subjects 2) sagittal cross-sections from chest 4DCT [91]	1) 3.13Hz 2) 2.5Hz	1) 12 sequences of 50 frames 2) 10 sequences of 10 frames	1) 0.32s to 1.60s 2) 0.40s to 2.00s	1) local NCC: 0.95–0.97 TE: 0.45–0.77mm 2) TE: 0.28–0.42mm
[26]	Conditional-based transformer with learnable queries	Prediction space factorization with explicit transformations	Population	4D-MR dataset covering the liver and partly the lungs (right hemidiaphragm)	2.22 Hz	80 reconstructed 4D MRI sequences of 31 frames for each of 25 subjects	0.45s	SSIM between 2D frames: $0.78 \pm 0.11$ TE in generated 3D frames: $1.56 \pm 1.13$ mm
Our work	PCA applied to Lucas-Kanade optical-flow field; prediction with RNNs trained online/transformers	Prediction space factorization with explicit transformations	Subject-specific (except for population transformers)	1) ETH Zürich data: chest sagittal slices from 4D cine MRI 2) OvGU data: 2D sagittal liver cine-MR navigator acquisitions	1) 3.18Hz 2) 6.0Hz	1) 4 sequences (200 frames each) from 2 subjects 2) 8 sequences, each corresponding to 498 frames and 1 subject	1) 0.31s to 2.20s 2) 0.17s to 2.17s	SnAp-1 (OvGU, full-frame) Correlation $r$ : 1) 0.987 2) 0.942 SSIM: 1) 0.899 2) 0.660 mean DVF error: 1) 1.41mm 2) 2.73mm

**Table 7**

Comparison with previous studies on frame forecasting in chest and liver imaging. The results reported for our work correspond to Table 4; we selected SnAp-1 as a representative online training algorithm for RNNs and the full-frame evaluation setting, as the latter better matches the other studies, not involving ROIs.

Furthermore, experimental choices—such as the response time and data partitioning into training, validation, and test sets—also vary, further complicating direct comparison.

Chhatkuli et al. reported higher  $r$  and SSIMs than those achieved in our study [66, 89]. However, they used sequences that looped identical respiratory cycles, simulating

artificially regular breathing. Moreover, their forecasting pipeline, relying on PCA applied directly to raw intensities rather than to motion fields (e.g., the optical flow vectors), may be less effective at capturing motion variability components and local deformation patterns. Indeed, they required



**Figure 17:** Ground-truth and predicted ROI images using an RNN trained with UORO, SnAp-1, and DNI, and a subject-specific transformer, at the EI (columns 3-6) and EE (columns 7-10) phases, along with the reference frame warped during the prediction process (column 1), for five representative cases in the OvGU dataset. The horizon is set to  $h = 1.66s$ , and the hyperparameters, including  $n_{cp}$ , were those optimal for that value of  $h$  and each sequence individually. The cross-sections from sequence 4 do not correspond to the test set (defined as  $t \geq t_{341}$ ) but were selected to illustrate forecasting under high motion variability around an irregular deep-inspiration time point. The prediction runs for sequences 1, 4, and 6, are those represented in Fig. 9.

up to twenty principal components for accurate kV fluoroscopic image prediction. We conjecture that such direct pixel-synthesis architectures (including PredNet in [69]) are generally more prone to artifacts and inconsistencies when confronted with large, previously unseen deformations atypical of the training set or when operating at long horizons. In particular, Oprea et al. argued that methods leveraging solely raw pixel intensities "often lead to the regression-to-the-mean problem, visually represented as blurriness" [58]. Similarly, higher SSIMs and lower target-tracking errors were reported in [69, 70], also relying on 4DCT data. However, 4DCT only represents motion averaged over several respiratory cycles, reducing apparent motion variability and preventing clinical applicability for real-time intrafractional motion compensation.

Reported TEs in the literature span roughly from sub-millimetre values to about 2.7mm, which partially overlaps with the magnitude of our 2D Euclidean endpoint errors. Both metrics capture different aspects of performance: TEs assess motion prediction locally, as they depend on a tracked anatomical landmark, whereas Euclidean endpoint errors quantify accuracy across the entire image or a specific region. Specifically, TEs can vary substantially even within a single patient and time point, since motion amplitude is typically greater near the diaphragm than at the lung apex. Those reported in [70] were relatively small (0.45–0.77 mm), partly because evaluation was restricted to right-hemidiaphragm images to avoid cardiac motion, in contrast with some of the ETH Zürich sagittal slices used here, which include the heart and adjacent thoraco-abdominal structures. The 3D geometrical errors achieved by the transformer-based model in [26] ( $1.25 \pm 0.74$ mm at  $h = 0.45$ s) lie in a similar numerical range to the 2D endpoint errors of our sequence-specific transformer on the ETH Zürich data ( $1.37 \pm 0.13$ mm at  $h = 0.63$ s; Fig. 13). However, these values are not directly comparable, given the different problem settings—4D volume reconstruction from partial observations plus forecasting versus 2D frame prediction—and the influence of large static-background regions in 3D images, which can lower the average error.

Several works on respiratory motion forecasting report that accuracy tends to decrease as  $h$  increases, confirming the trend observed in our results. For instance, the tumor center-of-mass TE in XCAT phantom images increased from 1.55mm to 2.60mm, as  $h$  increased from 0.13s to 0.63s in [67]. The same study also reported an increase of the nRMSE of PCA-weight forecasts with  $h$ , similar to the trend shown in Fig. 10. Likewise, prediction of the tumor SI coordinate in cine MRI with dynamically retrained LSTMs in [17] produced RMSEs that increased from 0.48mm at  $h = 0.25$ s to 2.20mm at  $h = 0.75$ s (4Hz sampling). More broadly, works in general video forecasting also report a clear decrease in frame-prediction performance as  $h$  increases [60, 59, 63].

On the OvGU dataset, the best full-frame SSIM, attained by SnAp-1, was  $0.66 \pm 0.03$  (Table 4), which is about 15% lower than the mean SSIM reported in [26] ( $0.78 \pm 0.11$ ), although CIs overlapped. Our relatively low SSIMs mainly

reflect the high noise, low contrast, and irregular motion in the OvGU frames, as already noted in Section 3.4.1. Crucially, warping the initial frame using the optical-flow field—our oracle baseline—yielded an SSIM of only 0.63 on the ROI. Thus, the ROI-based SSIM of SnAp-1 (0.48; Table 4) equals approximately 75% of this upper bound representing perfect forecasting of the reference DVF. In other words, the performance ceiling was largely determined by the registration method rather than the forecasting algorithm. This suggests that our comparative conclusions regarding the effectiveness of online-trained RNNs under limited-data conditions remain valid despite the relatively moderate quality of the OvGU frames.

## 4.2. Methodological considerations

Generally, quantifying performance with multiple metrics allows for a more fine-grained analysis. For instance,  $r$  is sensitive to coherent intensity variations across the image, while the SSIM emphasizes local similarity, extending the local normalized cross-correlation (NCC) by incorporating luminance and contrast factors. However, as noted by Oprea et al., these intensity-based metrics "prefer blurry predictions nearly accommodating the exact ground truth than sharper and plausible but imperfect generations" [58]. This has motivated the use of perceptual, feature-based metrics, such as learned perceptual image patch similarity (LPIPS) [92] or the visual geometry group (VGG) cosine similarity, which compare deep convolutional neural network (CNN) features to better align with human visual perception. Nonetheless, in MR imaging, where intensities are not physically calibrated (unlike CT), geometrical metrics derived from the predicted DVFs remain particularly interpretable. They also relate more directly to intuitive understanding of tumor tracking in radiotherapy.

Our study is the first to address optimal selection of the number of components in the PCA respiratory motion model using a validation-based procedure in chest and liver MR image-sequence forecasting. Prior works on PCA-based motion modeling have commonly used two or three principal components (Section 1.1); we also observed that this choice tended to yield high forecasting accuracy (Section 3.3). Indeed, increasing  $n_{cp}$  from 1 to 2 substantially reduced  $E_{pred}(n_{cp})$  (Fig. 12); a similar drop in the geometrical error on the validation set between the predicted and reference DVFs was also reported in [10], although the latter error purely reflected motion modeling (forecasting was not conducted in that study). Pham et al. mentioned that the third-order coefficient appeared "less predictable" than the first two and "excluding it [had] minimal effect on the final [predicted] volumetric cine MRI" [67], agreeing with its relatively higher noise and lower amplitude in Figs. 7 and 8. Overall, the PCA coefficients in our study resembled those shown in [66, 67, 68], with the dominant respiratory mode appearing rather sinusoidal and smooth. We observed that the optimal value of  $n_{cp}$  depended on both the prediction method and the horizon selected, with high-capacity models and short horizons generally favoring a larger  $n_{cp}$ .

Deep learning–based video-forecasting population models such as those in [69, 70, 26] enable inference on unseen patients without an explicit registration step. Yet, as noted by Romaguera et al., "classical registration approaches still outperform deep learning techniques in several medical imaging applications," underscoring the continued relevance of DIR-based pipelines [70]. The end-to-end strategy adopted in those studies contrasts with our modular pipeline, which follows the general methodology in [66, 67]. Such modularity improves interpretability, as each PCA component and weight can be inspected individually (Sections 3.1 and 3.2.2), and prediction errors in the image space can be traced back to dynamics in the weight domain (Section 3.4.2). Notably, while Nabavi et al. and Romaguera et al. focused mainly on deep-learning–based spatial modeling, we adopted a complementary approach, emphasizing developments on the time-series forecasting module. Indeed, we investigate for the first time online learning algorithms for RNNs in thoraco-abdominal MR image prediction, motivated by the need to adapt to non-stationary respiratory signals in real time with scarce data.

Notably, our framework can accommodate cross-subject–based components, such as the population transformer explored in this study, providing the ability to robustly learn respiratory patterns from large databases. Training that transformer in the PCA space may help mitigate domain-shift effects better than end-to-end image-based architectures in a low-data setting, as the reduced low-dimensional motion representation prevents overfitting to dataset-specific frame appearance. Moreover, using a common learning space enables relatively fair comparison between transformers and RNNs by requiring both to forecast the same compact signal, making differences in performance more directly attributable to their temporal modeling capabilities rather than disparities in input complexity. However, transformers have not achieved strong performance in our experiments. The following section discusses several factors that may explain this outcome.

### 4.3. Remarks on the performance of RNNs and transformers

#### 4.3.1. Factors influencing transformer performance

Data scarcity was likely a major factor limiting the accuracy of lightweight encoder-only transformers in our study. For example, Romaguera et al. reported conditional-based transformer gains over ConvLSTM and ConvGRU models for sagittal cine-MRI prediction at  $h = 0.45s$  (with geometrical errors of 1.25mm, 1.34mm, and 1.60mm for the three models, respectively), but relied on a large dataset from 25 subjects, with approximately 20min of data per subject [26]. Similarly, Jeong et al. observed that full encoder–decoder transformers outperformed LSTM-based baselines for respiratory-trace forecasting at  $h \geq 0.50s$ , using a large cohort (442 patients, 540 traces, mean record length of 145s) [24]. By contrast, our datasets comprise 12 sequences in total, with each acquisition lasting at most 83s. The relative underperformance of transformers in our work

is consistent with their weaker inductive biases compared with RNNs, which can better generalize in low-data regimes (Section 1.2). Specifically, the accuracy of sequence-specific transformers deteriorated rapidly as  $h$  increased (Sections 3.2.1 and 3.4.1), due to their limited training set (first 50.4s of each sequence), while online-trained RNNs could use test-set samples as additional training data. When testing the population transformer on the ETH Zürich data, we downsampled the PCA weights computed from the OvGU acquisitions to 3.18Hz, which reduced temporal granularity. Although polyphase filtering reduces high-frequency artifacts, as it applies an anti-aliasing filter before adjusting the sampling rate, future works could explore multi-start (phase-offset) downsampling, i.e., generating additional training sequences by resampling with several start indices, to avoid discarding information.

The domain shift between the ETH Zürich and OvGU datasets further limited the performance of the population transformer in our experiments. Indeed, the two datasets differ in anatomy and acquisition settings, which changes the semantic meaning, ordering, and characteristics of the PCA modes; for instance, local heart or liver deformations dominated the first-order mode in two of the ETH Zürich sequences, while overall respiratory motion contributed most to the first component in all OvGU acquisitions (Section 3.1). That lack of shared structure and semantic mismatch between components was exacerbated by the variety of respiratory motion patterns across subjects. While we used PCA-weight augmentations during training to increase robustness to ordering, scale, offset, and drift (Section 2.3.3), this strategy was not sufficient to fully resolve component misalignment across subjects in a low-data regime. Still, to our knowledge, our study is the first investigating training and testing with multi-center data for dynamic 2D MR image forecasting. Compared with works where learning and test-set evaluation were performed with more homogeneous cine-MRI acquisition protocols [26], our cross-dataset setting is inherently more challenging for population models. Future research could explore further data augmentations, such as resampling the PCA coefficients at slightly different frequencies or conducting piecewise time-warp between control knots on training examples to simulate global and local variability in frequency, respectively. Furthermore, one could investigate alternative optimization algorithms (e.g., AdamW [93]) or validation objectives to improve generalization. Specifically, the RMSE that we used implicitly upweighted sequences with corresponding higher-variance PCA coefficients, while averaging the per-sequence nRMSE would balance contributions across subjects.

Capping the transformer history length at  $L = 9.5s$  (broadly, two breathing cycles; Table 2) likely constrained performance, although prior works on motion forecasting in cine-MRI used slightly lower SHL values (8.0s and 2.25s in [17] and [26], respectively). RNNs can struggle to capture long-term dependencies due to vanishing gradients and past information compression into a finite-dimensional state. Transformers can, in principle, exploit longer context by

letting each time step directly attend to any other without forced reduction of all history into one state. Nonetheless, we imposed a relatively small  $L$  as a regularization and computational trade-off in a low-data regime, noting that transformers typically require a large amount of data and their time complexity scales as  $\mathcal{O}(L^2)$  with the input length, with large  $L$  potentially limiting clinical feasibility [29] (Section 1.2). Implementing early stopping during hyperparameter tuning could render search over larger grids (including larger  $L$ ) feasible without prohibitive cost.

#### 4.3.2. Notes on RNN accuracy and hyperparameter selection

Predicting the ETH Zürich-derived PCA weights in this work and forecasting the positions of external markers sampled at 3.33Hz in [39] were comparable tasks, given the similar sampling rates and data partition into training, validation, and test sets (30s/30s/remainder, in that study). Excluding RTRL and transformers, which were respectively trained with fewer hidden units ( $d \leq 40$ ) and not examined, in [39], the ordering of the remaining non-baseline methods by horizon-averaged nRMSE matched in both works; SnAp-1 yielded the lowest average nRMSE, whereas that of linear regression was substantially higher (0.335 vs. 1.663 in [39]). Nonetheless, across adaptive predictors, errors were lower in [39] than in this work (Table 3). This is likely because time-dependent marker locations in that study were less noisy, more correlated, and provided more data for training (each sequence comprised 584 samples on average) than our PCA weights derived from global image-based motion fields, which captured more complex, interacting dynamics (Section 3.1). In both studies, the nRMSE tended to increase with  $h$  and linear regression was particularly competitive for 1-step ahead prediction.

Trends relative to hyperparameter optimization for 3.33Hz sampling in [39] also aligned with those observed for the ETH Zürich sequences in this research (Fig. 11). For UORO, the validation nRMSE attained its minimum at similar hidden layer sizes in both works ( $d = 70$  here and  $d = 60$  in [39]). Concerning SnAp-1, the nRMSE tended to decrease with as  $d$  increased, and was minimized at  $d = 110$  in this work and  $d = 120$  in [39]. Lastly, in both studies, the optimal learning rate was  $\eta = 0.01$  for both UORO and DNI, whereas the validation error decreased with  $\eta$  and reached its minimum at  $\eta = 0.02$  for SnAp-1. By contrast, articles on respiratory motion forecasting using data sampled at higher rates, close to 30Hz, typically set  $\eta$  between 0.001 and 0.005 [15, 16, 18]. In our lower-rate, short-sequence setting, larger values of  $\eta$  produced better performance, plausibly because per-step changes were more pronounced and there were fewer online updates for adaptation; this is consistent with [39], where the optimal  $\eta$  decreased as the acquisition frequency increased.

LMS generally ranked higher for intensity-based metrics than for DVF accuracy (Table 4). Indeed, this algorithm has limited capability to forecast noisy signals, hence the validation procedure tended to retain fewer components

than for RNNs (Fig. 12). Selecting a smaller value of  $n_{cp}$  suppressed the influence of higher-order minor deformation modes—often dominated by noise—on predicted displacements. Since respiratory motion was mainly captured by the first one or two components (Figs. 6–9), this effectively resulted in denoising the Lucas–Kanade optical-flow field. This observation suggests that imposing a regularization constraint on locally divergent DVFs during deformable registration may further enhance frame-prediction performance. Regardless, RNNs still achieved higher SSIMs and values of  $r$  at long horizons than LMS on the ETH Zürich data (Fig. 13) and surpassed it at medium-to-long horizons for all metrics on the more irregular OvGU sequences (Figs. 14 and 19). They also generally outperformed linear regression for intermediate-to-high values of  $h$ . This is attributable to the online training regime and their internal state, which acts as a memory and provides greater learning capacity. Notably, linear regression outperformed RNNs for 3D lung-tumor position forecasting in cine MRI in [94], but that may reflect the relatively small horizon selected in that study. We argue that while linear filters can appropriately predict relatively steady breathing signals at shorter response times, online-trained RNNs can better demonstrate their full modeling potential when processing more irregular sequences or operating at longer horizons, consistent with the literature on respiratory motion prediction [4]. As MR-guided radiotherapy systems evolve and acquisition rates increase, typical horizon-to-frame-rate ratios may also rise, further increasing the appeal of dynamically trained RNN-based predictors even for relatively short look-ahead times.

#### 4.4. Limitations and future work

Our MRI datasets are relatively limited, as only ten subjects were involved; therefore, additional anatomies will be required to validate these preliminary findings. Data scarcity was a central limitation of this study and likely constrained forecasting performance, particularly for transformer-based models (Section 4.3.1), but also for dynamically trained RNNs (due to short duration of the sequences). Nevertheless, we argue that performance evaluation remains practically meaningful, as our records are relatively varied. Indeed, our acquisitions span both thoracic and abdominal regions, exhibit markedly different noise and contrast levels (with particularly high noise in several OvGU sequences) and encompass a relatively diverse range of respiratory motion patterns. To our knowledge, this study is the first to investigate frame forecasting in 2D thoraco-abdominal respiratory MRI using publicly available data. The accompanying code is also publicly available, enabling full reproducibility of our experiments [86]. To better leverage scarce data and combine the advantages of offline and online learning, future work could explore pretraining temporal models on larger multi-subject datasets, followed by patient-specific parameter updates during inference. Beyond data limitations, one-shot single-sequence learning and prediction were practically constrained by the computational resources required

for near real-time, per-patient hyperparameter tuning; future research could investigate more efficient tuning schemes.

In clinical settings, out-of-plane motion and local variations in brightness or contrast can hamper accurate deformable registration, thereby reducing image forecasting accuracy (Section 3.4.2). The relatively low accuracy upper bound achieved by the oracle baseline on the OvGU dataset (Table 4) highlighted that DIR quality could substantially cap performance, as discussed in Section 4.1. Specifically, the Lucas–Kanade optical flow algorithm used to estimate motion can produce noisy DVFs, as its basic formulation does not explicitly involve spatial smoothness regularization. Moreover, it relies solely on the brightness-constancy assumption and does not exploit any learned representation of anatomical structures, in contrast to modern deep learning-based registration methods [71]. Future directions include the integration of more advanced registration techniques into our modular pipeline to improve overall prediction accuracy.

Our framework assumes that future frames can be approximated as the result of deforming an initial reference frame. While convenient, this hypothesis is restrictive, as organ motion is three-dimensional and tissue-brightness constancy does not necessarily hold in MRI. One remedy would be to periodically update the motion model and reference frame when errors become large. Another option could be to combine future DVF estimation "with pure synthesis layers to better predict pixels that cannot be copied from other video frames," as suggested in [61]. Although PCA can provide an interpretable representation of respiratory motion, the underlying deformation manifold is not strictly linear. Future work could investigate more expressive dimensionality-reduction methods, such as kPCA or AEs, to better capture complex motion patterns and mitigate domain shift during cross-dataset training and evaluation of population models.

The EI phase was subject to higher inter-cycle variability, and therefore, harder to predict. This manifested as occasional misalignments of the diaphragm, which exhibited relatively high motion amplitudes, between the predicted and ground-truth frames (Figs. 15, 16d–16f, and 17). Similar EI-phase errors, occurring particularly around the diaphragm, have been reported in related work (Section 1.4.2). Taking into account those challenges, a 2mm upper bound on the TE has been proposed as a desirable target in motion compensation during radiotherapy [95]. Nonetheless, margins up to 3mm have also been reported as acceptable in specific contexts, such as ultrasound-based tracking [96]. On the ETH Zürich dataset, horizon-averaged mean geometric errors remained below 2mm for all non-baseline methods (Table 4), and RNNs errors even stayed below 1.5mm across all horizons (Fig. 13). On the OvGU dataset, however, the lowest horizon-averaged ROIs-based geometrical errors, reached by RTRL and SnAp-1, was 2.7mm, likely reflecting lower contrast and higher noise. Furthermore, high-frequency oscillations in the predicted motion trajectories near breathing

irregularities (Figs. 8 and 9) might be a challenge for radiotherapy systems with mechanical response limits, which cannot follow rapidly varying commands. We anticipate that the algorithmic improvements outlined above—including enhanced registration, richer motion representations, and applying online learning to pretrained models—could reduce both this oscillatory behavior and the mean error relative to the 2mm target. Finally, we note that errors measured on well-defined landmarks or clinical points of interest, rather than over the full ROI or field of view (FOV), may be closer to, or below, the 2mm margin guideline.

## 5. Conclusion

In this research, we propose a new approach to forecast respiratory motion in cine MRI to compensate for the latency of MR-guided radiotherapy systems and, in turn, deliver less radiation to healthy tissue. We apply for the first time standard RNNs trained with online learning algorithms to one-shot future frame estimation in dynamic chest and liver MRI sequences, and compare them with lightweight encoder-only transformers, in a low-data regime typical in medical imaging. To our knowledge, this is the first study examining the impact of domain shift on cross-subject model training and evaluation, in cine-MR image forecasting. We combined two public datasets covering thoracic and abdominal imaging (from ETH Zürich and OvGU, respectively), enabling evaluation across diverse breathing patterns and levels of noise and contrast. Our modular framework, based on forecasting projections of deformations between the incoming frame and a reference frame onto the PCA linear subspace, contrasts with recent end-to-end deep-learning architectures [69, 70]. It can decompose complex motion into simpler modes (e.g., cardiac motion and breathing components), benefits from high interpretability, is privacy-friendly, and requires limited data for model fitting.

RTRL and SnAp-1 almost consistently attained the highest cross-dataset and intra-dataset stability (Table 5) and the highest mean performance over horizons  $h \leq 2.2s$ , with geometrical errors of 1.4mm and 2.7mm over the full ETH Zürich images and the ROI of the OvGU frames, respectively (Table 4). Errors on the former dataset were on par with the related literature, satisfying the clinical 2mm threshold guideline [95]. Nevertheless, errors on the latter dataset were higher, mostly due to challenges in deformable registration between high-noise, low-contrast images. For example, the horizon-averaged ROI-based SSIM of SnAp-1 on the OvGU frames (0.48) equaled approximately 75% of the corresponding upper bound SSIM attained by an oracle knowing the exact DVF (0.63). Overall, performance decreased across algorithms as  $h$  increased; RNN accuracy remained relatively high for medium-to-long horizons, primarily because online algorithms learn from recent respiratory patterns and can adapt to non-stationary changes on-the-fly with few training samples. The sequence-specific transformer was competitive for low-to-medium horizons,

but generalization remained limited for the population transformer, except for the shortest horizons on the OvGU sequences. Transformers were particularly constrained by data scarcity, given their weak inductive biases, the small SHLs considered ( $L \leq 10$ s, roughly two breathing cycles), which limited their ability to model long-term dependencies despite self-attention, and the distribution gap between both datasets. Linear regression was the best predictor at low horizons among non-baseline methods in most cases.

Overall, the generated frames were visually plausible, with sharpness and texture largely preserved even for noisy image sequences and long horizons. Organ contours were broadly faithful to the ground truth, although occasional diaphragm misalignment was observed at the EI phase, characterized by higher motion variability. Out-of-plane motion, including vessel flickering induced by transverse blood flow, was challenging to predict, as we modeled deformations as strictly planar. Indeed, all relevant content was assumed to appear in the initial frame and remain visible across time, as future frames were estimated via vector-based resampling of that reference image. Moreover, pronounced oscillations of the predicted trajectories sometimes occurred around breathing irregularities, which may affect mechanical guidance of the radiation beam.

Key algorithmic improvements include exploring more accurate registration methods, richer motion representations (e.g., kPCA or VAEs), faster, more efficient (near real-time) hyperparameter tuning, online adaptation of pretrained population models, and transformer variants specialized in time series forecasting. Furthermore, training transformer-based models with more extensive data would help provide a fairer assessment of their capabilities. Subsequent studies should also further assess robustness to irregular breathing, anatomical variability, and differences in acquisition protocols. While 2D chest and liver cine-MRI prediction provides useful information about future target motion, its clinical benefits can only be fully realized with downstream modules, such as tumor and OAR segmentation and 3D image generation from partial 2D views to compensate for the imaging limitations of MR-LINAC systems. The implementation and evaluation of these components, integrated with video prediction, are left as future work.

## Conflicts of interest statement

The authors declare no conflict of interest.

## Funding

This work was supported by the Epson International Scholarship Foundation and the Japan Student Services Organization.

## Acknowledgments

We are thankful to Prof. Masaki Sekino, Prof. Ichiro Sakuma, Prof. Hitoshi Tabata (The University of Tokyo,

Graduate School of Engineering) and Dr. Kiwoo Lee (Edogawa Hospital, Department of Radiology) for their thoughtful feedback and recommendations that helped enhance the quality of this research. We also express gratitude to Dr. Cristian Le Minh (Max Planck Institute) and Mr. Suryanarayanan N.A.V. (The University of Tokyo, Graduate School of Engineering) for their assistance regarding software and coding.

## Data and code availability

The data and code used in this research are publicly available online [77, 80, 86].

## References

- [1] E. Huynh, A. Hosny, C. Guthrie, D. S. Bitterman, S. F. Petit, D. A. Haas-Kogan, B. Kann, H. J. Aerts, R. H. Mak, Artificial intelligence in radiation oncology, *Nature Reviews Clinical Oncology* 17 (2020) 771–781.
- [2] S. Sarudis, A. Karlsson Hauer, J. Nyman, A. Bäck, Systematic evaluation of lung tumor motion using four-dimensional computed tomography, *Acta Oncologica* 56 (2017) 525–530.
- [3] S. Takao, N. Miyamoto, T. Matsuura, R. Onimaru, N. Katoh, T. Inoue, K. L. Sutherland, R. Suzuki, H. Shirato, S. Shimizu, Intrafractional baseline shift or drift of lung tumor motion during gated radiation therapy with a real-time tumor-tracking system, *International Journal of Radiation Oncology - Biology - Physics* 94 (2016) 172–180.
- [4] P. Verma, H. Wu, M. Langer, I. Das, G. Sandison, Survey: real-time tumor motion prediction for image-guided radiation treatment, *Computing in Science & Engineering* 13 (2010) 24–35.
- [5] J. S. Witt, S. A. Rosenberg, M. F. Bassetti, Mri-guided adaptive radiotherapy for liver tumours: visualising the future, *The Lancet Oncology* 21 (2020) e74–e82.
- [6] G. Wang, Z. Li, G. Li, G. Dai, Q. Xiao, L. Bai, Y. He, Y. Liu, S. Bai, Real-time liver tracking algorithm based on LSTM and SVR networks for use in surface-guided radiation therapy, *Radiation Oncology* 16 (2021) 1–12.
- [7] J. Ehrhardt, C. Lorenz, et al., 4D modeling and estimation of respiratory motion for radiation therapy, volume 10, Springer, 2013.
- [8] Q. Zhang, A. Pevsner, A. Hertanto, Y.-C. Hu, K. E. Rosenzweig, C. C. Ling, G. S. Mageras, A patient-specific respiratory model of anatomical motion for radiation treatment planning, *Medical physics* 34 (2007) 4772–4781.
- [9] H. Chen, Z. Zhong, Y. Yang, J. Chen, L. Zhou, X. Zhen, X. Gu, Internal motion estimation by internal-external motion modeling for lung cancer radiotherapy, *Scientific reports* 8 (2018) 1–14.
- [10] R. Li, J. H. Lewis, X. Jia, T. Zhao, W. Liu, S. Wuenschel, J. Lamb, D. Yang, D. A. Low, S. B. Jiang, On a PCA-based lung motion model, *Physics in Medicine & Biology* 56 (2011) 6009.
- [11] B. Stemkens, R. H. Tjissen, B. D. De Senneville, J. J. Lagendijk, C. A. Van Den Berg, Image-driven, model-based 3D abdominal motion estimation for MR-guided radiotherapy, *Physics in Medicine & Biology* 61 (2016) 5335.
- [12] W. Harris, L. Ren, J. Cai, Y. Zhang, Z. Chang, F.-F. Yin, A technique for generating volumetric cine-magnetic resonance imaging, *International Journal of Radiation Oncology - Biology - Physics* 95 (2016) 844–853.
- [13] L. V. Romaguera, T. Mezheritsky, R. Mansour, W. Tanguay, S. Kadoury, Predictive online 3D target tracking with population-based generative networks for image-guided radiotherapy, *International Journal of Computer Assisted Radiology and Surgery* 16 (2021) 1213–1225.
- [14] R. Wang, X. Liang, X. Zhu, Y. Xie, A feasibility of respiration prediction based on deep bi-LSTM for real-time tumor tracking, *IEEE Access* 6 (2018) 51262–51268.

- [15] H. Lin, C. Shi, B. Wang, M. F. Chan, X. Tang, W. Ji, Towards real-time respiratory motion prediction based on long short-term memory neural networks, *Physics in Medicine & Biology* 64 (2019) 085010.
- [16] S. Yu, J. Wang, J. Liu, R. Sun, S. Kuang, L. Sun, Rapid prediction of respiratory motion based on bidirectional gated recurrent unit network, *IEEE Access* 8 (2020) 49424–49435.
- [17] E. Lombardo, M. Rabe, Y. Xiong, L. Nierer, D. Cusumano, L. Placidi, L. Boldrini, S. Corradini, M. Niyazi, C. Belka, et al., Offline and online LSTM networks for respiratory motion prediction in MR-guided radiotherapy, *Physics in Medicine & Biology* 67 (2022) 095006.
- [18] P. Samadi Miandoab, S. Saramad, S. Setayeshi, Respiratory motion prediction based on deep artificial neural networks in CyberKnife system: A comparative study, *Journal of Applied Clinical Medical Physics* 24 (2023) e13854.
- [19] D. Bahdanau, Neural machine translation by jointly learning to align and translate, *arXiv preprint arXiv:1409.0473* (2014).
- [20] A. Vaswani, N. Shazeer, N. Parmar, J. Uszkoreit, L. Jones, A. N. Gomez, Ł. Kaiser, I. Polosukhin, Attention is all you need, *Advances in neural information processing systems* 30 (2017).
- [21] S. Li, X. Jin, Y. Xuan, X. Zhou, W. Chen, Y.-X. Wang, X. Yan, Enhancing the locality and breaking the memory bottleneck of transformer on time series forecasting, *Advances in neural information processing systems* 32 (2019).
- [22] H. Zhou, S. Zhang, J. Peng, S. Zhang, J. Li, H. Xiong, W. Zhang, Informer: Beyond efficient transformer for long sequence time-series forecasting, in: *Proceedings of the AAAI conference on artificial intelligence*, volume 35, 2021, pp. 11106–11115.
- [23] H. Wu, J. Xu, J. Wang, M. Long, Autoformer: Decomposition transformers with auto-correlation for long-term series forecasting, *Advances in neural information processing systems* 34 (2021) 22419–22430.
- [24] S. Jeong, W. Cheon, S. Cho, Y. Han, Clinical applicability of deep learning-based respiratory signal prediction models for four-dimensional radiation therapy, *Plos one* 17 (2022) e0275719.
- [25] L. Shi, S. Han, J. Zhao, Z. Kuang, W. Jing, Y. Cui, Z. Zhu, Respiratory prediction based on multi-scale temporal convolutional network for tracking thoracic tumor movement, *Frontiers in Oncology* 12 (2022) 884523.
- [26] L. V. Romaguera, S. Alley, J.-F. Carrier, S. Kadoury, Conditional-based transformer network with learnable queries for 4D deformation forecasting and tracking, *IEEE Transactions on Medical Imaging* 42 (2023) 1603–1618.
- [27] P. Haller, J. Golde, A. Akbik, BabyHGRN: Exploring RNNs for sample-efficient training of language models, 2024. URL: <https://arxiv.org/abs/2412.15978>. *arXiv:2412.15978*.
- [28] S. Islam, H. Elmekki, A. Elsebai, J. Bentahar, N. Drawel, G. Rjoub, W. Pedrycz, A comprehensive survey on applications of transformers for deep learning tasks, *Expert Systems with Applications* 241 (2024) 122666.
- [29] L. Wimmert, M. Nielsen, F. Madesta, T. Gauer, C. Hofmann, R. Werner, Benchmarking machine learning-based real-time respiratory signal predictors in 4d sbct, *Medical Physics* 51 (2024) 3173–3183.
- [30] M. Tan, H. Peng, X. Liang, Y. Xie, Z. Xia, J. Xiong, LSTformer: Long short-term transformer for real time respiratory prediction, *IEEE Journal of Biomedical and Health Informatics* 26 (2022) 5247–5257.
- [31] K. Zhang, J. Yu, J. Liu, Q. Li, S. Jin, Z. Su, X. Xu, Z. Dai, X. Wang, H. Zhang, LGEANet: LSTM-global temporal convolution-external attention network for respiratory motion prediction, *Medical Physics* 50 (2023) 1975–1989.
- [32] T. P. Teo, S. B. Ahmed, P. Kawalec, N. Alayoubi, N. Bruce, E. Lyn, S. Pistorius, Feasibility of predicting tumor motion using online data acquired during treatment and a generalized neural network optimized with offline patient tumor trajectories, *Medical physics* 45 (2018) 830–845.
- [33] H. Jaeger, Tutorial on training recurrent neural networks, covering BPPT, RTRL, EKF and the "echo state network" approach, volume 5, GMD-Forschungszentrum Informationstechnik Bonn, 2002.
- [34] R. J. Williams, D. Zipser, A learning algorithm for continually running fully recurrent neural networks, *Neural computation* 1 (1989) 270–280.
- [35] K. Jiang, F. Fujii, T. Shiinoki, Prediction of lung tumor motion using nonlinear autoregressive model with exogenous input, *Physics in Medicine & Biology* 64 (2019) 21NT02.
- [36] M. Mafi, S. M. Moghadam, Real-time prediction of tumor motion using a dynamic neural network, *Medical & biological engineering & computing* 58 (2020) 529–539.
- [37] M. Pohl, M. Uesaka, K. Demachi, R. B. Chhatkuli, Prediction of the motion of chest internal points using a recurrent neural network trained with real-time recurrent learning for latency compensation in lung cancer radiotherapy, *Computerized Medical Imaging and Graphics* (2021) 101941.
- [38] M. Pohl, M. Uesaka, H. Takahashi, K. Demachi, R. B. Chhatkuli, Prediction of the position of external markers using a recurrent neural network trained with unbiased online recurrent optimization for safe lung cancer radiotherapy, *Computer Methods and Programs in Biomedicine* 222 (2022) 106908.
- [39] M. Pohl, M. Uesaka, H. Takahashi, K. Demachi, R. B. Chhatkuli, Real-time respiratory motion forecasting with online learning of recurrent neural networks for accurate targeting in externally guided radiotherapy, *Computer Methods and Programs in Biomedicine* (2025) 108828.
- [40] R. J. Williams, J. Peng, An efficient gradient-based algorithm for online training of recurrent network trajectories, *Neural computation* 2 (1990) 490–501.
- [41] C. Tallic, Y. Ollivier, Unbiased online recurrent optimization, in: *International Conference on Learning Representations*, 2018.
- [42] A. Mujika, F. Meier, A. Steger, Approximating real-time recurrent learning with random kronecker factors, *Advances in Neural Information Processing Systems* 31 (2018) 6594–6603.
- [43] C. Roth, I. Kanitscheider, I. Fiete, Kernel rnn learning (kernl), in: *International Conference on Learning Representations*, 2018.
- [44] F. Benzinger, M. M. Gauy, A. Mujika, A. Martinsson, A. Steger, Optimal kronecker-sum approximation of real time recurrent learning, in: *International Conference on Machine Learning*, PMLR, 2019, pp. 604–613.
- [45] J. M. Murray, Local online learning in recurrent networks with random feedback, *ELife* 8 (2019) e43299.
- [46] J. Menick, E. Elsen, U. Evci, S. Osindero, K. Simonyan, A. Graves, A practical sparse approximation for real time recurrent learning, in: *International Conference on Learning Representations*, 2021.
- [47] O. Marschall, K. Cho, C. Savin, A unified framework of online learning algorithms for training recurrent neural networks, *Journal of Machine Learning Research* 21 (2020) 1–34.
- [48] M. Jaderberg, W. M. Czarnecki, S. Osindero, O. Vinyals, A. Graves, D. Silver, K. Kavukcuoglu, Decoupled neural interfaces using synthetic gradients, in: *International Conference on Machine Learning*, PMLR, 2017, pp. 1627–1635.
- [49] S. Hochreiter, J. Schmidhuber, Long short-term memory, *Neural computation* 9 (1997) 1735–1780.
- [50] M. Minderer, C. Sun, R. Villegas, F. Cole, K. P. Murphy, H. Lee, Unsupervised learning of object structure and dynamics from videos, *Advances in Neural Information Processing Systems* 32 (2019).
- [51] A. Gupta, S. Tian, Y. Zhang, J. Wu, R. Martín-Martín, L. Fei-Fei, Maskvit: Masked visual pre-training for video prediction, *arXiv preprint arXiv:2206.11894* (2022).
- [52] X. Jin, H. Xiao, X. Shen, J. Yang, Z. Lin, Y. Chen, Z. Jie, J. Feng, S. Yan, Predicting scene parsing and motion dynamics in the future, *Advances in neural information processing systems* 30 (2017).
- [53] W. Lotter, G. Kreiman, D. Cox, Deep predictive coding networks for video prediction and unsupervised learning, 2017. *arXiv:1605.08104*.
- [54] P. Luc, C. Couprie, Y. Lecun, J. Verbeek, Predicting future instance segmentation by forecasting convolutional features, in: *Proceedings of the European Conference on Computer Vision (ECCV)*, 2018, pp. 584–599.

- [55] X. Shi, Z. Chen, H. Wang, D.-Y. Yeung, W.-K. Wong, W.-c. Woo, Convolutional lstm network: A machine learning approach for precipitation nowcasting, *Advances in neural information processing systems* 28 (2015).
- [56] I. Sutskever, O. Vinyals, Q. V. Le, Sequence to sequence learning with neural networks, *Advances in neural information processing systems* 27 (2014).
- [57] N. Srivastava, E. Mansimov, R. Salakhudinov, Unsupervised learning of video representations using LSTMs, in: *International conference on machine learning*, PMLR, 2015, pp. 843–852.
- [58] S. Oprea, P. Martinez-Gonzalez, A. Garcia-Garcia, J. A. Castro-Vargas, S. Orts-Escolano, J. Garcia-Rodriguez, A. Argyros, A review on deep learning techniques for video prediction, *IEEE Transactions on Pattern Analysis and Machine Intelligence* (2020).
- [59] R. Villegas, J. Yang, S. Hong, X. Lin, H. Lee, Decomposing motion and content for natural video sequence prediction, in: *5th International Conference on Learning Representations, ICLR 2017*, 2017.
- [60] C. Finn, I. Goodfellow, S. Levine, Unsupervised learning for physical interaction through video prediction, *Advances in neural information processing systems* 29 (2016).
- [61] Z. Liu, R. A. Yeh, X. Tang, Y. Liu, A. Agarwala, Video frame synthesis using deep voxel flow, in: *Proceedings of the IEEE International Conference on Computer Vision*, 2017, pp. 4463–4471.
- [62] M. Jaderberg, K. Simonyan, A. Zisserman, et al., Spatial transformer networks, *Advances in neural information processing systems* 28 (2015).
- [63] M. Babaeizadeh, C. Finn, D. Erhan, R. H. Campbell, S. Levine, Stochastic variational video prediction, *arXiv preprint arXiv:1710.11252* (2017).
- [64] E. Denton, R. Fergus, Stochastic video generation with a learned prior, in: *International conference on machine learning*, PMLR, 2018, pp. 1174–1183.
- [65] Y.-J. Gong, Y.-K. Li, R. Zhou, Z. Liang, Y. Zhang, T. Cheng, Z.-J. Zhang, A novel approach for estimating lung tumor motion based on dynamic features in 4d-ct, *Computerized Medical Imaging and Graphics* 115 (2024) 102385.
- [66] R. B. Chhatkuli, K. Demachi, N. Miyamoto, M. Uesaka, A. Haga, et al., Dynamic image prediction using principal component and multi-channel singular spectral analysis: a feasibility study, *Open Journal of Medical Imaging* 5 (2015) 133.
- [67] J. Pham, W. Harris, W. Sun, Z. Yang, F.-F. Yin, L. Ren, Predicting real-time 3D deformation field maps (DFM) based on volumetric cine MRI (VC-MRI) and artificial neural networks for on-board 4D target tracking: a feasibility study, *Physics in Medicine & Biology* 64 (2019) 165016.
- [68] W. Liu, A. Sawant, D. Ruan, Prediction of high-dimensional states subject to respiratory motion: a manifold learning approach, *Physics in Medicine & Biology* 61 (2016) 4989.
- [69] S. Nabavi, M. Abdoos, M. E. Moghaddam, M. Mohammadi, Respiratory motion prediction using deep convolutional long short-term memory network, *Journal of Medical Signals and Sensors* 10 (2020) 69.
- [70] L. V. Romaguera, R. Plantefève, F. P. Romero, F. Hébert, J.-F. Carrier, S. Kadoury, Prediction of in-plane organ deformation during free-breathing radiotherapy via discriminative spatial transformer networks, *Medical image analysis* 64 (2020) 101754.
- [71] G. Balakrishnan, A. Zhao, M. R. Sabuncu, J. Guttag, A. V. Dalca, Voxelmorph: a learning framework for deformable medical image registration, *IEEE transactions on medical imaging* 38 (2019) 1788–1800.
- [72] L. V. Romaguera, T. Mezheritsky, R. Mansour, J.-F. Carrier, S. Kadoury, Probabilistic 4D predictive model from in-room surrogates using conditional generative networks for image-guided radiotherapy, *Medical image analysis* 74 (2021) 102250.
- [73] N. Gunnarsson, J. Sjölund, P. Kimstrand, T. B. Schön, Online learning in motion modeling for intra-interventional image sequences, in: *International Conference on Medical Image Computing and Computer-Assisted Intervention*, Springer, 2024, pp. 706–716.
- [74] Q. Xu, R. J. Hamilton, R. A. Schowengerdt, B. Alexander, S. B. Jiang, Lung tumor tracking in fluoroscopic video based on optical flow, *Medical physics* 35 (2008) 5351–5359.
- [75] Y. Akino, R.-J. Oh, N. Masai, H. Shiomi, T. Inoue, Evaluation of potential internal target volume of liver tumors using cine-MRI, *Medical physics* 41 (2014) 111704.
- [76] J. Dhont, J. Vandemeulebroucke, D. Cusumano, L. Boldrini, F. Cellini, V. Valentini, D. Verellen, Multi-object tracking in MRI-guided radiotherapy using the tracking-learning-detection framework, *Radiotherapy and Oncology* 138 (2019) 25–29.
- [77] ETH Zürich, Biomedical Image Computing, Datasets, 4D MRI lung data, <https://bmic.ee.ethz.ch/research/datasets.html>, 2021. [Online; accessed 26-May-2021].
- [78] M. von Siebenthal, G. Szekely, U. Gamper, P. Boesiger, A. Lomax, P. Cattin, 4D MR imaging of respiratory organ motion and its variability, *Physics in Medicine & Biology* 52 (2007) 1547.
- [79] D. Boye, G. Samei, J. Schmidt, G. Székely, C. Tanner, Population based modeling of respiratory lung motion and prediction from partial information, in: *Medical Imaging 2013: Image Processing*, volume 8669, International Society for Optics and Photonics, 2013, p. 86690U.
- [80] G. Gulamhussene, A. Meyer, M. Rak, C. Lübeck, J. Omari, M. Pech, C. Hansen, 2D MRI liver slices with navigator frames. A training and test data set for image based 4D MRI reconstruction. (Part II), 2021. URL: <http://open-science.ub.ovgu.de/xmlui/handle/684882692/88>. doi:10.24352/UB.OVGU-2021-071.
- [81] G. Gulamhussene, A. Meyer, M. Rak, O. Bashkanov, J. Omari, M. Pech, C. Hansen, Predicting 4d liver mri for mr-guided interventions, *Computerized Medical Imaging and Graphics* 101 (2022) 102122.
- [82] B. D. Lucas, T. Kanade, et al., An iterative image registration technique with an application to stereo vision (1981).
- [83] J.-Y. Bouguet, et al., Pyramidal implementation of the affine Lucas Kanade feature tracker, description of the algorithm, *Intel Corporation* 5 (2001) 4.
- [84] D. Fleet, Y. Weiss, Optical flow estimation, in: *Handbook of mathematical models in computer vision*, Springer, 2006, pp. 237–257.
- [85] R. Pascanu, T. Mikolov, Y. Bengio, On the difficulty of training recurrent neural networks, in: *International conference on machine learning*, 2013, pp. 1310–1318.
- [86] M. Pohl, Future frame prediction in 2D cine-MR images: latest release, 2025. URL: <https://doi.org/10.5281/zenodo.13896201>. doi:10.5281/zenodo.13896201.
- [87] T. Akiba, S. Sano, T. Yanase, T. Ohta, M. Koyama, Optuna: A next-generation hyperparameter optimization framework, in: *Proceedings of the 25th ACM SIGKDD International Conference on Knowledge Discovery and Data Mining*, 2019.
- [88] Z. Wang, A. C. Bovik, H. R. Sheikh, E. P. Simoncelli, Image quality assessment: from error visibility to structural similarity, *IEEE transactions on image processing* 13 (2004) 600–612.
- [89] R. B. Chhatkuli, Development of a markerless tumor prediction system using principal component analysis and multi-channel singular spectral analysis with real-time respiratory phase recognition in radiation therapy, Ph.D. thesis, The University of Tokyo, 2016. URL: [https://repository.dl.itc.u-tokyo.ac.jp/record/48459/files/A32580\\_summary.pdf](https://repository.dl.itc.u-tokyo.ac.jp/record/48459/files/A32580_summary.pdf).
- [90] J. Vandemeulebroucke, D. Sarrut, P. Clarysse, et al., The POPI-model, a point-validated pixel-based breathing thorax model, in: *XVth international conference on the use of computers in radiation therapy (ICCR)*, volume 2, 2007, pp. 195–199.
- [91] E. Castillo, R. Castillo, J. Martinez, M. Shenoy, T. Guerrero, Four-dimensional deformable image registration using trajectory modeling, *Physics in Medicine & Biology* 55 (2009) 305.
- [92] R. Zhang, P. Isola, A. A. Efros, E. Shechtman, O. Wang, The unreasonable effectiveness of deep features as a perceptual metric, in: *Proceedings of the IEEE conference on computer vision and pattern recognition*, 2018, pp. 586–595.

- [93] I. Loshchilov, F. Hutter. Decoupled weight decay regularization, arXiv preprint arXiv:1711.05101 (2017).
- [94] Y. Li, Z. Li, J. Zhu, B. Li, H. Shu, D. Ge. Online prediction for respiratory movement compensation: a patient-specific gating control for MRI-guided radiotherapy, *Radiation Oncology* 18 (2023) 149.
- [95] M. J. Murphy, Tracking moving organs in real time, in: *Seminars in radiation oncology*, volume 14, Elsevier, 2004, pp. 91–100.
- [96] F. Preiswerk, V. De Luca, P. Arnold, Z. Celicanin, L. Petrusca, C. Tanner, O. Bieri, R. Salomir, P. C. Cattin, Model-guided respiratory organ motion prediction of the liver from 2d ultrasound, *Medical image analysis* 18 (2014) 740–751.
- [97] G. Zhang, T.-C. Huang, T. Guerrero, K.-P. Lin, C. Stevens, G. Starkschall, K. Forster, Use of three-dimensional (3D) optical flow method in mapping 3D anatomic structure and tumor contours across four-dimensional computed tomography data, *Journal of applied clinical medical physics* 9 (2008) 59–69.

## A. Appendix: Dataset characteristics

The characteristics of the datasets used in our study are provided in Table 8.

## B. Appendix : Optimization of MR image registration parameters

In this appendix, we describe the optimization of the iterative and pyramidal Lucas–Kanade optical-flow algorithm parameters with grid search, illustrated with the ETH Zürich dataset (step 1.1 in Fig. 5; see Section 2.2). The same methodology was applied to the OvGU images for consistency. We perform this optimization for each sequence by minimizing the registration error  $E_{\text{ref}}(\vec{u})$  using the first  $M_{\text{DIR}}$  frames, defined as follows:

$$E_{\text{ref}}(\vec{u}) = \sqrt{\frac{1}{(M_{\text{DIR}} - 1)|I|} \sum_{k=2}^{M_{\text{DIR}}} \sum_{\vec{x}} \delta(\vec{u}, \vec{x}, t_k)^2} \quad (14)$$

In that equation,  $|I|$  and  $\delta(\vec{u}, \vec{x}, t_k)$  refer to the number of pixels in each frame and the instantaneous registration error at pixel  $\vec{x}$  and time  $t_k$  using the 4D vector field  $\vec{u}$ , defined in Eq. 11, respectively. The value of  $\vec{u}$  minimizing  $E_{\text{ref}}(\vec{u})$  is considered the *reference* (i.e., proxy ground-truth) DVF, representing the motion to forecast. In contrast,  $E_{\text{pred}}(n_{\text{cp}})$ , defined in Eq. 13, is minimized with respect to  $n_{\text{cp}}$  on the validation set to obtain an accurate *predicted* DVF (Sections 2.5 and 3.3).  $M_{\text{DIR}}$  is set such that  $t_{M_{\text{DIR}}} = 28.3\text{s}$ ; for online forecasting algorithms,  $M_{\text{DIR}} = M_{\text{train}}$  (Table 11). The tuned parameters (definitions in [37]<sup>11</sup>) and selected values are summarized in Table 9.

<sup>10</sup>For reference, the OvGU sequences numbered from 1 to 8 correspond to the following identifiers in [80], in order: 2020-11-10\_KS81\_Nav\_Pur\_1, 2020-11-12\_QN76\_Nav\_Pur\_1, 2020-11-17\_CS31\_Nav\_Pur\_2, 2020-11-17\_JY02\_Nav\_Pur\_2, 2020-11-23\_ON65\_Nav\_Pur\_2, 2020-11-23\_PS11\_Nav\_Pur\_1, 2020-11-25\_I129\_Nav\_Pur\_1, 2020-11-26\_NE38\_Nav\_Pur\_1.

<sup>11</sup>Variable notations were slightly adapted from [37] for clarity. For instance, here,  $n_{\text{layer}}^{LK}$  denotes the number of pyramid levels in the Lucas–Kanade optical-flow algorithm, distinct from the  $n_{\text{layer}}$  parameter used for the transformer network.  $E_{\text{ref}}$  refers to the same quantity as  $e_{\text{DVF}}$  in [37].

Dataset	ETH Zürich	OvGU
Body part	Thorax	Abdomen
Acquisition type	Cross-sections from reconstructed 4D-MR	2D navigator slices
Number of sequences	4	8 <sup>10</sup>
Whole image FOV (mm)	270 × 270 (seq. 1–2) 290 × 290 (seq. 3–4)	255 × 320
In-plane resolution (mm)	1.0 × 1.0	1.818 × 1.818
Through-plane resolution	1.0mm	4.0mm
Sampling rate	3.18Hz	6.0Hz
Number of frames	200	498
Breathing characteristics	Regular	Rather irregular
Noise level	Low	High
Organ contrast	High, stable	Low, variable
Maximum ROI width	n/a	158mm
Maximum ROI height	n/a	262mm
Number of breathing cycles		
- minimum/maximum	14 - 28	13 - 26
- average	16	19.75

**Table 8**

General characteristics of the two cine-MRI datasets.

Parameter	Parameter range	Best value
Standard deviation of the Gaussian filter applied to the initial image, $\sigma_{\text{init}}$	{0.1, 0.5, 1.0}	0.1
Std. deviation of the Gaussian filter used for downsampling at each layer, $\sigma_{\text{sub}}$	{0.1, 0.5, 1.0}	-
Standard deviation of the Gaussian kernel weighting the moment matrix, $\sigma_{\text{support}}$	{1.0, 2.0, 3.0, 4.0}	2.0 or 3.0
Number of layers, $n_{\text{layer}}^{LK}$	{1, 2, 3}	2 or 3
Number of iterations, $n_{\text{iter}}$	{1, 2, 3}	1

**Table 9**

Hyperparameter range for optimization of the pyramidal iterative Lucas–Kanade optical-flow algorithm, along with the values that experimentally led to the lowest registration error  $E_{\text{ref}}$  on the ETH Zürich sequences.

On the ETH Zürich sequences,  $E_{\text{ref}}$  generally increased with  $\sigma_{\text{init}}$  and  $\sigma_{\text{sub}}$ , suggesting that extra smoothing may be detrimental when noise levels are moderate (Fig. 18).  $E_{\text{ref}}$  was a convex function of  $\sigma_{\text{support}}$ , with  $\sigma_{\text{support}} = 1.0$  producing the highest errors. Using a single pyramid level yielded poor registration accuracy, consistent with the large amplitude of respiratory motion relative to the in-plane resolution (1mm isotropic pixel spacing after resampling). This aligns with prior recommendations to use a multiresolution scheme for optical-flow estimation in thoracic imaging [74, 97]. Multiscale designs are also common in learning-based models that predict spatial transformations (e.g., U-Net encoder–decoder architecture in [71] or multiscale residual blocks in [70]). By contrast, using several iterations did not improve performance, as  $E_{\text{ref}}$  increased with  $n_{\text{iter}}$ .  $\sigma_{\text{support}}$  and  $n_{\text{layer}}^{LK}$  had the largest impact on registration accuracy; optimizing them reduced the marginal minimum of  $E_{\text{ref}}$  (over all other parameters in the grid) by 19.6% and 5.4%, respectively. Overall, these trends are consistent with prior observations in thoracic CT registration [37].

<sup>12</sup>In our training implementation for the population transformer, drift augmentation adjusted future targets based on the terminal input window

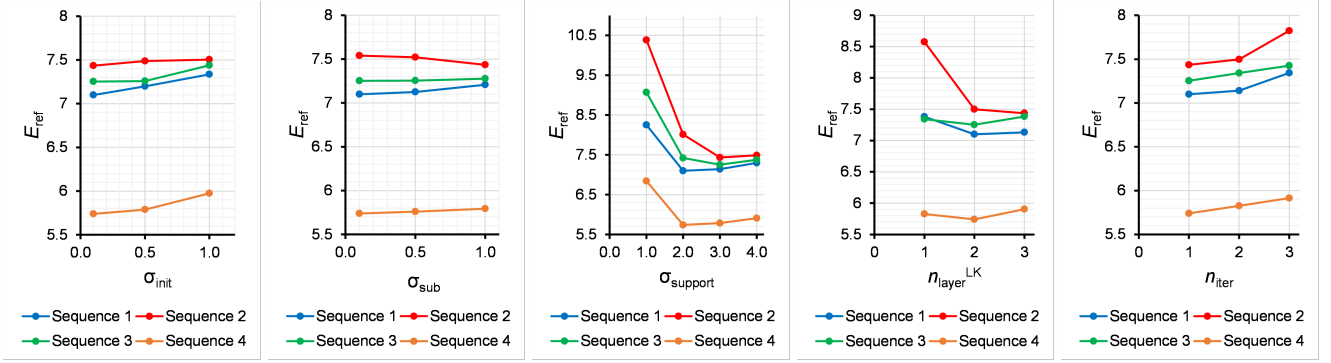


**Figure 18:** RMS registration error,  $E_{\text{ref}}$ , as a function of the iterative and pyramidal Lucas–Kanade optical-flow parameters, for each sequence of the ETH Zürich dataset (Eq. 14). Given one parameter, each point in the associated graph corresponds to the minimum of  $E_{\text{ref}}$  over every possible combination of the other parameters in the grid (Table 9).

### C. Appendix : Notes on the PCA respiratory motion model

In this section, we derive the equations of the motion model introduced in Section 2.2, starting from the conventional formulation of PCA. This motion model is sequence-specific and similar to the original one proposed in [8], although we apply PCA to internal motion only and do not rely on surrogate data. We form the matrix  $X \in \mathbb{R}^{M \times 2|I|}$  that contains all motion information for a given sequence up to time step  $M \in \mathbb{N}$ :

$$X = \begin{bmatrix} u_x(\vec{x}_1, t_1) & u_y(\vec{x}_1, t_1) & u_x(\vec{x}_2, t_1) & \dots & u_y(\vec{x}_{|I|}, t_1) \\ \vdots & \vdots & \vdots & \ddots & \vdots \\ u_x(\vec{x}_1, t_M) & u_y(\vec{x}_1, t_M) & u_x(\vec{x}_2, t_M) & \dots & u_y(\vec{x}_{|I|}, t_M) \end{bmatrix} \quad (15)$$

Here,  $u_x(\vec{x}, t)$  and  $u_y(\vec{x}, t)$  respectively refer to the  $x$  and  $y$  components of  $\vec{u}(\vec{x}, t)$ , the deformation vector at time  $t$  and pixel  $\vec{x}$ . By abuse of notation, we set  $M$  to the number of training images ( $M_{\text{train}}$ ) in this appendix. We denote by  $\mu_X \in \mathbb{R}^{1 \times 2|I|}$  the row vector of column-wise means of  $X$ , containing the average deformation over time:

$$\mu_X = [\mu_x(\vec{x}_1), \mu_y(\vec{x}_1), \mu_x(\vec{x}_2), \dots, \mu_y(\vec{x}_{|I|})] \quad (16)$$

In this equality,  $\mu_x(\vec{x}_i)$  and  $\mu_y(\vec{x}_i)$  respectively refer to the averages of  $u_x(\vec{x}_i, t_k)$  and  $u_y(\vec{x}_i, t_k)$  over time steps  $k \in \{1, \dots, M\}$ . We define the centered data matrix  $X_c$ , whose columns each have zero mean, as:

$$X_c = X - \mathbb{1}_{M \times 1} \mu_X \quad (17)$$

Given an arbitrary integer  $n_{cp}$ , PCA seeks two matrices,  $W \in \mathbb{R}^{M \times n_{cp}}$  and  $U \in \mathbb{R}^{2|I| \times n_{cp}}$ , that minimize the quantity  $\|X_c - WU^T\|_F$ , where  $\|\cdot\|_F$  designates the Frobenius norm, subject to the following two conditions:

offset without accounting for the horizon; this likely has a minor effect on performance as we set the maximum random linear slope to 0.05 (Table 10). Horizon-aligned augmentation is left for future work as an improvement.

- $W^T W$  is a diagonal matrix
- $U^T U = I_{n_{cp}}$  (identity matrix of size  $n_{cp}$ )

Specifically, we first perform the spectral decomposition of  $Y = X_c X_c^T$ , i.e., we compute the matrix of eigenvectors  $V$  and diagonal matrix  $\Lambda$  that contains the square roots of the eigenvalues, satisfying by definition:

$$Y = V \Lambda^2 V^T \quad (18)$$

We introduce the following notations:

$$\Lambda = \begin{bmatrix} \lambda_1 & & \\ & \ddots & \\ & & \lambda_M \end{bmatrix} \quad \text{with } \lambda_1 \geq \dots \geq \lambda_M \geq 0 \quad (19)$$

$$V = [V_1, \dots, V_M] \quad (20)$$

We multiply each column  $V_i$  by the sign of its first non-zero entry (which thereby becomes positive). We included that additional normalization step to make the PCA output consistent regardless of the eigendecomposition algorithm.  $W$  and  $U$  are computed using the first  $n_{cp}$  eigenpairs, as follows:

$$W = [V_1, \dots, V_{n_{cp}}] \begin{bmatrix} \lambda_1 & & \\ & \ddots & \\ & & \lambda_{n_{cp}} \end{bmatrix} \quad (21)$$

$$U = X_c^T [V_1, \dots, V_{n_{cp}}] \begin{bmatrix} 1/\lambda_1 & & \\ & \ddots & \\ & & 1/\lambda_{n_{cp}} \end{bmatrix} \quad (22)$$

$X$ ,  $W$ , and  $U$  approximately satisfy the following relationship:

$$X - \mathbb{1}_{M \times 1} \mu_X = WU^T \quad (23)$$

The rows of  $W$  contain the time-dependent PCA coefficients (weights), while the columns of  $U$  represent spatial

RNN parameters	
Training loss	Instantaneous squared error
Number and size of hidden layers	Number: 1, size <sup>†</sup> : $d$
Activation function $\Phi$	Hyperbolic tangent
Optimization method	SGD (learning rate <sup>†</sup> : $\eta$ )
Gradient clipping threshold	100.0
Learnable parameter initialization	Gaussian $\mathcal{N}(0, \sigma = 0.02)$
Transformer parameters	
Training loss	MSE loss
Embedding dimension <sup>†</sup>	$d_{model}$
Number of encoder layers <sup>†</sup>	$n_{layer}$
Number of heads	2
Dimension of the FFN in each encoder layer	$2d_{model}$ (sequence-specific) or 16 (population model)
Output-head FFN hidden width	$\lfloor \sqrt{Ld_{model}n_{cp}} \rfloor$
Activation function	ReLU
Optimization method	ADAM (learning rate <sup>†</sup> : $\eta$ )
Dropout probability	0.5
Batch size	32
Number of epochs	50 (sequence-specific model) max. 300 (population model)
Early stopping patience	30 (population model only)
Learnable parameter initialization	Fan-in/fan-out-aware (Kaiming/Xavier-style)
Resampling method for cross-dataset training	Bandlimited FIR interpolation (via polyphase filtering)
Data augmentation (pop. only):	
- probability to scale amplitude	0.8
- amplitude scaling range	[0.8, 1.2]
- prob. to permute components	0.5
- probability to add bias or drift <sup>12</sup>	0.3
- maximum additive slope allowed	$0.05 \times$ amplitude
- maximum additive offset allowed	$0.2 \times$ amplitude

**Table 10**

Parameters related to the configuration of RNNs and transformers. Early stopping is only implemented for population transformers; the "patience" parameter refers to the number of epochs to wait for a loss decrease before terminating training. Quantities marked with <sup>†</sup>, and  $L$  (the SHL), were tuned via grid search on the validation set (cf. Table 2 for the allowed parameter ranges).

deformation modes. Accordingly, we denote the entries of  $W$  and  $U$  as follows:

$$W = \begin{bmatrix} w_1(t_1) & \dots & w_{n_{cp}}(t_1) \\ \dots & \dots & \dots \\ w_1(t_M) & \dots & w_{n_{cp}}(t_M) \end{bmatrix} \quad (24)$$

$$U = \begin{bmatrix} u_1^x(\vec{x}_1) & \dots & u_{n_{cp}}^x(\vec{x}_1) \\ u_1^y(\vec{x}_1) & \dots & u_{n_{cp}}^y(\vec{x}_1) \\ u_1^x(\vec{x}_2) & \dots & u_{n_{cp}}^x(\vec{x}_2) \\ \dots & \dots & \dots \\ u_1^y(\vec{x}_{|I|}) & \dots & u_{n_{cp}}^y(\vec{x}_{|I|}) \end{bmatrix} \quad (25)$$

Using those notations<sup>13</sup>, Eq. 23 can be rewritten as Eq. 2, which holds for the time steps used to build  $X$ , and is extended to  $k > M_{train}$  via projection (as discussed below). Noticeably, with our eigenvector sign convention (positive

General validation settings	
Metric for selecting parameters	nRMSE (Eq. 9), except for $n_{cp}$
Metric for selecting $n_{cp}$	$E_{pred}(n_{cp})$ (Eq. 13)
Validation range for $n_{cp}$	$n_{cp} \in \{1, 2, 3, 4\}$
Network stochasticity mitigation	
Number of runs for selecting the algorithm hyperparameters	$n_{cv} = 250$ (10 for RTRL and sequence-specific transformer, 5 for population transformer)
Nb. of runs to evaluate PCA score prediction accuracy of the test set	$n_{test}^{PCA}$ , set to the same value as $n_{cv}$ (Section 3.2.1)
Number of runs to evaluate image prediction accuracy of the test set and transformers	$n_{test} = 25$ (5 for RTRL and transformers)
Number of runs for selecting $n_{cp}$	$n_{cv}^{dim}$ , set to the same value as $n_{test}$ (Section 2.5)
Sequence temporal split	
Number of images for optimizing DIR parameters (first 28.3 s)	$M_{DIR} = 90$ (ETH Zürich) $M_{DIR} = 170$ (OvGU)
Last training time step index for online methods ( $t_{M_{train}} = 28.3s$ )	$M_{train} = 90$ (ETH Zürich) $M_{train} = 170$ (OvGU)
Last training time step index for offline methods ( $t_{M_{train}} = 50.4s$ )	$M_{train} = 160$ (ETH Zürich) $M_{train} = 303$ (OvGU)
Last validation time step index ( $t_{M_{cv}} = 56.6s$ )	$M_{cv} = 180$ (ETH Zürich) $M_{cv} = 340$ (OvGU)
Proportion of each sequence for training the population transformer	first 80% of the sequence (validation: last 20%)
Test time interval (all models):	
- ETH Zürich (20 time steps)	last 6.3s of each sequence
- OvGU (158 time steps)	last 26.3s of each sequence

**Table 11**

Parameters related to the general experimental setup.

first-row entry), we have  $w_j(t_1) \geq 0$  for all  $j \in \{1, \dots, n_{cp}\}$  (Figs. 7 and 9).

Moreover, the relationship  $U^T U = I_{n_{cp}}$ , which expresses the orthonormality of the principal components, is equivalent to Eq. 4. Using the same relationship, one can rewrite Eq. 23 as follows:

$$W = X_c U \quad (26)$$

For  $k \in \mathbb{N}$ , we denote by  $X_c(t_k)$  the row vector obtained by flattening the DVF at time  $t_k$  and centering it with  $\mu_X$ , the mean DVF over the training-set time steps (Eq. 16):

$$X_c(t_k) = [u_x(\vec{x}_1, t_k), u_y(\vec{x}_1, t_k), u_x(\vec{x}_2, t_k), \dots, u_y(\vec{x}_{|I|}, t_k)] - \mu_X \quad (27)$$

For  $k \leq M_{train}$ ,  $X_c(t_k)$  is the  $k^{\text{th}}$  row of  $X_c$ , and Eq. 26 is equivalent to:

$$[w_1(t_k), \dots, w_{n_{cp}}(t_k)] = X_c(t_k) U \quad (28)$$

This equation expresses the weights at time  $t_k$  as the projection of  $X_c(t_k)$  onto the  $n_{cp}$ -dimensional linear subspace of  $\mathbb{R}^{2|I|}$  spanned by the orthonormal columns of  $U$ . We assume that spatiotemporal dynamics remain approximately stable throughout the MRI sequence, and define the weights at time  $t_k$  as the projection of  $X_c(t_k)$ , computed using the incoming

<sup>13</sup>We define  $\vec{\mu}(\vec{x}_i) = [\mu_x(\vec{x}_i), \mu_y(\vec{x}_i)]^T$  and  $\vec{u}_j(\vec{x}_i) = [u_j^x(\vec{x}_i), u_j^y(\vec{x}_i)]^T$ .

image, onto the same hyperplane, during inference. In other words, Eq. 28 defines the weights for  $k > M_{train}$ , by projection onto the fixed basis  $U$ . Fig. 2 illustrates this projection idea. Eq. 3 follows directly from Eq. 28.

## D. Appendix: Experimental setup

Tables 10 and 11 summarize the parameters related to the RNN and transformer configuration and overall experimental setup, respectively. We clipped the loss gradient norm to 100.0 for RNNs and 2.0 for LMS, respectively [85]. The forecasting pipeline and performance evaluation were implemented in MATLAB for consistent evaluation across methods. Transformer training and inference were implemented in Python, interfaced with the MATLAB code, and conducted on consumer-grade GPUs (NVIDIA GeForce RTX 3060 and RTX 4060).

## E. Appendix: Further results on performance variation with the horizon

Fig. 19 shows the performance of each algorithm as a function of the horizon  $h$  on the OvGU dataset (full-frame evaluation). Stability with respect to  $h$  is detailed in Table 12.

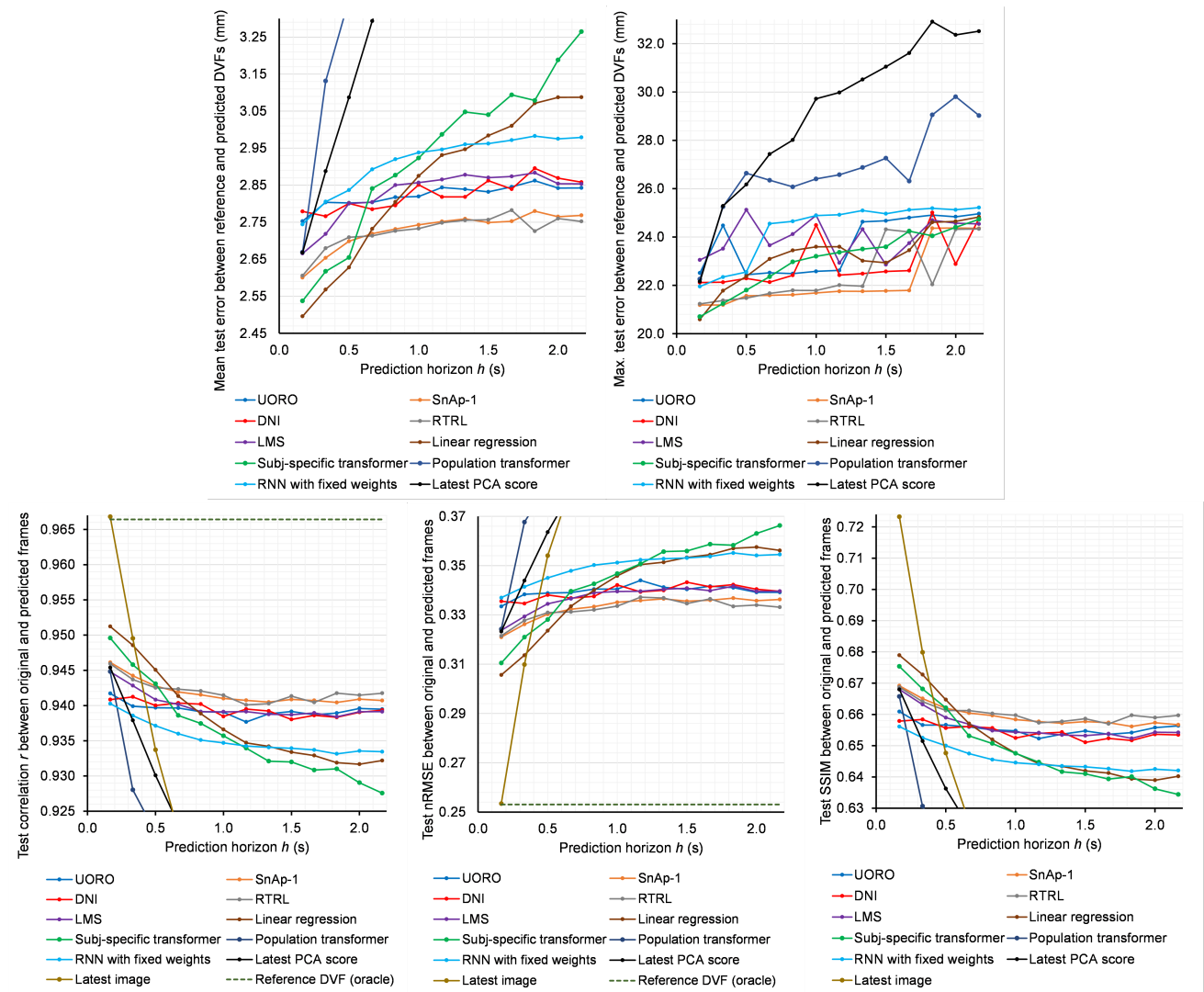


**Figure 19:** Test-set frame-forecasting performance for each algorithm as a function of the horizon, for the OvGU dataset (evaluation on the entire images). Each point represents the average of a given metric over the eight image sequences and  $n_{\text{test}}$  runs. Hyperparameters, including  $n_{cp}$ , were optimized for each horizon (and for each sequence, except the population transformer). The mean of each curve (i.e., the performance averaged over  $h$  for each method) is reported in the “OvGU (whole image)” columns of Table 4. The SSIM of the oracle baseline is not shown, for readability, as it exceeded that of the other methods by far.

		ETH Zürich		OvGU (whole image)		OvGU (ROI)	
		Test SSIM decrease (%)	Mean test DVF error increase (%)	Test SSIM decrease (%)	Mean test DVF error increase (%)	Test SSIM decrease (%)	Mean test DVF error increase (%)
<b>Prediction algorithms</b>	UORO	<b>0.2</b>	<b>3.4</b>	<b>0.03</b>	<b>1.4</b>	<b>0.1</b>	<b>2.2</b>
	SnAp-1	0.6	7.0	1.3	4.3	4.1	8.6
	DNI	<b>0.4</b>	<b>5.5</b>	0.8	3.3	<b>2.5</b>	6.1
	RTRL	0.6	6.8	<b>0.7</b>	<b>2.7</b>	<b>2.5</b>	<b>5.0</b>
	LMS	0.9	7.0	1.4	5.0	4.6	11.0
	Linear regression	1.3	19.4	4.8	20.2	14.7	42.9
	Sequence-specific transformer	1.6	17.3	5.1	24.7	14.9	48.4
	Population transformer	1.3	9.6	3.1	14.7	10.2	25.2
<b>Baselines</b>	RNN with a frozen hidden layer	0.8	7.5	1.6	6.2	5.7	12.4
	Latest PCA weight as prediction	2.1	5.5	9.7	41.6	30.4	79.8
	Latest image as prediction	3.7	n/a	15.6	n/a	40.4	n/a
Average over non-baseline RNN algorithms		0.4	5.3	0.7	3.0	2.2	5.6
Average over all non-baseline algorithms		0.9	9.5	2.1	9.5	6.7	18.7

**Table 12:** Test-set prediction performance stability with respect to the horizon  $h$  for each method, expressed as the relative decrease of the SSIM and relative increase of the mean DVF error (both in %) averaged over each dataset (and evaluation region—ROI or whole image—for the OvGU data) between  $h = 0.3\text{s}$  and  $h = 2.2\text{s}$ . These relative differences are computed from the data points in Figs. 13, 14, and 19. In each column, the values corresponding to the two most stable non-baseline algorithms are bolded (ties included).